

# Fundamentals and Applications of Slow Light

by

Zhimin Shi

Submitted in Partial Fulfillment of  
the Requirements for the Degree  
Doctor of Philosophy

Supervised by  
Professor Robert W. Boyd

The Institute of Optics  
Arts, Sciences and Engineering  
Edmund A. Hajim School of Engineering and Applied Sciences

University of Rochester  
Rochester, New York

2010

*To Yuqi (Miles) and Xiang*

## Curriculum Vitae

Zhimin Shi was born in Hangzhou, Zhejiang, China in 1979. He completed his early education in Hangzhou Foreign Language School in 1997. Following that, He studied in Chu Ke Chen Honors College as well as the Department of Optical Engineering at Zhejiang University and received B.E. with highest honors in Information Engineering in 2001. He joined the Center for Optical and Electromagnetic Research at Zhejiang University under the supervision of Dr. Sailing He and Dr. Jian-Jun He in 1999, where he focused his study on integrated diffractive devices for wavelength division multiplexing applications and the performance analysis of blue-ray optical disks. After receiving his M.E. with honors in Optical Engineering from the same university in 2004, he joined the Institute of Optics, University of Rochester and has been studying under the supervision of Prof. Robert W. Boyd. His current research interests include nonlinear optics, nano-photonics, spectroscopic interferometry, fiber optics, plasmonics, electromagnetics in nano-composites and meta-materials, etc.

### Publications related to the thesis

1. “Enhancing the spectral sensitivity of interferometers using slow-light media,” Z. Shi, R. W. Boyd, D. J. Gauthier and C. C. Dudley, *Opt. Lett.* **32**, 915–917 (2007).
2. “Design of a tunable time-delay element using multiple gain lines for increased fractional delay with high data fidelity,” Z. Shi, R. Pant, Z. Zhu, M. D. Stenner, M. A. Neifeld, D. J. Gauthier, and R. W. Boyd, *Opt. Lett.* **32**, 1986–1988 (2007).
3. “Maximizing the opening of eye diagrams for slow-light systems,” R. Pant, M. D. Stenner, M. A. Neifeld, Z. Shi, R. W. Boyd, D. J. Gauthier, *Appl. Opt.*, **46**, 6513–6519 (2007).
4. “A Slow-Light Fourier Transform Interferometer,” Z. Shi, R. W. Boyd, R. M. Camacho, P. K. Vudyasetu, and J. C. Howell, *Phys. Rev. Lett.* **99**, 240801 (2007).
5. “Slow-Light Interferometry: Practical Limitations to Spectroscopic Performance,” Z. Shi, and R. W. Boyd, *J. Opt. Soc. Am. B* **25**, C136–C143 (2008).
6. “Discretely tunable optical packet delays using channelized slow light,” Z. Shi, and R. W. Boyd, *Phys. Rev. A* **79**, 013805 (2009).
7. “Electromagnetic momenta and forces in dispersive dielectric media,” D. H. Bradshaw, Z. Shi, R. W. Boyd, and P. W. Milonni, *Opt. Commun.*, **283**, 650–656 (2009).
8. “Demonstration of a low-distortion bidirectionally tunable optical timing module using stimulated Brillouin scattering,” Z. Shi, A. Schweinsberg, J. E. Vornehm, Jr., M. A. Martínez Gámez, and R. W. Boyd, *Phys. Lett. A*, **374**, 4071–4074 (2010).
9. “Noise Properties of Propagation through Slow- and Fast-Light Media,” R. W. Boyd, Z. Shi, and P. W. Milonni, *J. Opt.*, **12**, 104007 (2010).
10. “A general quantum model for non-ideal amplifiers and attenuators,” Z. Shi, P. W. Milonni, and R. W. Boyd, (in preparation).

### Other publications

1. “Surface-plasmon polaritons on metal-dielectric nanocomposite films,” Z. Shi, G. Piredda, A. C. Liapis, M. A. Nelson, L. Novotny, and R. W. Boyd, *Opt. Lett.*, **34**, 3535–3537 (2009).

### Conference papers related to the thesis

1. "Slow Light with Gain Induced by Three Photon Effect in Strongly Driven Two-Level Atoms," Y. Chen, Z. Shi, P. Zerom, and R. W. Boyd, *OSA Slow and Fast Light (SL)*, ME1 (2006).
2. "Distortion-Reduced Pulse-Train Propagation with Large Delay in a Triple Gain Media," Z. Shi, R. W. Boyd, Z. Zhu, D. J. Gauthier, R. Pant, M. D. Stenner and M. A. Neifeld, *OSA Slow and Fast Light (SL)*, WB3 (2006).
3. "Spectroscopic Interferometry Using Slow Light Media," Z. Shi, R. W. Boyd and D. J. Gauthier, *FiO/LS* (2006).
4. "Distortion-Reduced Pulse-Train Propagation with Large Delay in a Triple Gain Media," Z. Shi, R. W. Boyd, Z. Zhu, D. J. Gauthier, R. Pant, M. D. Stenner and M. A. Neifeld, *OSA Slow and Fast Light (SL)*, WB3 (2006).
5. "Enhancing the Spectral Sensitivity and Resolution of Interferometers Using Slow-Light Media," Z. Shi, R. W. Boyd, D. J. Gauthier, and C. C. Dudley, *CLEO/QLES CTuT2* (2007).
6. "Enhancing the Performance of Spectroscopic Interferometers Using Slow-Light Media," Z. Shi, and R. W. Boyd, *CQO-9/ICQI 2007 CSuA44* (2007).
7. "A Slow-Light Fourier-Transform Interferometer," Z. Shi, and R. W. Boyd, *FiO/LS FThG2* (2007).
8. "Design of a tunable time-delay element with high data fidelity using dispersion management," Z. Shi, and R. W. Boyd, *CLEO/QLES CWQ5* (2008).
9. "Pulse-Distortion Management Using the Pulse-on-Background Method and Multiple Closely Spaced Gain Lines in Slow/Fast Light Propagation," H. Shin, Z. Shi, A. Schweinsberg, G. Gehring, and R. W. Boyd, *OSA Slow and Fast Light (SL)*, STuA3 (2008).
10. "Enhancement of the Spectral Performance of Interferometers Using Slow Light Under Practical Conditions," Z. Shi, and R. W. Boyd, *OSA Slow and Fast Light (SL)*, SWA3 (2008).
11. "Optical Packet Delay Using Channelized Slow Light," Z. Shi, and R. W. Boyd, *FiO/LS FThW2* (2008).

12. “A bidirectionally tunable optical timing module using stimulated Brillouin scattering,” Z. Shi, A. Schweinsberg, J. E. Vornehm, Jr., M. A. Martínez Gámez, and R. W. Boyd,, *CLEO/QELS*, CTuI1 (2010).

### Other conference papers

1. “Single Photon Source on Demand Based on Single-Colloidal-Quantum-Dot Fluorescence in Chiral Photonic Bandgap Liquid Crystal Hosts,” L. J. Bissell, Z. Shi, H. Shin, S. G. Lukishova, S. White, R. W. Boyd, and C. R. Stroud, Jr., *CLEO/QELS*, JMC4 (2007).
2. “Surface Plasmon Polaritons on Metal-Dielectric Nanocomposite Films,” Z. Shi, G. Piredda, A. C. Liapis, M. A. Nelson, L. Novotny, and R. W. Boyd, *CLEO/QELS*, IThG16 (2009).
3. “Optical Modes on Anisotropic Epsilon-Near-Zero Films,” Z. Shi, A. C. Liapis, and R. W. Boyd, *FiO/LS* FMA2 (2009).

## Acknowledgments

The pursuit of a Ph.D. is a journey of adventure, a journey filled with challenges and difficulties. Luckily, I have never been alone but with many guiding lights and companions, which made my journey filled with memorable moments full of joy and pleasure.

First, I would like to express my most sincere gratitude to Prof. Robert W. Boyd, my thesis advisor, for his constant guidance, inspiration, support and care over the past six years. My journey would not have been possible if not for Prof. Boyd's keen insights, never-ending encouragement and the persistence to interpreting physical concepts using most intuitive pictures. Furthermore, he has been constantly revealing new territories of research to me, which not only broadens my sights of views, but more importantly, teaches me how to search for treasure islands through the vast and challenging ocean of scientific research.

Secondly, I would like to thank Prof. Daniel J. Gauthier at Duke University, Prof. John C. Howell, and Prof. Lukas Novotny, both at the University of Rochester, for their mentoring during the fruitful collaborations. I have learnt a lot of hands-on knowledge from them, and I enjoy very much the scientific conversations with them. I am grateful to Prof. Peter W. Milonni for many collaborative discussions regarding many fundamental problems. His thought-provoking comments and suggestions have always enlightened me and inspired me towards new directions. I want to express my gratitude to Prof. Antonio Badolato for the helping discussion and guidance over the past years. His expertise and experience in photonic crystal and nano-fabrication have vastly enhanced my understanding of the field and have helped me greatly traveling in the realm of nano-photonics. I thank Brian McIntyre for his great course on SEM/TEM and constant support and help in the characterization and fabrication of various nano-photonic materials and devices. I would like to sincerely thank Prof. Govind Agrawal, Prof. Philippe Fauchet and Prof. Antonio Badolato for accepting to serve on my thesis committee, and I appreciate all the suggestions and

comments that they made on my research efforts and the thesis. Furthermore, I am always indebted to all the staff at the Institute of Optics, especially Per Adamson, Maria Schnitzler, Noelene Votens, Joan Christian, Lissa Cotter and Marie Banach, for their endless help and loving care through out my years at the Institute.

I am very thankful that I have had wonderful collaborations with Dr. C. C. Dudley, Dr. Zhaoming Zhu, Dr. Ravi Pant, Dr. Michael D. Stenner, Petros Zerom, Heeduek Shin, Luke Bissell, Dr. Svetlana Lukishova, Dr. Mark A. Neifeld, Dr. Ryan M. Camacho, Praveen K. Vudyasetu, Dr. Giovanni Piredda, Andreas C. Liapis, Dr. Mark A. Nelson, Dr. Douglas H. Bradshaw, Aaron Schweinsberg, Joseph E. Vornehm, Jr., and Dr. M. Alejandrina Martínez Gámez. I also appreciate the generous help from and wonderful discussions with Dr. Alan E. Willner, Dr. Miguel Alonso, Dr. Gary W. Wicks, Dr. Renee Pedrazzani, Brad Deutsch, Sean Anderson, Yi-Ho (Jonathan) Lee, Yijing Fu, Michael Theisen, Dr. Anand K. Jha, Colin O'Sullivan, Dr. Ksenia Dolgaleva, George Gehring, Dr. Kam Wai Clifford Chan, Bosheng Gao, Brandon Rodenburg, Dr. Jonathan Leech, Dr. Rob Ilic, Dr. Liu Liu, Dr. Long Chen, Dr. Zhichao Ruan, and all others.

I want to express my deepest gratitude to my wife, Xiang, my newly arrived son, Miles, and the rest of my family, who have always be there throughout the lows and the highs with unconditional love and supports.

Last but not the least, I give thanks to all my friends in Rochester and around the world, who have provided me with much enjoyment through their company, best wishes and helping hands whenever needed.

## Abstract

“Slow and fast light” constitute a broad class of science and technology that can dramatically change the group index of a medium over a certain wavelength range. This thesis is composed of studies regarding both fundamental aspects and applications of slow light.

The thesis starts with some discussion on two fundamental questions. The first one is how much momentum a photon carries within a slow-light medium, and what kind of force is experienced by a slow-light medium when a photon enters or leaves it. The second issue is how the noise properties of an optical field change as it propagates through a slow-light medium.

The second part of the thesis deals with the applications of slow light for tunable time delays. For such applications, one of the key figures of merit is the maximum fractional delay that a slow-light element can achieve. I first present a method with experimental demonstrations for improving the maximum fractional delay using a multiple-gain-line medium. Second, I present a design with experimental demonstration for how to achieve simultaneous tunable delay and advancement using slow and fast light in a single module. I then propose a design of a digitally tunable module using channelized slow light, which can be useful for optical packet delays, etc.

The third part of the thesis studies the use of slow light to enhance the performance of spectroscopic interferometers. I start with the derivation of the spectral sensitivity of two-beam and multiple-beam interferometers with slow-light media incorporated in them. I show both theoretically and experimentally that the spectral sensitivity is proportional to the group index of the medium inside the interferometers. Second, I propose and demonstrate experimentally a new type of Fourier-transform interferometer using tunable slow light. I then analyze the performance of three types of slow-light media for interferometry applications. Lastly, I present a design of an

on-chip slow-light spectrometer as well as some studies on slow-light waveguides using photonic crystal structures.

# Contents

<b>Acknowledgments</b>	<b>viii</b>
<b>Abstract</b>	<b>ix</b>
<b>List of Figures</b>	<b>xxii</b>
<b>Foreword</b>	<b>1</b>
<b>1 Introduction</b>	<b>4</b>
1.1 Phase velocity and group velocity of light . . . . .	4
1.2 Microscopic and macroscopic slow light . . . . .	7
1.3 Applications of slow light and practical considerations . . . . .	10
1.4 Remainder of the thesis . . . . .	13
<b>2 Photon Momentum in Dispersive Dielectric Media</b>	<b>16</b>
2.1 Background . . . . .	16
2.2 Photon momentum in non-dispersive media . . . . .	17
2.3 Photon momentum in dispersive media . . . . .	19
2.4 Momenta and force on polarizable particles . . . . .	23
2.5 Change of momenta between light and particles . . . . .	28
2.6 Force on a dielectric sphere . . . . .	30
2.7 Conclusions . . . . .	32
2.8 Appendix: energy density in dispersive media . . . . .	33

<b>3</b>	<b>Noise Properties of Slow-Light Media</b>	<b>35</b>
3.1	Background . . . . .	35
3.2	A quantum model of an ideal linear amplifier . . . . .	36
3.3	A quantum model of an ideal linear attenuator . . . . .	38
3.4	A generalized model for a non-ideal linear amplifier or attenuator . .	40
3.4.1	A not-entirely-inverted laser amplifier . . . . .	42
3.4.2	A stimulated Brillouin scattering amplifier . . . . .	47
3.5	Noise figure of a gain-induced slow-light medium . . . . .	48
3.6	Summary . . . . .	51
<b>4</b>	<b>Increasing the Fractional Delay of a Slow-Light Delay Element Using Multiple Gain Lines</b>	<b>52</b>
4.1	Fractional delay and practical considerations . . . . .	52
4.2	Optimization design using multiple gain lines . . . . .	55
4.3	Experimental demonstration . . . . .	57
4.4	Summary . . . . .	62
<b>5</b>	<b>Continuously Tunable, Positive and Negative Time Delays with Optimized Stimulated Brillouin Scattering Slow and Fast Light</b>	<b>64</b>
5.1	Background . . . . .	64
5.2	Theory of slow and fast light using gain media . . . . .	65
5.3	Experimental demonstration using stimulated Brillouin scattering . .	67
5.4	Summary . . . . .	73
<b>6</b>	<b>Channelized Slow Light For Discretely Tunable Optical Packet Delays</b>	<b>74</b>
6.1	A fundamental limit on maximum achievable fractional delay of a slow-light element . . . . .	74
6.2	Principle of channelized slow light . . . . .	76
6.3	A numerical example using stimulated Brillouin scattering slow light .	83

6.4	Summary . . . . .	88
<b>7</b>	<b>Slow Light Interferometry</b>	<b>89</b>
7.1	Background . . . . .	89
7.2	Two-beam interferometers . . . . .	90
7.3	Multiple-beam interferometers . . . . .	91
7.4	Experimental demonstration . . . . .	95
7.5	Practical considerations . . . . .	97
7.6	Summary . . . . .	101
<b>8</b>	<b>Slow Light Fourier-Transform Interferometry</b>	<b>103</b>
8.1	Conventional Fourier transform interferometry . . . . .	103
8.2	A slow-light Fourier transform interferometer . . . . .	105
8.3	Experimental demonstration . . . . .	108
8.4	Practical considerations . . . . .	112
8.5	Summary . . . . .	115
<b>9</b>	<b>Evaluating Slow Light Processes for Interferometry Applications</b>	<b>116</b>
9.1	Introduction . . . . .	116
9.2	Single isolated Lorentzian gain line . . . . .	117
9.3	Separated double absorption lines . . . . .	119
9.4	Electromagnetically induced transparency . . . . .	122
9.5	Summary . . . . .	125
<b>10</b>	<b>On-Chip Slow-Light Interferometers</b>	<b>127</b>
10.1	Design of the geometry of an on-chip spectrometer . . . . .	127
10.2	Photonic crystal waveguide . . . . .	132
10.3	Design of a flat-band slow-light photonic crystal waveguide . . . . .	134
10.4	Coupling between a normal waveguide and a slow-light waveguide . . . . .	138
10.5	Overview of fabrication procedures . . . . .	141

<i>CONTENTS</i>	xiv
10.6 Summary . . . . .	143
<b>Bibliography</b>	<b>145</b>

# List of Figures

1.1	Gain coefficient $g$ , real part of refractive index $n$ and group index $n_g$ as functions of frequency detuning near a gain resonance with intensity gain of $G = e \text{ m}^{-1}$ and linewidth of $\gamma = 1 \text{ MHz}$ . . . . .	8
3.1	One can describe a realistic amplifier using (a) a series of alternating ideal amplifiers and attenuators, or (b) a general quantum beam splitter model. . . . .	41
3.2	The average photon number and its variance for the output field of a not-entirely-inverted amplifier using two different models. $M$ is the number of divided ideal sub-amplifier/attenuator pairs. The average photon number of the input field is $\langle \hat{n}_a \rangle = 1$ , the total gain of the amplifier is $G = 10$ , and the spontaneous emission factor is $n_{\text{sp}} = 2$ . . . . .	43
3.3	Noise figure of a laser medium as a function of intensity gain $G$ and spontaneous emission factor $n_{\text{sp}}$ when it operates as (a) an amplifier and (b) an attenuator. Here, the average photon number of the input field is 1000. . . . .	46
3.4	The expectation value of photon number in the noise input source $\langle \hat{n}_c \rangle$ of a SBS medium as a function of temperature $T$ . . . . .	47
3.5	(a) The spontaneous emission factor $n_{\text{sp}}$ and (b) noise figure $\mathcal{F}$ of a laser medium as functions of the intensity gain for input fields with different values of average photon number. . . . .	49

3.6 The noise figure  $\mathcal{F}$  of an SBS medium as a function of the intensity gain for input fields with different values of average photon number. . . . . 50

4.1 Schematic diagram of a SBS-based tunable delay line. TL: tunable laser; FPC: fiber polarization controller; MZM: Mach-Zehnder modulator; AFG: arbitrary function generator; SCF: small-core fiber; EDFA: Erbium doped fiber amplifier; VOA: variable optical attenuator. The inset on the right shows a typical profile of  $\tilde{n}$  for a triple-gain-line medium. . . . . 57

4.2 Maximum fractional delay for triple and double gain media as bandwidth increases when single pulse metrics are considered. . . . . 58

4.3 (a) Maximum achievable fractional delay  $\overline{\Delta T}_{\max}$ ; (b) corresponding eye-opening penalty EOP; and (c) optimum values of the half separation  $\delta_{\text{opt}}$  and peak ratio  $r_{\text{opt}}$  as functions of normalized bandwidth for the SGL, DGL and TGL media, respectively, when system metrics are considered. . . . . 59

4.4 The eye diagram of (a) a theoretical noiseless input; (b) a theoretical noiseless output; (c) the actual input in the experiment; and (d) the actual output in the experiment for the optimum design of a TGL medium with  $\overline{\Delta T} \approx 1.9$  at  $\Delta\nu = 1.4\gamma$ . The dotted lines indicate the magnitude of the eye-opening  $\mathcal{E}$  of each cases. . . . . 60

4.5 (a) Simulated results of fractional delay  $\overline{\Delta T}$ ; and (b) eye-opening penalty EOP as functions of gain (normalized by the gain required to achieve  $\overline{\Delta T}_{\max}$ ) for optimum designs of a triple-gain-medium at various bandwidths. . . . . 61

5.1 Schematic diagram of a bidirectionally tunable optical timing element using stimulated Brillouin scattering. TL: tunable laser; IM: intensity modulator; AFG: arbitrary function generator; SMF: single-mode fiber; EDFA: erbium doped fiber amplifier; VOA: variable optical attenuator. . . . . 68

5.2 Schematics of creating multiple gain line profile using dual-stage modulation method. The orange and green arrows indicate the created discrete frequency side bands with each modulation stage. . . . . 68

5.3 Measured small signal gain and calculated induced refractive index change as functions of frequency detuning for slow light [(a) and (b)] and fast light [(c) and (d)] configurations. The black dotted lines in (a) and (c) show the power spectrum of Gaussian pulses with FWHM of 6.5 ns. . . . . 69

5.4 Calculated optimized and un-optimized gain profiles as functions of frequency detuning for slow light (a) and fast light (c) configurations, and the RMS width of the output pulse for different gain profiles as functions of peak delay for slow light (b) or advancement for fast light (d) configuration. . . . . 70

5.5 Measured fractional delay (circles) and advancement (triangles) as functions of the pump power. The error bars are the standard deviations. 71

5.6 Output pulse as a function of time for reference, slow-light, and fast-light configurations. . . . . 72

6.1 Refractive index as a function of the detuning from some center frequency  $\nu_0$  for an ideal slow-light medium and for a channelized slow-light medium. Here  $\delta n = n'_g \Delta_c / \nu_0$  is the maximum refractive index variation for both types of medium within the frequency interval  $\Delta_c$ . 78

6.2 False-color representation of the amplitude of the output signal propagating through an ideal channelized delay device as a function of time and of the value of  $n'_g$ . Here the input signal is a Gaussian pulse with a half width to the 1/e intensity value of  $T_0$ , and the channel spacing  $\Delta_c$  is set equal to  $1/(8T_0)$ . The time axis is set so that  $t = 0$  indicates no delay as in the case in which  $n'_g = 0$ . . . . . 80

6.3 Schematic diagrams of (a) a  $1 \times 8$  spectral slicer using cascaded half-band filters; and (b) a channelized SBS slow-light delay element. . . . 82

6.4 (a) Transmission of each of the seven physical signal channels of a channelized SBS delay element; (b) corresponding pump field spectrum for one particular signal channel (channel #4); and the SBS-induced (c) gain and (d) refractive index variation as functions of the detuning for channel #4 (solid line) and for a broadened gain profile (dashed line), respectively. . . . . 84

6.5 Outputs of a 40 Gbps, RZ data train ‘1010’ after propagating through a channelized SBS delay element with  $\Delta_c$  of 10 GHz (solid line), a single channel narrow-band SBS delay element (dash-dotted line) and a single channel broadband SBS delay element (dashed line), respectively. The dotted line is the reference output. . . . . 85

6.6 Eye-openings of three channelized devices as functions of the standard deviation phase noise level  $\delta\phi$  among different spectral channels. The insets show typical eye-diagrams for (a) an ideal channelized slow-light device; (b) an channelized device with realistic spectral slicers and ideal slow-light media; and (c) an realistic channelized SBS slow-light device, respectively. The corresponding eye-openings are given on top of each eye-diagram, respectively. . . . . 86

7.1 Schematic diagram of a Mach-Zehnder interferometer containing a slow-light medium in one arm. . . . . 90

7.2	Left: Schematic diagram of a slow-light Fabry-Perot interferometer. Right: A close look at the multiple beam interference within the F-P etalon. . . . .	92
7.3	Schematic diagram of a wedged shear interferometer containing a slow-light medium. . . . .	93
7.4	Relative rate of fringe movement as a function of wavelength. The squares are experimental data with standard deviation bars, the solid line is the theoretical prediction and the dashed line is the prediction if dispersion is neglected. . . . .	97
7.5	Finesse of a F-P interferometer as a function of single path transmission $T_L$ . Here the reflectivity at the air-etalon interface is assumed to be 0.99.	99
7.6	Resolution of a F-P interferometer as a function of the etalon thickness $L$ for the etalon being composed of different materials. . . . .	101
8.1	Schematic diagrams of (a) a conventional FT interferometer with one moving arm and one fixed arm; and (b) a FT interferometer with a tunable slow-light medium in one of the two fixed arms. . . . .	105
8.2	Experimental setup of the FT interferometer using a rubidium vapor cell as the slow-light medium. . . . .	109
8.3	(a) Transmission; (b) refractive index $n$ ; and (c) group index $n_g$ of the 10-cm-long rubidium vapor cell at the temperature of approximately 100 °C as functions of detuning $\nu'$ . The thick curve is the measured transmission, and the thin curves are the fitted theory using Eq. (8.16). The inset shows the energy levels of the $^{87}\text{Rb}$ and $^{85}\text{Rb}$ D <sub>2</sub> transitions; and the gray region is the frequency region over which the spectral measurement are performed. . . . .	110
8.4	Output intensity of the slow-light FT interferometer as a function of the group delay $\tau_g$ for an input field of two sharp spectral lines separated by 80 MHz. . . . .	111

8.5 Retrieved spectrum of the input field using experimental data (solid line) and simulated data (dashed line) and the actual spectrum of the input field (dotted line). The resolution of a conventional FT interferometer of the same size would be approximately 100 times worse. . . . . 112

8.6 (a) Simulated output of a slow-light FTI as the reduced group index  $n'_g$  increases when the input field only contains a single frequency. (b) The retrieved spectrum as compared to a Lorentzian-shaped spectral line. . . . . 114

9.1 (a) The reduced group index  $n'_g$  and gain coefficient  $g$ , and (b) the characteristic spectral resolution  $\delta\nu_c$  as functions of the normalized frequency detuning from the resonance center for a single Lorentzian gain line medium. . . . . 119

9.2 (a) The reduced group index and absorption coefficient as functions of detuning for a double-absorption-line medium with  $\Delta = 4\gamma$ ; (b) the characteristic spectral resolution at  $\nu' = 0$ , and (c) the working finesse as functions of the normalized half separation between the two resonance centers. . . . . 121

9.3 Absorption coefficient, refractive index, and group index as functions of frequency detuning for a EIT medium with three different pump field strength. . . . . 122

9.4 (a) Energy level diagram of a  $\Lambda$ -type EIT system; (b) the reduced group index and absorption coefficient at the center frequency, (c) the characteristic spectral resolution at  $\nu' = 0$ , and (d) the working finesse, all plotted as functions of the normalized pump Rabi frequency for an EIT medium with  $\bar{\gamma} = 100$ . The dots are results using the approximate expression of Eqs. (9.22) and (9.25), and the solid lines are results based on the analytical expression of Eq. (9.17). . . . . 124

10.1 Schematic diagram of a slow-light arrayed waveguide grating spectrometer. . . . .	129
10.2 Linear transverse dispersion at the focal plane of the output FPR as a function of the group index of the waveguide of a slow-light AWG with $\Delta L = 10, 20$ and $40 \mu\text{m}$ , respectively. . . . .	132
10.3 Two-dimensional schematic diagram of a slab photonic crystal single line defect (W1) waveguide with lattice constant $a$ and hole radius $r$ . . . . .	133
10.4 (a) Dispersion relations of the fundamental guided Bloch modes of a PhC W1 waveguide; corresponding effective mode index (b) and reduced group index $n'_g$ (c) as functions of wavelength for such a waveguide structure. . . . .	134
10.5 Effective indices of a slab SOI waveguide for two different polarizations as functions of the thickness of the silicon core layer. . . . .	136
10.6 Two-dimensional schematics of a slab photonic crystal calzone line-defect waveguide with lattice constant $a$ and hole radius $r$ . . . . .	136
10.7 (a) dispersion relations of the fundamental guided Bloch modes of a flat-band calzone line-defect waveguide with $a = 403 \text{ nm}$ , $r = 0.3$ , and $w = 488.6 \text{ nm}$ ; corresponding effective mode index (b) and reduced group index $n'_g$ (c) as functions of wavelength for such a waveguide structure. . . . .	137
10.8 Two-dimensional schematics of connecting SOI channel waveguides with a photonic crystal calzone line-defect waveguide slab. Here $\Delta L$ is the difference between the actual start of the PhC slab and the start of the original unmodified slab. . . . .	139
10.9 TE Transmission through a channel-PhC-channel waveguide structure as a function of wavelength and the modification of the PhC slab length $\Delta L$ . . . . .	140

10.10	Average transmission over the slow-light regime through a channel-PhC-channel waveguide structure as a function of the modification of the PhC slab length $\Delta L$ . . . . .	141
10.11	Average transmission over the slow-light regime through a channel-PhC-channel waveguide structure as a function of the width of the channel waveguide $w_{\text{ch}}$ . . . . .	142
10.12	Schematic Flow Chart of fabricating a suspended silicon photonic crystal waveguide. . . . .	143

# Foreword

The contents of this thesis come from various research projects during my doctoral studies at University of Rochester, many of which are collaborative projects with my advisor, my fellow group members as well as other researchers at or outside of University of Rochester.

Chapter 2 is an extended version of a research paper entitled “Electromagnetic momenta and forces in dispersive dielectric media” published in *Opt. Commun.*, **283**, 650–656 (2009) written by D. H. Bradshaw, Z. Shi, R. W. Boyd, and P. W. Milonni. It was developed through a continuous exchange of ideas among all authors. Therefore, the extent of the contribution of each author cannot be disentangled.

Chapter 3 is the result of a joint work with Dr. R. W. Boyd and Dr. P. W. Milonni. The ideas are developed through a continuous discussions among all collaborators, and therefore the extent of the contribution of each author cannot be disentangled. Note that I am the second author of one research paper entitled “Noise Properties of Propagation through Slow- and Fast-Light Media” published in *J. Opt.*, **12**, 104007 (2010), and I am currently preparing the manuscript of a second paper.

Chapter 4 is primarily based on a collaboration with Dr. Z. Zhu and Dr. D. J. Gauthier at Duke University, and Dr. R. Pant, Dr. M. D. Stenner and Dr. M. A. Neifeld at University of Arizona. I performed the optimization design analysis, and carried out the experiment at Duke University together with my collaborators. Note that I am the first author of the research paper out of this collaboration entitled “Design of a tunable time-delay element using multiple gain lines for increased fractional

delay with high data fidelity,” published in *Opt. Lett.* **32**, 1986–1988 (2007).

Chapter 5 is an extended version of a research paper entitled “Demonstration of a low-distortion bidirectionally tunable optical timing module using stimulated Brillouin scattering” published in *Phys. Lett. A*, **374**, 4071–4074 (2010). The experimental work behind the paper was a team work with A. Schweinsberg, J. E. Vornehm, Jr., M. A. Martínez Gámez, and R. W. Boyd, and the manuscript was written through a continuous discussion and exchange of ideas among all authors. Therefore, the extent of the contribution of each author cannot be disentangled.

Chapter 6 is based on a research paper entitled “Discretely tunable optical packet delays using channelized slow light” published in *Phys. Rev. A* **79**, 013805 (2009). Please note that I am the first author of this work.

Chapter 7 is primarily based on a collaboration with Dr. D. J. Gauthier at Duke University and Dr. C. C. Dudley at Naval Research Laboratory. I performed the analysis of multiple-beam interferometers and carried out the experimental demonstration. Note that a research paper entitled “Enhancing the spectral sensitivity of interferometers using slow-light media” is published in *Opt. Lett.* **32**, 915–917 (2007), and I am the first author of this work.

Chapter 8 is mainly based on a collaboration with R. M. Camacho, P. K. Vudyaasetu, and Dr. J. C. Howell at University of Rochester. I conceived the original concept, but the details of the experiment was designed through a series discussions and meetings among all collaborators, and was carried out as a team work. Therefore, the extent of the contribution of each author cannot be disentangled.

Chapter 9 is an extended version of a research paper entitled “Slow-Light Interferometry: Practical Limitations to Spectroscopic Performance” published in *J. Opt. Soc. Am. B* **25**, C136–C143 (2008). Please note that I am the first author of this work.

Chapter 10 is based on an on-going collaboration with Andreas Liapis and Dr. A. Badolato’s group at University of Rochester. The design of the spectrometer geometry

as well as the slow light waveguides are being matured during continuous discussions among all collaborators, and the fabrication and the characterization are team work with all collaborators. Therefore the extent of the contribution of each author cannot be disentangled.

# Chapter 1

## Introduction

### 1.1 Phase velocity and group velocity of light

The pursuit of understanding the propagation of light can be traced back to the nineteenth century in the work of Fizeau, Lorentz, Michaelson, etc. One fundamental question that motivated generations of scientists is “how fast does the light travel?” Yet when one talks about the velocity of light, it could be ambiguous as to what one means. There are many different definitions of “the velocity of light” [1], including the phase velocity and the group velocity.

To understand the different definitions of velocity of light, let us first start from the mathematical description of the propagation of an electromagnetic field. Consider a monochromatic electromagnetic plane wave at angular frequency  $\omega$  propagating in the  $z$  direction, the complex electric field as a function of space and time is given by,

$$\mathcal{E}(z, t) = \mathcal{E}_0 e^{ikz - i\omega t}, \quad (1.1)$$

where  $\mathcal{E}_0$  is the amplitude of the field,  $k$  is the wave number,  $z$  is the position in space, and  $t$  is the time. The phase of such a field is defined as  $\phi(z, t) = kz - \omega t$ , and a phase front is defined by a plane on which the phase is constant, e.g.,  $\phi(z, t) = \phi_0$ . The

phase velocity of the plane wave is the propagation velocity of this constant phase front, which is given by

$$v_p = \frac{dz}{dt} = \frac{\omega}{k(\omega)} = \frac{\omega}{n(\omega)k_0} = \frac{c}{n(\omega)}, \quad (1.2)$$

where  $k_0$  is the wave number of the field at angular frequency  $\omega$  in vacuum, and  $n(\omega) \equiv k/k_0$  is the refractive index of the medium at angular frequency  $\omega$ .

While the phase velocity  $c/n$  shows the wave property of an electromagnetic field, it is not easy to measure experimentally because the phase oscillates much faster than a human eye can perceive. In fact, before the laser and vacuum technologies were available, all measurements for the speed of light involved somehow turning on and off a light source, and then measuring how long it took for the “light pulse” to propagate through a certain distance in air. Such measurements of the velocity of optical pulses is indeed the group velocity of light in air.

To see this point, we again start from the mathematical description of an optical pulse propagating in a medium. Consider an electromagnetic pulse propagating in the  $z$  direction, the complex electric field as a function of time at some starting point,  $z = 0$ , is given by

$$\mathcal{E}(z = 0, t) = A(t)e^{-i\omega_0 t}, \quad (1.3)$$

where  $A(t)$  and  $\omega_0$  are the slowly-varying envelope and the carrier (central) angular frequency of the pulse, respectively. One can also describe such a pulse in the frequency domain using Fourier analysis as follows:

$$\mathcal{E}(z = 0, t) = \frac{1}{2\pi} \int_{-\infty}^{\infty} E(\omega)e^{-i\omega t} d\omega, \quad (1.4)$$

where  $E(\omega)$  is the amplitude of spectral component at frequency  $\omega$  and is given by

the inverse Fourier transform relation,

$$E(z = 0, \omega) = \int_{-\infty}^{\infty} A(t) e^{i(\omega - \omega_0)t} dt. \quad (1.5)$$

Note that each plane wave component propagates at its own phase velocity as

$$E(z, t) = E_0 e^{ikz - i\omega t}, \quad (1.6)$$

where  $k = n(\omega)\omega/c$  is the wave number in the medium at angular frequency  $\omega$ .

Meanwhile, the pulse can be understood as the interference of a span of plane waves at different frequencies, and the peak is the point at which all the frequency components constructively interfere. The propagation of this peak indicates that the relative phase among all frequency components needs to be fixed, i.e.,

$$\Delta\phi = \phi(\omega_1) - \phi(\omega_2) = [k(\omega_1)z - \omega_1 t] - [k(\omega_2)z - \omega_2 t], \quad (1.7)$$

or

$$(k(\omega_1) - k(\omega_2))z = (\omega_1 - \omega_2)t + \Delta\phi, \quad (1.8)$$

for any two different frequencies  $\omega_1$  and  $\omega_2$ . Since the group velocity  $v_g$  describes the velocity of such a plane in the medium, at which the relative phase relations among different frequency components are maintained, one can derive  $v_g$  as follows:

$$\begin{aligned} v_g &= \frac{dz(\Delta\phi)}{dt(\Delta\phi)} = \frac{k(\omega_1) - k(\omega_2)}{\omega_1 - \omega_2} \\ &= \frac{dk}{d\omega} = \frac{d(n\omega)}{cd\omega} \\ &= \frac{n + \omega \frac{dn}{d\omega}}{c} = \frac{n_g}{c}. \end{aligned} \quad (1.9)$$

Here,  $n_g \equiv n + \omega dn/d\omega$  is the group index of the medium.

## 1.2 Microscopic and macroscopic slow light

The recent surge of interest in controlling the group velocity of light propagation, which started in the late 1990s, is partly indebted to the latest technologies that enable the achievement of exotic group indices. Remarkably slow group velocities of light, 17 m/s and 57 m/s have been experimentally observed in Bose-Einstein condensates [2] and in room-temperature Ruby crystals [3], respectively. Such a broad class of science and technologies, that can dramatically change the group index of a medium within certain wavelength range, is also known as “slow and fast light” [4, 1] or simply “slow light”.

Many mechanisms have been proposed and demonstrated to achieve slow light. Generally speaking, these mechanisms fall into one of two general categories, namely, “microscopic” and “macroscopic” slow light.

Microscopic slow light refers to those processes in which the change of group index is mainly due to light-matter interactions at the atom/molecule level. A slow-light medium typically indicates that  $n_g$  can be very different from  $n$ , i.e., the magnitude of  $\omega(dn/d\omega)$  term is an appreciable quantity. Meanwhile, the real and imaginary parts of the complex refractive index  $\tilde{n}$  satisfy the Kramers–Kronig (K–K) relations [5, 6]. Thus, large dispersion of  $\omega(dn/d\omega)$  usually occurs in the vicinity of some gain or absorption resonance features.

One example of a means to achieve slow light is to create a Lorentzian-shaped gain resonance. The real part of the refractive index and the gain coefficient as functions of the frequency detuning  $\nu' = \nu - \nu_0$  from the resonance center  $\nu_0$  are given by

$$n(\nu') = n(0) + \frac{g_0}{2k_0} \frac{\gamma\nu'}{\nu'^2 + \gamma^2}, \quad (1.10)$$

$$g(\nu') = g_0 \frac{\gamma^2}{\nu'^2 + \gamma^2}, \quad (1.11)$$

where  $g_0$  is the intensity gain coefficient, and  $\gamma$  is the  $1/e$  half width of the resonance.

The group index is then given by

$$n_g(\nu') = n + \nu_0 \frac{dn}{d\nu} = n(0) + \frac{g_0}{2k_0} \frac{\gamma \nu'}{\nu'^2 + \gamma^2} + \frac{cg_0\gamma}{4\pi} \frac{-\nu'^2 + \gamma^2}{(\nu'^2 + \gamma^2)^2}. \quad (1.12)$$

As one can see from Fig. 1.1, one has slow light ( $n_g > n$ ) in the center of the resonance and fast light ( $n_g < n$ ) in the wings of the resonance.

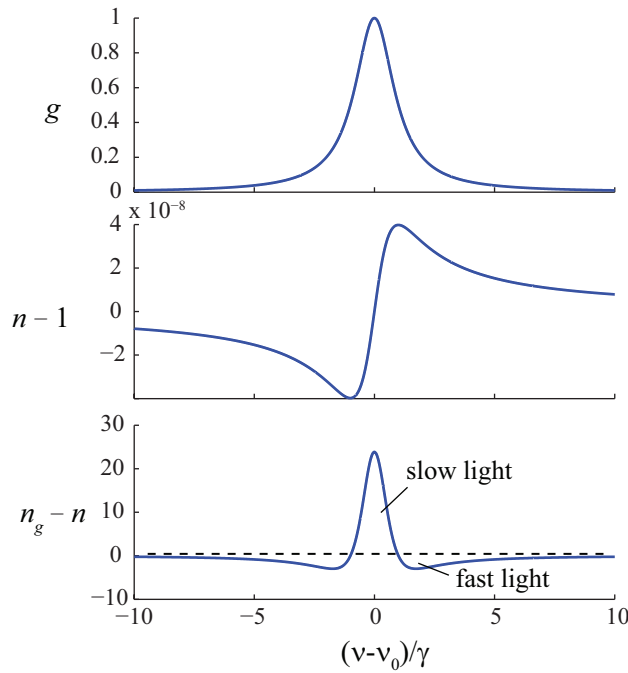


Figure 1.1: Gain coefficient  $g$ , real part of refractive index  $n$  and group index  $n_g$  as functions of frequency detuning near a gain resonance with intensity gain of  $G = e$   $\text{m}^{-1}$  and linewidth of  $\gamma = 1$  MHz.

Other examples of microscopic slow light include electromagnetically induced transparency (EIT) [2], coherent population oscillations (CPO) [7, 3, 8, 9], naturally occurring resonances [10] or band edges [11], stimulated Brillouin scattering (SBS) [12, 13], stimulated Raman scattering (SRS) [14], spectral hole burning [15], parametric amplification [16, 17], and so on.

Macroscopic slow light, on the other hand, indicates that the manipulation of the “effective group velocity” of light in the medium is achieved through the inter-

action between light and the structural geometry of an element that is comparable or larger than the optical wavelength. A macroscopic slow-light element is typically not spatially homogeneous but has a structural geometry with characteristic feature size comparable to or much larger than the wavelength. In such cases, the slow-light effect is best described by the group delay of propagation through the entire element, or at least one period of the structure if it is periodic, as follows,

$$\tau_g = \frac{d\phi(\omega)}{d\omega}, \quad (1.13)$$

where  $\phi(\omega)$  is the phase of the complex transfer function  $\tilde{H}(\omega) = A(\omega) \exp[i\phi(\omega)]$ . Sometimes it is convenient to define the effective refractive index  $n_{\text{eff}}$  and effective group index  $n_{g,\text{eff}}$  by assuming that the medium is homogeneous;

$$n_{\text{eff}}(\omega) = \frac{\phi(\omega)c}{\omega L}, \quad (1.14)$$

$$n_{g,\text{eff}} = n_{\text{eff}} + \omega \frac{dn_{\text{eff}}}{d\omega}, \quad (1.15)$$

where  $c$  is the speed of light in vacuum, and  $L$  is the length of the element or a period of the element.

Macroscopic slow light includes photonic bandgap structures [18, 19, 20, 21, 22, 23], single and coupled ring resonators [24, 25, 26], fiber or waveguide grating structures [27], and so on.

Note that the real and imaginary parts of  $\tilde{H}(\omega)$  have to satisfy the K–K relations due to the constraint of causality, but the amplitude response  $A(\omega)$  and the phase response  $\phi(\omega)$  are not necessarily connected through the K–K relation. Therefore, the design space of macroscopic slow light can be different from microscopic slow light, which may lead to different design approaches and consequently different performance.

## 1.3 Applications of slow light and practical considerations

Equipped with the ability to control the group index of a slow-light medium, one can control the time that a pulsed optical signal takes to propagate through the medium. Such all-optical controllable delay lines can lead to various applications. In fiber optics telecommunication systems, an all-optical tunable delay element can be used for all-optical buffering, data-resynchronization, jitter correction, etc. True optical delay elements are also useful for optical signal processing [28], slow-light laser radar (SLIDAR), RF photonics [29, 30], etc.

Besides the property of “slowing down” light pulses or optical wave packets, slow light has other properties that can lead to other applications. One of such properties is that the refractive index of a slow-light medium is highly frequency dependent [31]. In other words, a small shift in frequency  $\delta\omega$  will cause a large change in the wave number  $\delta k$  inside a slow-light medium. This is very important to the spectroscopic response of interferometric devices, and it is worthwhile to examine in detail how slow light can enhance the performance of spectroscopic interferometers, both in ideal and practical cases. Alternatively, fast light can be used to build interferometers that are insensitive to wavelength drift. Such a “white-light” interferometer [32] can be used for ultrahigh-precision metrology such as gravitational-wave detection.

As more and more fundamental aspects of slow light are being better understood, research on slow light is also leading to new areas of applications, such as to increase the nonlinear interaction between light and matter [33, 34], and so on.

In ideal cases, a pulse can maintain its temporal shape after propagating through a slow-light element as one controls its group index. However, in practical situations, the temporal shape of a pulse can change. To understand better this point, we take a second look on the frequency-domain analysis of pulse propagation through a linear medium. To take into account more practical situations, we take the refractive index

of the medium to be complex and frequency dependent.

The time-dependent field at the entrance plane of a slow-light medium can alternatively be represented by a span of plane waves at different frequencies through the following Fourier transform relation:

$$\mathcal{E}(z = 0, t) = \int_{\omega=-\infty}^{\infty} E(z = 0, \omega) e^{i\omega t} d\omega. \quad (1.16)$$

Each frequency component propagates through the medium of length  $L$  as follows:

$$E(z = L, \omega) = E(z = 0, \omega) e^{ik'L - k''L}, \quad (1.17)$$

where  $k'$  and  $k''$  are the real and imaginary part of the wave number at frequency  $\omega$  inside the medium. Furthermore, one can expand  $k'(\omega)$  using a Taylor series around the carrier frequency  $\omega_0$  as follows:

$$\begin{aligned} k'(\omega) &= k'_0(\omega_0) + \left. \frac{dk'}{d\omega} \right|_{\omega_0} (\omega - \omega_0) + \frac{1}{2!} \left. \frac{d^2k'}{d\omega^2} \right|_{\omega_0} (\omega - \omega_0)^2 + \dots \\ &= k'_0(\omega_0) + \frac{n_g(\omega_0)}{c} (\omega - \omega_0) + \frac{1}{2!} \left. \frac{d^2k'}{d\omega^2} \right|_{\omega_0} (\omega - \omega_0)^2 + \dots \\ &= k'_0(\omega_0) + \beta_1 \Delta\omega + \frac{1}{2!} \beta_2 \Delta\omega^2 + \dots, \end{aligned} \quad (1.18)$$

where

$$\beta_j \equiv \left. \frac{d^j k'}{d\omega^j} \right|_{\omega_0}, \quad (1.19)$$

is the  $j$ th order dispersion of the wave propagation constant at center frequency  $\omega_0$ , and  $\Delta\omega = \omega - \omega_0$  is the frequency detuning from the center frequency  $\omega_0$ . Thus, the

time-dependent field at the exit plane of the medium is given by

$$\begin{aligned}
\mathcal{E}(z = L, t) &= \int_{-\infty}^{\infty} d\omega E(z = L, \omega) e^{-i\omega t}, \\
&= \int_{-\infty}^{\infty} d\omega E(z = 0, \omega) e^{ik'z - k''z} e^{-i\omega t}, \\
&= \int_{-\infty}^{\infty} d\omega E(z = 0, \omega) e^{-k''z} e^{-i\omega t} \\
&\quad \times \exp \left\{ i \left[ k'_0(\omega_0) + \frac{n_g(\omega_0)}{c} \Delta\omega + \frac{\beta_2}{2!} \Delta\omega^2 + \dots \right] L \right\}. \quad (1.20)
\end{aligned}$$

In the ideal case in which the second- and higher-order dispersion terms are zero, i.e.,  $\beta_j = 0$  for  $j \geq 2$ , and the imaginary part of the wave vector  $k'' = 0$ , the output field becomes

$$\begin{aligned}
\mathcal{E}(z = L, t) &= \int_{-\infty}^{\infty} d\omega E(z = 0, \omega) e^{ik'_0(\omega_0)L + i\beta_1(\omega - \omega_0)L} e^{-i\omega t} \\
&= \mathcal{E} \left( z = 0, \left( t - \frac{n_g L}{c} \right) \right). \quad (1.21)
\end{aligned}$$

One can see that, in this ideal case, the output field has the same temporal shape of the input pulse, but with a temporal shift equal to the group delay of the medium  $\Delta T = n_g L/c$ .

However, a practical slow-light medium has non-vanishing higher-order dispersions as well as some associated gain or loss. Thus, there are at least three mechanisms that will cause the temporal shape of the output pulse to be different from the input signal.

The first factor is the change in the magnitude of the signal after propagating through a slow-light medium. In different scenarios, one can see this point either from the change in the magnitude of the signal spectrum, or from the change in the peak intensity of the temporal pulse.

The second factor is the frequency-dependent gain/loss of the medium, which causes reshaping of the signal spectrum and consequently causes pulse distortion.

This is sometimes referred to as the amplitude distortion [35].

The third factor is the higher order dispersion ( $\frac{1}{2!}\beta_2(\omega - \omega_0)^2 + \frac{1}{3!}\beta_3(\omega - \omega_0)^3 + \dots$ ). Since higher dispersion changes the relative phase relation among different frequency components, it also leads to pulse distortion, which is also referred to as the phase distortion [35].

When all of the above factors are considered, both the shape and the magnitude of the output pulse will inevitably be more and more different from those of the input pulse as the delay increases. Therefore, it is important to optimize the complex refractive index profile of a slow-light media to maximize the performance of a slow-light delay element. Furthermore, it would also be of practical convenience to design slow-light based modules that can have other properties, such as a single module that can provide both tunable delay and advancement at the same time, a module to provide tunable packet delays, and so on.

Such frequency-dependent gain and group index also put practical limits on the performance of slow light in other applications, such as interferometry, as well. Thus, it is worthwhile to investigate the consequences or practical performance for specific applications.

## 1.4 **Remainder of the thesis**

Following the leads of the general interests for “slow light”, my thesis includes studies regarding some fundamental issues of slow light as well as specific applications. The remainder of my thesis is organized as follows.

Chapters 2 and 3 deal primarily with two fundamental aspects of slow light. It includes a study on the momentum of photons inside dispersive media, and a study on the noise property of slow-light media based on amplifiers/attenuators.

The derivation of the momentum of a photon in a dispersive medium starts with the long-time debate between the Abraham [36] and Minkowski [37] forms . I then

study how these different definitions are modified when dispersion needs to be considered, and what force a slow-light medium is experienced when a photon enters or leaves it.

Microscopic slow and fast light are typically associated with some gain or absorption feature. Hence, it is natural to ask the question: “how is the noise property of an optical signal field modified after propagating through a slow- or fast-light medium?” I include some study to answer this question under both ideal and more realistic scenarios using a quantized field approach.

Chapters 4, 5 and 6 focus mainly on applications of using slow light for optical delay lines and on how to improve the performance of fiber-based tunable delay lines using, e.g., stimulated Brillouin scattering (SBS). Chapter 4 describes an approach to increase the maximum fractional delay by optimizing the shape of a gain profile. The optimization utilizes multiple closely spaced gain lines, and the free parameters include the frequency separation between neighboring lines and the relative strength of individual lines. The gain profile is optimized under separate considerations for single pulses as well as for random data trains, during which different metrics are used to quantify the signal distortion and to define the relative delay.

In chapter 5, I present an approach to achieve simultaneously delay and advancement using slow and fast light in a single module. The design of such a bi-directionally tunable temporal adjustment element is based on a reconfigurable gain profile, and is demonstrated using SBS slow light in a single mode fiber.

In chapter 6, I investigate a more fundamental limit, the Miller limit [38], that is imposed on the maximum achievable fractional delay that a slow-light element can achieve. In particular, I propose and demonstrate numerically a realistic design of a channelized delay device which, by using a finite number of spatially separated channels, can overcome Miller’s limit. Furthermore, we show that such a device can achieve discretely tunable optical packet delays without the need of dynamically controlling the phase of each channel.

The last part of my thesis, chapters 7–10, explore the use of slow light to enhance the spectroscopic performance of interferometers. It starts with Chapter 7 in which I first investigate the role of group index in the spectral response of two-beam and multiple-beam interferometers. The theoretical prediction is demonstrated experimentally on a slow-light wedged-shear interferometer. Limitations on the enhanced performance is then analyzed under practical considerations.

In Chapter 8, I present a design to utilize tunable slow light to construct a new type of Fourier–transform interferometer (FTI). I show that the Fourier transform of the spectrum of the input signal can be obtained as one continuously changes the group index of the medium, and therefore that such a SLFTI does not need any mechanical moving parts and can achieve much higher spectral resolution as compared to a conventional FTI. Following an experimental demonstration, I also analyze the performance of such a SL–FTI under practical considerations.

In Chapter 9, I attempts to answer the general question of what types of slow light processes are suitable for spectroscopic interferometry applications. In specific, three types of realistic slow-light processes are examined, namely, a Lorentzian-shaped gain line medium, a double absorption line medium, and an electromagnetically-induced-transparency (EIT) medium.

While using a slow-light medium can enhance the spectral performance of an interferometer by a factor equal to the group index, one can also reduce the size of the interferometer by the same factor without sacrificing the spectral performance. Thus, I propose in Chapter 10 a design of an integrated spectrometer that can have high spectral resolution using on-chip slow-light technologies. In specific, I propose a new flat–band slow–light photonic crystal line defect waveguide that can be incorporated into the on-chip spectrometer design.

# Chapter 2

## Photon Momentum in Dispersive Dielectric Media

### 2.1 Background

As a particle carries a momentum given by the product of its mass  $m$  and its velocity  $v$ , a photon also carries a momentum. In vacuum, the momentum carried by a photon is simply  $\hbar\omega/c$ , but electromagnetic momentum in a dielectric medium is a subject that have been extensively studied both theoretically and experimentally [39], and the debate of the correct form of the momentum density of an electromagnetic field or the momentum carried by a photon still goes on. There are two most favored forms, the Abraham [36] and Minkowski [37] forms. Over the years, there are a bewildering array of experimental studies and associated theoretical analyses [40] to support either Abraham or Minkowski form. However, an aspect of this subject that has received surprisingly little attention concerns the effects of dispersion on the Minkowski and Abraham momenta and on the electromagnetic forces on polarizable particles. This chapter tries to address such effects, which might help to clarify the physical interpretation of the Abraham and Minkowski momenta and the distinction between them.

## 2.2 Photon momentum in non-dispersive media

We first review briefly the Abraham and Minkowski momenta for the situation usually considered when a dielectric medium is assumed to be dispersionless and non-absorbing near a frequency  $\omega$ . The Abraham and Minkowski momentum densities are given by

$$\mathbf{P}_A = \frac{1}{c^2} \mathbf{E} \times \mathbf{H}, \quad (2.1)$$

$$\mathbf{P}_M = \mathbf{D} \times \mathbf{B}, \quad (2.2)$$

where the subscript  $A$  and  $M$  denote Abraham and Minkowski, respectively.

Here we assume that the permeability  $\mu$  of the medium is equal to that of the vacuum  $\mu_0$ . For a plane wave, the relation between different components of the electromagnetic fields is given by

$$\mathbf{E} = \mathbf{E}_\omega e^{-i\omega t}, \quad (2.3)$$

$$\mathbf{H} = \mathbf{H}_\omega e^{-i\omega t}, \quad (2.4)$$

$$\mathbf{D}_\omega = \epsilon \mathbf{E}_\omega = \epsilon_0 n^2 \mathbf{E}_\omega, \quad (2.5)$$

$$\mathbf{B}_\omega = \mu_0 \mathbf{H}_\omega, \quad (2.6)$$

$$\mathbf{H}_\omega^2 = (\epsilon \mu_0) \mathbf{E}_\omega^2. \quad (2.7)$$

From  $\mathbf{D} = \epsilon_0 n^2 \mathbf{E}$  it follows that

$$\frac{\partial \mathbf{P}_M}{\partial t} = \frac{\partial \mathbf{P}_A}{\partial t} + \mathbf{f}^A, \quad (2.8)$$

where

$$\mathbf{f}^A = \frac{1}{c^2} (n^2 - 1) \frac{\partial}{\partial t} (\mathbf{E} \times \mathbf{H}) \quad (2.9)$$

is the *Abraham force density*.

To derive the momentum carried by a single photon, we need to use the quantized field approach. The standard quantization of the electromagnetic field in a non-dispersive medium gives the following results:

$$\hat{\mathbf{E}}(\mathbf{r}, t) = \frac{1}{\sqrt{V}} \sum_{\mathbf{k}} \sum_s \left( \frac{\hbar\omega}{2n^2\epsilon_0} \right)^{1/2} [i\hat{a}_{\mathbf{k}s}(0)\epsilon_{\mathbf{k}s}e^{i(\mathbf{k}\cdot\mathbf{r}-\omega t)} + \text{h.c.}], \quad (2.10)$$

$$\hat{\mathbf{B}}(\mathbf{r}, t) = \frac{1}{\sqrt{V}} \sum_{\mathbf{k}} \sum_s \left( \frac{\hbar}{2\omega n^2\epsilon_0} \right)^{1/2} [i\hat{a}_{\mathbf{k}s}(0)(\mathbf{k} \times \epsilon_{\mathbf{k}s})e^{i(\mathbf{k}\cdot\mathbf{r}-\omega t)} + \text{h.c.}], \quad (2.11)$$

where  $V$  is the quantization volume,  $\mathbf{k}$  is the wave vector, and  $s$  is the polarization. Using such quantized field approach, one can obtain the expressions for the magnitudes of the Abraham and Minkowski momenta for single photons as follows:

$$p_A = \frac{1}{n} \frac{\hbar\omega}{c}, \quad (2.12)$$

$$p_M = n \frac{\hbar\omega}{c}, \quad (2.13)$$

where  $n$  is the refractive index of the medium at frequency  $\omega$ . For single-photon fields, the momentum  $p^A$  associated with the Abraham force is given by

$$p^A = \frac{(n^2 - 1)}{n} \frac{\hbar\omega}{c}, \quad (2.14)$$

and the relation between the Abraham and Minkowski momenta of a single photon becomes

$$p_M = p_A + p^A. \quad (2.15)$$

## 2.3 Photon momentum in dispersive media

We first recall the expression for the total cycle-averaged energy density when a plane-wave monochromatic field propagates in a dispersive dielectric at a frequency  $\omega$  at which absorption is negligible [41] (see also Sec 2.8):

$$u = \frac{1}{4} \left[ \frac{d}{d\omega} (\epsilon\omega) \mathbf{E}_\omega^2 + \mu_0 \mathbf{H}_\omega^2 \right], \quad (2.16)$$

or equivalently, in terms of  $\mathbf{E}_\omega$  and the group index  $n_g = d(n\omega)/d\omega$ ,

$$u = \frac{1}{2} \epsilon_0 n n_g \mathbf{E}_\omega^2. \quad (2.17)$$

When the field is quantized in a volume  $V$ ,  $u$  is in effect replaced by  $q\hbar\omega/V$ , where  $q$  is the expectation value of the photon number in the volume  $V$ . Therefore, from Eq. (2.17),  $\mathbf{E}_\omega^2$  is effectively equal to  $2\hbar\omega/(\epsilon_0 n n_g V)$  per photon. Thus, for single photons, the Abraham momentum defined by Eq. (2.1) becomes

$$p_A = \frac{n}{c} \frac{1}{2} \epsilon_0 \frac{2\hbar\omega}{\epsilon_0 n n_g V} V = \frac{1}{n_g} \frac{\hbar\omega}{c}. \quad (2.18)$$

Similarly, the Minkowski momentum becomes

$$p_M = \frac{n^2}{n_g} \frac{\hbar\omega}{c}, \quad (2.19)$$

which follows from the definition in Eq. (2.1) and the relation  $\mathbf{D} = \epsilon_0 n^2 \mathbf{E}$ . We now have the following relation between the Abraham and Minkowski momenta in a dispersive medium:

$$p_M = n^2 p_A. \quad (2.20)$$

These same expressions for  $p_A$  and  $p_M$  can be obtained more formally by quantizing

the fields  $\mathbf{E}$ ,  $\mathbf{D}$ ,  $\mathbf{H}$ , and  $\mathbf{B}$  in a dispersive medium [42].

Two examples serve to clarify the differences among the momenta involved in the momentum exchange between light and matter. The first example is based on an argument of Fermi's that the Doppler effect is a consequence of this momentum exchange [43], as follows.

Consider an atom of mass  $M$  inside a host dielectric medium with refractive index  $n(\omega)$ . The atom has a sharply defined transition frequency  $\omega_0$  and is initially moving with velocity  $v$  away from a source of light of frequency  $\omega$ . Because the light in the atom's reference frame has a Doppler-shifted frequency  $\omega(1 - nv/c)$  determined by the phase velocity ( $c/n$ ) of light in the medium, the atom can absorb a photon if  $\omega(1 - nv/c) = \omega_0$ , or if

$$\omega \cong \omega_0(1 + nv/c). \quad (2.21)$$

We denote the momentum associated with a photon in the medium by  $\wp$  and consider the implications of (nonrelativistic) energy and momentum conservation. The initial energy is  $E_i = \hbar\omega + \frac{1}{2}Mv^2$ , and the final energy, after the atom has absorbed a photon, is  $\frac{1}{2}Mv'^2 + \hbar\omega_0$ , where  $v'$  is the velocity of the atom after absorption. The initial momentum is  $\wp + Mv$ , and the final momentum is just  $Mv'$ . Therefore

$$\frac{1}{2}M(v'^2 - v^2) \cong Mv(v' - v) = Mv(\wp/M) = \hbar(\omega - \omega_0), \quad (2.22)$$

or  $\omega \cong \omega_0 + \wp v/\hbar$ . From Eq. (2.21) and  $\omega \cong \omega_0$  we conclude that

$$\wp = n \frac{\hbar\omega}{c}. \quad (2.23)$$

Thus, once we accept the fact that the Doppler shift depends on the refractive index of the medium according to Eq. (2.21), we are led by energy and momentum conservation to conclude that an atom in the medium must recoil with momentum Eq. (2.23) when

it absorbs (or emits) a photon of energy  $\hbar\omega$ . Momentum conservation in this example is discussed in more detail below.

In our second example we consider, following Balazs [44], a rigid block of mass  $M$ , refractive index  $n$ , and length  $a$ , initially sitting at rest on a frictionless surface. A single-photon pulse of frequency  $\omega$  passes through the block, which is assumed to be non-absorbing at frequency  $\omega$  and to have anti-reflection coatings on its front and back surfaces. The length  $a$  of the block is presumed to be much larger than the length of the pulse. If the photon momentum is  $\wp_{\text{in}}$  inside the block and  $\wp_{\text{out}}$  outside, the block picks up a momentum  $MV = \wp_{\text{out}} - \wp_{\text{in}}$  when the pulse enters. If the space outside the block is vacuum,  $\wp_{\text{out}} = mc$ , where  $m = E/c^2 = \hbar\omega/c^2$ . Similarly  $\wp_{\text{in}} = mv_p$ , where  $v_p$  is the velocity of light in the block. Without dispersion,  $v_p = c/n$  and the momentum of the photon in the block is evidently  $\wp_{\text{in}} = mc/n = \hbar\omega/nc$ . The effect of dispersion is to replace  $v_p = c/n$  by  $v_g = c/n_g$  and  $\wp_{\text{in}} = \hbar\omega/nc$  by  $\wp_{\text{in}} = \hbar\omega/n_g c$ . With or without dispersion, this example suggests that the photon momentum in the medium has the Abraham form. Note that the essential feature of Balazs's argument is simply that the velocity of light in the medium is  $v_p$  (or, more generally,  $v_g$ ). This, together with momentum conservation, is what leads him to conclude that the momentum of the field has the Abraham form.

This prediction can in principle be tested experimentally. Conservation of momentum requires, according to Balazs's argument, that  $MV = m(c - v_g)$ . When the pulse exits the block, the block recoils and comes to rest, and is left with a net displacement

$$\Delta x = V\Delta t = \frac{m}{M}(c - v_g)\frac{a}{v_g} = \frac{\hbar\omega}{Mc^2}(n_g - 1)a \quad (2.24)$$

as a result of the light having passed through it. This is the prediction for the net displacement based on the momentum  $p_A$  given in Eq. (2.18). If the photon momentum inside the block were assumed to have the Minkowski form  $n^2\hbar\omega/cn_g$  given in Eq. (2.19), however, the displacement of the block would in similar fashion

be predicted to be

$$\Delta x = \frac{\hbar\omega}{Mc^2}a(n_g - n^2), \quad (2.25)$$

and if it were assumed to be  $n\hbar\omega/c$ , as in Eq. (2.23), the prediction would be that the net displacement of the block is

$$\Delta x = \frac{\hbar\omega}{Mc^2}an_g(1 - n). \quad (2.26)$$

These different assumptions about the photon momentum can lead to different predictions not only for the magnitude of the block displacement but also for its direction.

The first (Doppler) example suggests at first thought that the momentum of the photon is  $n\hbar\omega/c$  [Eq. (2.23)], while the second (Balazs) example indicates that it is  $\hbar\omega/n_gc$ . Let us consider more carefully the first example. There is ample experimental evidence that the Doppler shift is  $nv\omega/c$  regardless of dispersion, as we have assumed, but does this imply that the momentum of a photon in a dielectric is in fact  $n\hbar\omega/c$ ? We will show in the following section that the forces exerted by a plane monochromatic wave on the polarizable particles of a dielectric result in a momentum density of magnitude

$$p_{\text{med}} = \frac{\epsilon_0}{2c}n(nn_g - 1)E_\omega^2 = \left(n - \frac{1}{n_g}\right)\frac{\hbar\omega}{c}\frac{1}{V}; \quad (2.27)$$

the second equality applies to a single photon, and follows from the replacement of  $\mathbf{E}_\omega^2$  by  $2\hbar\omega/(\epsilon nn_g V)$ , as discussed earlier. Now from the fact that the Doppler shift implies that an absorber (or emitter) inside a dielectric recoils with momentum  $n\hbar\omega/c$ , all we can safely conclude from momentum conservation is that a momentum  $n\hbar\omega/c$  is taken from (or given to) the *combined system of field and dielectric*. Given that the medium has a momentum density Eq. (2.27) due to the force exerted on it by the propagating field, we can attribute to the field (by conservation of momentum) a

momentum density

$$n \frac{\hbar\omega}{c} \frac{1}{V} - P_{\text{med}} = \frac{1}{n_g} \frac{\hbar\omega}{c} \frac{1}{V} = p_A. \quad (2.28)$$

That is, the momentum of the field in this interpretation is given by the Abraham formula, consistent with the conclusion of the Balazs thought experiment. The recoil momentum  $n\hbar\omega/c$ , which in general differs from both the Abraham and the Minkowski momenta, evidently gives the momentum not of the field as such but of the combined system of field plus dielectric. It is the momentum density equal to the *total* energy density  $u = \hbar\omega/V$  for a monochromatic field divided by the phase velocity  $c/n$  of the propagating wave. As already mentioned, experiments on the recoil of objects immersed in dielectric media have generally indicated that the recoil momentum is  $n\hbar\omega/c$  per unit of energy  $\hbar\omega$  of the field, just as in the Doppler effect. But this should not be taken to mean that  $n\hbar\omega/c$  is the momentum of a “photon” existing independently of the medium in which the field propagates. Regardless of how this momentum is apportioned between the field and the medium in which it propagates, the important thing for the theory, of course, is that it correctly predicts the *observable forces* exerted by electromagnetic fields. We next turn our attention specifically to the forces acting on polarizable particles in an applied electromagnetic field.

## 2.4 Momenta and force on polarizable particles

To calculate the force on polarizable particles, We take the electric dipole approximation and assume that frequency components of the field is far enough from any transition resonance center such that the absorption is negligible. Then the induced electric dipole moment of a particle in a field of frequency  $\omega$  is

$$\mathbf{d} = \alpha(\omega)\mathbf{E}_\omega \exp(-i\omega t), \quad (2.29)$$

and the polarizability  $\alpha(\omega)$  may be taken to be real. With these assumptions we now consider the forces acting on such particles in applied, quasi-monochromatic fields.

We begin with the Lorentz force on an electric dipole moment  $\mathbf{d}$  in an electromagnetic field [45]:

$$\begin{aligned}\mathbf{F} &= (\mathbf{d} \cdot \nabla)\mathbf{E} + \dot{\mathbf{d}} \times \mathbf{B} \\ &= (\mathbf{d} \cdot \nabla)\mathbf{E} + \mathbf{d} \times (\nabla \times \mathbf{E}) + \frac{\partial}{\partial t}(\mathbf{d} \times \mathbf{B}) \\ &\equiv \mathbf{F}_E + \mathbf{F}_B,\end{aligned}\tag{2.30}$$

where we define

$$\mathbf{F}_E = (\mathbf{d} \cdot \nabla)\mathbf{E} + \mathbf{d} \times (\nabla \times \mathbf{E}),\tag{2.31}$$

$$\mathbf{F}_B = \frac{\partial}{\partial t}(\mathbf{d} \times \mathbf{B}).\tag{2.32}$$

In writing the second equality in Eq. (2.30) we have used the Maxwell equation  $\partial\mathbf{B}/\partial t = -\nabla \times \mathbf{E}$ . The dipole moment of interest here is induced by the electric field. Writing

$$\mathbf{E} = \mathcal{E}_0(\mathbf{r}, t)e^{-i\omega t} = e^{-i\omega t} \int_{-\infty}^{\infty} d\Delta \tilde{\mathcal{E}}_0(\mathbf{r}, \Delta)e^{-i\Delta t},\tag{2.33}$$

in which  $|\partial\mathcal{E}_0/\partial t| \ll \omega|\mathcal{E}_0|$  for a quasi-monochromatic field, we approximate  $\mathbf{d}$  as follows:

$$\begin{aligned}\mathbf{d}(\mathbf{r}, t) &= \int_{-\infty}^{\infty} d\Delta \alpha(\omega + \Delta) \tilde{\mathcal{E}}_0(\mathbf{r}, \Delta) e^{-i(\omega + \Delta)t} \\ &\cong \int_{-\infty}^{\infty} d\Delta [\alpha(\omega) + \Delta\alpha'(\omega)] \tilde{\mathcal{E}}_0(\mathbf{r}, \Delta) e^{-i(\omega + \Delta)t} \\ &= \left[ \alpha(\omega)\mathcal{E}_0(\mathbf{r}, t) + i\alpha'(\omega)\frac{\partial\mathcal{E}_0}{\partial t} \right] e^{-i\omega t}.\end{aligned}\tag{2.34}$$

Here  $\alpha' = d\alpha/d\omega$  and we assume that higher-order dispersion is sufficiently weak that the terms  $d^m\alpha/d\omega^m$  can be neglected for  $m \geq 2$ . Putting Eq. (2.34) into Eq. (2.31), we obtain after some straightforward manipulations and cycle-averaging the force

$$\mathbf{F}_E = \nabla \left[ \frac{1}{4}\alpha(\omega)|\mathcal{E}|^2 \right] + \frac{1}{4}\alpha'(\omega)\mathbf{k}\frac{\partial}{\partial t}|\mathcal{E}|^2, \quad (2.35)$$

where  $\mathcal{E}$  and  $\mathbf{k}$  are defined by writing  $\mathcal{E}_0(\mathbf{r}, t) = \mathcal{E}(\mathbf{r}, t)e^{i\mathbf{k}\cdot\mathbf{r}}$ . Since the refractive index  $n$  of a medium in which local field corrections are negligible is given in terms of  $\alpha$  by  $n^2 - 1 = N\alpha/\epsilon_0$ ,  $N$  being the density of dipoles in the dielectric, we have  $\alpha' = (2n\epsilon_0/N)(dn/d\omega)$  and

$$\mathbf{F}_E = \nabla \left[ \frac{1}{4}\alpha(\omega)|\mathcal{E}|^2 \right] + \frac{\epsilon_0}{2N}\mathbf{k}n\frac{dn}{d\omega}\frac{\partial}{\partial t}|\mathcal{E}|^2. \quad (2.36)$$

The first term is the ‘‘dipole force’’ associated with the energy  $W = -\frac{1}{2}\alpha(\omega)\mathbf{E}^2$  involved in inducing an electric dipole moment in an electric field:

$$W = -\int_0^{\mathbf{E}} \mathbf{d} \cdot d\mathbf{E} = -\alpha(\omega) \int_0^{\mathbf{E}} \mathbf{E} \cdot d\mathbf{E} = -\frac{1}{2}\alpha(\omega)\mathbf{E}^2. \quad (2.37)$$

The second term in Eq. (2.36) is nonvanishing only because of dispersion ( $dn/d\omega \neq 0$ ). It is in the direction of propagation of the field, and implies for a uniform density  $N$  of atoms per unit volume a momentum density of magnitude

$$P_D = \frac{1}{2}\epsilon_0 n^2 \frac{dn}{d\omega} \frac{\omega}{c} |\mathcal{E}|^2 = \frac{1}{2} \frac{\epsilon_0}{c} n^2 (n_g - n) |\mathcal{E}|^2, \quad (2.38)$$

since  $k = n(\omega)\omega/c$ . This momentum density comes specifically from the dispersion ( $dn/d\omega$ ) of the medium.

The force  $\mathbf{F}_B$  defined by Eq. (2.32), similarly, implies a momentum density  $\mathbf{P}^A$  imparted to the medium:

$$\mathbf{P}^A = N\mathbf{d} \times \mathbf{B}. \quad (2.39)$$

As the notation suggests, this momentum density is associated with the Abraham force density Eq. (2.9). The result of a straightforward evaluation of  $\mathbf{P}^A$  based on Eq. (2.34) and  $\nabla \times \mathbf{E} = -\partial\mathbf{B}/\partial t$  is

$$\mathbf{P}^A = \frac{1}{2}\epsilon_0(n^2 - 1)\frac{\mathbf{k}}{\omega}|\mathcal{E}|^2, \quad (2.40)$$

$$|\mathbf{P}^A| = P^A = \frac{1}{2}\frac{\epsilon_0}{c}n(n^2 - 1)|\mathcal{E}|^2, \quad (2.41)$$

when we use  $\mathbf{k} \cdot \mathbf{E} = 0$  and our assumption that  $|\dot{\mathcal{E}}_0| \ll \omega|\mathcal{E}_0|$ . The magnitude of the total momentum density in the medium due to the force of the field on the dipoles is therefore

$$\begin{aligned} P_{\text{med}} = P_D + P^A &= \frac{\epsilon}{2c} [n^2(n_g - n) + n(n^2 - 1)] |\mathcal{E}|^2 \\ &= \frac{\epsilon_0}{2c} n(nn_g - 1) |\mathcal{E}|^2 \end{aligned} \quad (2.42)$$

in the approximation in which the field is sufficiently uniform that we can ignore the dipole force  $\nabla[\frac{1}{4}\alpha|\mathcal{E}|^2]$ .

The complete momentum density for the field and the medium is obtained by adding to Eq. (2.42) the Abraham momentum density  $P_A$  of the field. According to Eq. (2.1),  $P_A = (\epsilon_0/2c)n|\mathcal{E}|^2$ , and so the total momentum density is

$$P_A + P_D + P^A = \frac{\epsilon}{2c} [n + n(nn_g - 1)] |\mathcal{E}|^2 = \frac{\epsilon}{2c} n^2 n_g |\mathcal{E}|^2 \quad (2.43)$$

if the dipole force is negligible.

To express these results in terms of single photons, we again replace  $|\mathcal{E}_0|^2$  by  $2\hbar\omega/(\epsilon n n_g V)$ ; Eq. (2.43) then takes the form

$$p_A + p_D + p^A = n \frac{\hbar\omega}{c} \frac{1}{V}, \quad (2.44)$$

which is consistent with the discussion in the preceding section. This is the total

momentum density per photon, assuming that the dipole force is negligible. The momentum density of the medium per photon follows from Eq. (2.42):

$$\begin{aligned} p_{\text{med}} &= p_D + p^A = \frac{\epsilon}{2c} n(nn_g - 1) \frac{2\hbar\omega}{nn_g\epsilon_0 V} \\ &= \left(n - \frac{1}{n_g}\right) \frac{\hbar\omega}{c} \frac{1}{V}, \end{aligned} \quad (2.45)$$

as stated earlier in Eq. (2.27).

Consider the example of spontaneous emission by a guest atom in a host dielectric medium. The atom loses energy  $\hbar\omega_0$ , and the quantum (photon in the medium) of excitation carries away from the atom not only this energy but also a linear momentum  $n\hbar\omega/c$  [see Eq. (2.44)]. The atom therefore recoils with momentum  $n\hbar\omega/c$  [46].

The momentum density of Eq. (2.38) was obtained by Nelson [47] in a rigorous treatment of a deformable dielectric based on a Lagrangian formulation. Here a dielectric medium is treated as an idealized rigid body. From a microscopic perspective, this part of the momentum density of the medium is attributable directly to the second term on the right-hand side of Eq. (2.34), i.e., to the part of the induced dipole moment that arises from dispersion, which is a general property of induced dipole moments in applied fields. Consider, for example, a two-level atom driven by a quasi-monochromatic field with frequency  $\omega$  far-detuned from the atom's resonance frequency  $\omega_0$ . In the standard  $u, v$  notation for the off-diagonal components of the density matrix in the rotating-wave approximation [48],

$$u(t) - iv(t) \cong \frac{1}{\Delta} \chi(t) + \frac{i}{\Delta^2} \frac{\partial \chi}{\partial t} + \dots, \quad (2.46)$$

where  $\chi(t)$  is the Rabi frequency and  $\Delta$  is the frequency detuning. The polarizability is proportional to  $1/\Delta$  in this approximation, and therefore Eq. (2.46) is just a special case of Eq. (2.34).

## 2.5 Change of momenta between light and particles

We next consider the momentum exchange between a plane-wave *pulse* and a single polarizable particle. We will assume again that the particle is characterized by a real polarizability  $\alpha(\omega)$  and that it is surrounded by a host medium with refractive index  $n_b(\omega)$ . The electric field is assumed to be

$$\mathbf{E}(z, t) = \mathcal{E}(t - z/v_{bg}) \cos(\omega t - kz), \quad (2.47)$$

with  $k = n_b(\omega)\omega/c$  and group velocity  $v_{bg} = c/n_{bg}$ ,  $n_{bg} = (d/d\omega)(\omega n_b)$ .

The force acting on the particle is  $\mathbf{F}_E + \mathbf{F}_B$ . By multiplying Eq. (2.41) by a volume  $V$  describing the pulse, replacing  $n^2 - 1$  by  $N\alpha/\epsilon_0$  with  $NV = 1$  for the single particle, and differentiation with respect to time,  $\mathbf{F}_B$  reduces to  $\frac{1}{2}\alpha(\omega)(\mathbf{k}/\omega)(\partial/\partial t)|\mathcal{E}|^2$ .  $\mathbf{F}_E$  follows from Eq. (2.35). Then the force acting on the particle is in the  $z$  direction and has the (cycle-averaged) magnitude

$$F = \frac{1}{4}\alpha(\omega)\frac{\partial}{\partial z}\mathcal{E}^2 + \frac{1}{4}\alpha'(\omega)n_b(\omega)\frac{\omega}{c}\frac{\partial}{\partial t}\mathcal{E}^2 + \frac{1}{2c}\alpha(\omega)n_b(\omega)\frac{\partial}{\partial t}\mathcal{E}^2, \quad (2.48)$$

where now we retain the dipole force, given by the first term on the right-hand side.

The momentum of the particle at  $z$  at time  $T$  is

$$\begin{aligned} p &= \int_{-\infty}^T F dt = \frac{1}{4}\alpha \int_{-\infty}^T \frac{\partial}{\partial z}\mathcal{E}^2(t - z/v_{bg}) dt \\ &\quad + \frac{1}{4c}\alpha' n_b \omega \int_{-\infty}^T \frac{\partial}{\partial t}\mathcal{E}^2(t - z/v_{bg}) dt + \frac{1}{2c}\alpha n_b \int_{-\infty}^T \frac{\partial}{\partial t}\mathcal{E}^2(t - z/v_{bg}) dt \\ &= -\frac{1}{4}\alpha \frac{1}{v_{bg}}\mathcal{E}^2 + \frac{n_b}{4c}\alpha' \omega \mathcal{E}^2 + \frac{1}{2}\alpha \frac{n_b}{c}\mathcal{E}^2 \\ &= \frac{1}{4c}[(2n_b - n_{bg})\alpha + n_b \omega \alpha']\mathcal{E}^2(T - z/v_{bg}). \end{aligned} \quad (2.49)$$

Hinds and Barnett [40] have considered the force on a two-level atom due to a

pulse of light in free space. In this case  $\bar{n}_b = n_{bg} = 1$  and Eq. (2.49) reduces to

$$p = \frac{1}{4c}[\alpha + \omega\alpha']\mathcal{E}^2. \quad (2.50)$$

Following Hinds and Barnett, we argue that a pulse occupying the volume  $V$  in the neighborhood of the atom in free space corresponds to a number  $q = \frac{1}{2}\epsilon_0\mathcal{E}^2V/\hbar\omega$  of photons, so that

$$p = \frac{1}{2c}[\alpha + \omega\alpha']\frac{\hbar\omega}{\epsilon_0V}q. \quad (2.51)$$

We recall that  $\alpha = \epsilon_0(n^2 - 1)/N$ , where  $n$  is the refractive index in the case of  $N$  polarizable particles per unit volume. Then

$$\begin{aligned} p &= \frac{1}{2c} \left[ \frac{\epsilon_0(n^2 - 1)}{N} + \frac{2\epsilon_0n}{N}\omega\frac{dn}{d\omega} \right] \frac{\hbar\omega}{c}q \\ &\cong [n - 1 + \omega\frac{dn}{d\omega}] \frac{\hbar\omega}{c}q \equiv K \frac{\hbar\omega}{c}q. \end{aligned} \quad (2.52)$$

This is the momentum imparted to the particle, which implies that a change in the *field* momentum per photon equal to

$$\frac{\hbar\omega}{c}[1 - K] \cong \frac{\hbar\omega}{c} \frac{1}{1 + K} = \frac{\hbar\omega}{n_g c} \quad (2.53)$$

if  $|K| \ll 1$ , where  $n_g = (d/d\omega)(n\omega)$ . As in the case of a two-level atom considered by Hinds and Barnett, this corresponds to the Abraham momentum; our result simply generalizes theirs in replacing  $n$  by  $n_g$  in the expression for the change in photon momentum.

In the case of a polarizable particle in a host dielectric rather than in free space we obtain, from Eq. (2.49),

$$p = \frac{I}{2\epsilon_0c^2} \left[ \left(2 - \frac{n_{bg}}{n_b}\right)\alpha + \omega\alpha' \right], \quad (2.54)$$

where the intensity  $I = (1/2)c\epsilon_0 n_b \mathcal{E}^2$ . If dispersion in the medium and in the polarizability of the guest particle are negligible, we can set  $n_{bg} = n$  and  $\alpha' = 0$ , and then Eq. (2.54) reduces to a well known expression [e.g., Eq.(2.7) in Ref. [49]]. However, this momentum can be large in a slow-light medium ( $n_{bg}$  large), for example, because the gradient of the field Eq. (2.47) responsible for the dipole force on the particle is large [50]; this is a consequence of the spatial compression of a pulse in a slow-light medium. We discuss this case further in the next Section.

## 2.6 Force on a dielectric sphere

The expression of Eq. (2.48) for the force on a polarizable particle in a field [Eq. (2.47)] may be generalized to allow for absorption by the particle simply by taking the polarizability  $\alpha(\omega)$  in Eq. (2.34) to be complex. Assuming again that  $\mathcal{E}$  is slowly varying in time compared to  $\exp(-i\omega t)$ , and slowly varying in space compared to  $\exp(ikz)$ , we obtain

$$F = \frac{1}{4c}[(2n_b - n_{bg})\alpha_R + n_b\omega\alpha'_R]\frac{\partial}{\partial\tau}|\mathcal{E}|^2 + \frac{1}{2}n_b\frac{\omega}{c}\alpha_I|\mathcal{E}|^2, \quad (2.55)$$

where  $\tau = t - n_{bg}z/c$  and  $\alpha_R$  and  $\alpha_I$  are the real and imaginary parts, respectively, of the complex polarizability  $\alpha(\omega)$ . If we replace  $n_{bg}$  by  $n_b$  and take  $\alpha'_R \cong 0$ , we recover the results that may be found in many previous works when absorption is assumed to be negligible [49]. The last term in Eq. (2.55) is the absorptive contribution to equation (7) of a paper by Chaumet and Nieto-Vesperinas [51] when the field is assumed to have the form of Eq. (2.47).

The polarizability in the case of a dielectric sphere of radius  $a$  much smaller than the wavelength of the field is given by

$$\alpha(\omega) = 4\pi\epsilon_b \left( \frac{\epsilon_s - \epsilon_b}{\epsilon_s + 2\epsilon_b} \right) a^3. \quad (2.56)$$

Dispersion affects the force, of the form of Eq. (2.55), through both the group index ( $n_{bg}$ ) of the host dielectric medium and the variation of the real part of the sphere's polarizability with frequency ( $\alpha'_R$ ). The latter depends on both the intrinsic frequency dependence of the permittivity of the material of the sphere and the frequency dependence of the refractive index of the host medium. If these dispersive contributions to the force exceed the remaining two contributions to the force of Eq. (2.56), the total force becomes

$$F \cong \frac{1}{4c} [-\alpha_R n_{bg} + n_b \omega \alpha'_R] \frac{\partial}{\partial \tau} |\mathcal{E}|^2. \quad (2.57)$$

Using Eq. (2.56) for this case, we obtain

$$F \cong -\frac{3\pi\epsilon_0 a^3}{c} n_{bg} \frac{n_s^2 n_b^4}{(n_s^2 + 2n_b^2)^2} \frac{\partial}{\partial \tau} |\mathcal{E}|^2 \quad (2.58)$$

if the dispersion of the dielectric material constituting the sphere is much smaller than that of the host dielectric medium, i.e., if  $d\epsilon_s/d\omega \ll d\epsilon_b/d\omega$ . (Here  $n_s$  is the refractive index at frequency  $\omega$  of the material of the sphere.) This result implies that, in the case of a slow-light host medium ( $n_{bg} \gg 1$ ), the force on the sphere can be much larger than would be the case in a “normally dispersive” medium, and is in the direction opposite to that in which the field propagates.

The simple formula of Eq. (2.58), and similar expressions obtained in other limiting cases of Eq. (2.55), obviously allow for a wide range of forces when a pulse of radiation is incident on a dielectric sphere in a host dielectric medium. Here we make only a few remarks concerning the last term in Eq. (2.55). Although we have associated this contribution to the force with absorption, such a force appears even if the sphere does not absorb any radiation of frequency  $\omega$ . This is because there must be an imaginary part of the polarizability simply because the sphere scatters radiation and thereby takes energy out of the incident field. According to the optical theorem in this case of scattering by a non-absorbing polarizable particle that is small compared

to the wavelength of the field, the imaginary part of the polarizability is related to the complete (complex) polarizability as follows [52]:

$$\alpha_I(\omega) = \frac{1}{4\pi\epsilon_0} \frac{2\omega^3}{3c^3} n_b |\alpha(\omega)|^2. \quad (2.59)$$

Then the force proportional to  $\alpha_I(\omega)$  in Eq. (2.55) is

$$F_{\text{scat}} \equiv \frac{1}{2} n_b^5 \frac{\omega}{c} \alpha_I |\mathcal{E}|^2 = \frac{8\pi}{3} \left(\frac{\omega}{c}\right)^4 \frac{n_b^5 I}{c} \left(\frac{\epsilon_s - \epsilon_b}{\epsilon_s + 2\epsilon_b}\right)^2 a^6, \quad (2.60)$$

which is just the well known “scattering force” [53] on a dielectric sphere in a medium with refractive index  $n_b$ , which may be taken to be real in the approximation in which the field is far from any absorption resonances of the sphere.

## 2.7 Conclusions

In this Chapter, we have attempted to better understand the different electromagnetic momenta and the forces on electrically polarizable particles in dispersive dielectric media. We have made several simplifications, including the neglect of any surface effects, the treatment of the medium as a non-deformable body, and the approximation of plane-wave fields. We have shown that conservation of momentum, even in seemingly simple examples such as the Doppler effect, generally requires consideration not only of the Abraham momentum and the Abraham force, but also of a contribution to the momentum of the medium due specifically to the dispersive nature of the medium. We have generalized some well known expressions for the forces on particles immersed in a dielectric medium to include the dispersion effect. While we have presented arguments in favor of the interpretation of the Abraham momentum as the momentum of the field, our simplified analyses lead to the conclusion that neither the Abraham nor the Minkowski expressions for photon momentum give the recoil momentum of a particle in a dispersive dielectric medium. Finally we have shown that the force

exerted on a particle in a strongly dispersive medium is approximately proportional to the group index  $n_{bg}$ , and can therefore become very large in a slow-light medium.

## 2.8 Appendix: energy density in dispersive media

To derive the expression of the energy density of an electromagnetic field in a dispersive dielectric medium, we start from the macroscopic Maxwell Equation and has

$$\frac{\partial u}{\partial t} = \mathbf{E} \cdot \frac{\partial \mathbf{D}}{\partial t} + \mathbf{H} \cdot \frac{\partial \mathbf{B}}{\partial t}. \quad (2.61)$$

The time-dependent electric field can be expressed using the slowly-varying envelope approximation as follows:

$$\begin{aligned} \mathbf{E}(t) &= \mathbf{A}(t)e^{-i\omega_0 t} \\ &= \int_{-\infty}^{\infty} d\delta \tilde{\mathbf{A}}(\delta) e^{-i(\omega_0 + \delta)t}, \end{aligned} \quad (2.62)$$

where  $\tilde{\mathbf{A}}(\delta)$  is the spectrum of the field with respect to the center frequency  $\omega_0$ . Consequently, one has

$$\begin{aligned} \mathbf{D}(\mathbf{t}) &= \epsilon_0 \int_{-\infty}^t dt' \epsilon_r(t-t') \mathbf{E}(t') \\ &= \epsilon_0 \int_{-\infty}^{\infty} d\delta \epsilon_r(\omega_0 + \delta) \tilde{\mathbf{A}}(\delta) e^{-i(\omega_0 + \delta)t} \\ &= \epsilon_0 \int_{-\infty}^{\infty} d\delta \left[ \epsilon_r(\omega_0) + \delta \frac{d\epsilon_r}{d\omega} \right] \tilde{\mathbf{A}}(\delta) e^{-i(\omega_0 + \delta)t} \\ &= \epsilon_0 \left[ \epsilon_r(\omega_0) \mathbf{E}(t) + i \frac{d\epsilon_r}{d\omega} e^{-i\omega_0 t} \frac{\partial \mathbf{A}}{\partial t} \right]. \end{aligned} \quad (2.63)$$

Using the above expressions, one has

$$\begin{aligned}
\frac{\partial \mathbf{D}}{\partial t} &= \epsilon_0 \left[ \epsilon_r(\omega_0) \frac{\partial \mathbf{E}}{\partial t} + \omega_0 \frac{d\epsilon_r}{d\omega} e^{-i\omega_0 t} \frac{\partial \mathbf{A}}{\partial t} \right] \\
&= \epsilon_0 \epsilon_r(\omega_0) \frac{\partial \mathbf{A}}{\partial t} e^{-i\omega_0 t} - i\epsilon_0 \omega_0 \epsilon_r(\omega_0) \mathbf{A} e^{-i\omega_0 t} \\
&\quad + \epsilon_0 \left[ \omega_0 \frac{d\epsilon_r}{d\omega} e^{-i\omega_0 t} \frac{\partial \mathbf{A}}{\partial t} \right] \\
&= \epsilon_0 \left( \epsilon_r(\omega_0) + \omega_0 \frac{d\epsilon_r}{d\omega} \right) \frac{\partial \mathbf{A}}{\partial t} e^{-i\omega_0 t} \\
&\quad - i\epsilon_0 \omega_0 \epsilon_r(\omega_0) \mathbf{E}.
\end{aligned} \tag{2.64}$$

And consequently one has

$$\begin{aligned}
\mathbf{E} \cdot \frac{\partial \mathbf{D}}{\partial t} &= \epsilon_0 \left( \epsilon_r(\omega_0) + \omega_0 \frac{d\epsilon_r}{d\omega} \right) \mathbf{E} \frac{\partial \mathbf{A}}{\partial t} e^{-i\omega_0 t} \\
&\quad - i\epsilon_0 \omega_0 \epsilon_r(\omega_0) \mathbf{E}^2.
\end{aligned} \tag{2.65}$$

Thus, the time average energy density is given by

$$\begin{aligned}
u &= \frac{1}{2} \epsilon_0 \mathbf{E}_\omega^2 \left[ \epsilon_r + \frac{1}{2} \omega \frac{d\epsilon_r}{d\omega} \right] \\
&= \frac{1}{2} \epsilon_0 \mathbf{E}_\omega^2 [n^2 + n(n_g - n)] \\
&= \frac{1}{2} \epsilon_0 n n_g \mathbf{E}_\omega^2.
\end{aligned} \tag{2.66}$$

# Chapter 3

## Noise Properties of Slow-Light Media

### 3.1 Background

Optical amplification, by means of erbium doped fiber amplifiers [54, 55], semiconductor optical amplifiers [56], Raman amplifiers [57], parametric amplifiers, surface plasmon amplifiers [58], etc., have been analyzed and employed in a wide spectrum of applications including telecommunications, optical information processing, quantum optics, etc. In many cases, optical amplifiers can also work as attenuators given appropriate working conditions. Recently, optical amplification and attenuation have also attracted much attention for the purpose of slow and fast light propagation [4, 59, 1, 60, 61]. The most extreme values of the group index often occur when the signal wavelength is at or near a strong gain or absorption resonance of a material system. In this chapter, we address the following question: How much noise, if any, is added to a beam of light as it propagates through a medium with an extreme value of the group velocity?

In many cases of interest the quantum-mechanical properties of the electromagnetic field pose a fundamental limit to the noise level of optical beams. An ideal

phase-insensitive optical amplifier has been treated with a quantum beam-splitter model with two input ports, a signal field and a vacuum field [62]. In such a model, the amplifier noise can be attributed mainly to the beating between the amplified signal field and the amplified vacuum fluctuations.

A non-ideal amplifier or attenuator typically puts extra noise into the output signal, and the properties of such a non-ideal amplifier or attenuator have been traditionally described by alternating pairs of ideal amplifiers and attenuators, a three-dimensional quantum beam-splitter model [63], etc. Such treatments require a certain ordering of the cascaded ideal amplifiers and attenuators, and some of the analytical expressions lack simplicity or intuition.

Here we present a modified quantum beam-splitter model to describe a non-ideal linear amplifier or attenuator, beginning with a brief summary of the usual treatments in Sections 3.2 and 3.3. Our model is introduced in Section 3.4 and applied specifically to several types of practical amplifiers. The noise properties of a slow-light element based on different types of realistic amplifiers/attenuators are then discussed in Section 3.5, followed by a summary in Section 3.6.

## 3.2 A quantum model of an ideal linear amplifier

We first summarize the quantum description of the noise properties of an ideal quantum amplifier [62] for the case of a single-mode input field propagating through an ideal linear amplifier with intensity gain  $G_0$ . The photon annihilation operators for the input and output fields are denoted by  $\hat{a}$  and  $\hat{b}$ , respectively. Since photons are Bosons, we have the following commutation relations:

$$[\hat{a}, \hat{a}^\dagger] = [\hat{b}, \hat{b}^\dagger] = 1. \quad (3.1)$$

The annihilation operator for the output field is expressed in terms of the annihi-

lation operator for the input field and a Langevin operator  $\hat{L}$  as follows [62]:

$$\hat{b} = g_0 \hat{a} + \hat{L}^\dagger, \quad (3.2)$$

where  $g_0 = \sqrt{G_0}$ , and  $\hat{L} = (G_0 - 1)^{1/2} \hat{c}$ , and where  $\hat{c}$  denotes a second input field and satisfies the relation  $[\hat{c}, \hat{c}^\dagger] = 1$ . The Langevin operator is assumed to be uncorrelated from the input operator, i.e.,

$$[\hat{a}, \hat{L}^\dagger] = [\hat{a}, \hat{L}] = 0, \quad (3.3)$$

in which case it follows from Eq. (3.2) that  $[\hat{b}, \hat{b}^\dagger] = 1$ . For an ideal amplifier, one generally assumes that the second input field  $\hat{c}$  represents a vacuum state, i.e.,

$$\langle \hat{n}_c \rangle = \langle \hat{c}^\dagger \hat{c} \rangle = 0. \quad (3.4)$$

Then the expectation value of the photon number of the output field is

$$\langle \hat{n}_b \rangle = \langle \hat{b}^\dagger \hat{b} \rangle = G_0 \langle \hat{n}_a \rangle + (G_0 - 1), \quad (3.5)$$

where  $\langle \hat{n}_a \rangle = \langle \hat{a}^\dagger \hat{a} \rangle$  is the average photon number of the input field. One sees that, in addition to the input field being amplified by a factor of  $G_0$ ,  $(G_0 - 1)$  noise photons are added to the output field.

From these expressions one obtains the variance of the output photon number:

$$\begin{aligned} \langle \Delta \hat{n}_b^2 \rangle &\equiv \langle \hat{n}_b^2 \rangle - \langle \hat{n}_b \rangle^2 \\ &= G_0^2 \langle \Delta \hat{n}_a^2 \rangle + G_0(G_0 - 1)(\langle \hat{n}_a \rangle + 1). \end{aligned} \quad (3.6)$$

The first term represents the amplification of the fluctuations present in the input field, and the second term represents added noise.

The noise properties of an amplifier are often characterized by the noise figure,

defined as

$$\mathcal{F} \equiv \frac{\text{SNR}_{\text{in}}}{\text{SNR}_{\text{out}}}, \quad (3.7)$$

where

$$\text{SNR}_{\text{in}} \equiv \frac{\langle \hat{n}_a \rangle^2}{\langle \Delta \hat{n}_a^2 \rangle}, \quad (3.8)$$

$$\text{SNR}_{\text{out}} \equiv \frac{G_0^2 \langle \hat{n}_a \rangle^2}{\langle \Delta \hat{n}_b^2 \rangle}. \quad (3.9)$$

Note that in  $\text{SNR}_{\text{out}}$  we use  $G_0 \langle \hat{n}_a \rangle$  for the amplified signal field, not the total output field that includes the noise contributions. For an ideal quantum amplifier, the noise figure is then found from the expressions above to be

$$\mathcal{F} = 1 + \left(1 - \frac{1}{G_0}\right) \frac{\langle \hat{n}_a \rangle + 1}{\langle \Delta \hat{n}_a^2 \rangle}. \quad (3.10)$$

When the fluctuations of the input field follow Poisson statistics, so that  $\langle \Delta \hat{n}_a^2 \rangle = \langle \hat{n}_a \rangle$ , one sees that the value of the noise figure  $\mathcal{F}$  of an ideal quantum amplifier approaches 2 (or 3dB) when  $G_0, \langle \hat{n}_a \rangle \gg 1$ [64].

### 3.3 A quantum model of an ideal linear attenuator

We now consider the case of a single-mode input field propagating through an ideal attenuator with intensity transmission  $T_0$ , which is often modeled as a quantum beam splitter. In order to preserve the commutation relations for the output field, the annihilation operator for the output field is similarly expressed in terms of the annihilation operator for the input field  $\hat{a}$  and a Langevin operator  $\hat{L}$  as follows:

$$\hat{b} = t_0 \hat{a} + \hat{L}, \quad (3.11)$$

where  $t_0 = \sqrt{T_0}$ ,  $\hat{L} = (1 - T_0)^{1/2}\hat{c}$ , and  $[\hat{c}, \hat{c}^\dagger] = 1$ . The Langevin operator is again assumed to be uncorrelated from the input operator:

$$[\hat{a}, \hat{L}^\dagger] = [\hat{a}, \hat{L}] = 0. \quad (3.12)$$

For an ideal attenuator, one typically assumes again that  $\hat{c}$  denotes a vacuum-state input, i.e.,

$$\langle \hat{n}_c \rangle = \langle \hat{c}^\dagger \hat{c} \rangle = 0. \quad (3.13)$$

The expected photon number of the output field of such an ideal attenuator is then

$$\langle \hat{n}_b \rangle = \langle \hat{b}^\dagger \hat{b} \rangle = T_0 \langle \hat{n}_a \rangle, \quad (3.14)$$

where  $\langle \hat{n}_a \rangle = \langle \hat{a}^\dagger \hat{a} \rangle$  is again the average photon number of the input field. Note that this result agrees with that obtained by a classical treatment.

The intensity fluctuation of the output field is given by

$$\begin{aligned} \langle \Delta \hat{n}_b^2 \rangle &\equiv \langle \hat{n}_b^2 \rangle - \langle \hat{n}_b \rangle^2 \\ &= T_0^2 \langle \Delta \hat{n}_a^2 \rangle + T_0(1 - T_0) \langle \hat{n}_a \rangle. \end{aligned} \quad (3.15)$$

The first term represents the attenuation of the fluctuations present in the input beam, and the second term represents noise added due to the random loss of photons from the signal field.

The noise figure of the ideal attenuator is then found to be

$$\mathcal{F} = 1 + \left( \frac{1}{T_0} - 1 \right) \frac{\langle \hat{n}_a \rangle}{\langle \Delta \hat{n}_a^2 \rangle}. \quad (3.16)$$

This noise figure can become arbitrarily large as the transmission of the attenuator

approaches zero. This increased noise can be attributed to the random loss of photons from the signal field.

### 3.4 A generalized model for a non-ideal linear amplifier or attenuator

We next propose a new quantum approach to model a non-ideal amplifier or attenuator. For the case of an amplifier, we use a single quantum amplifying beam-splitter model with intensity gain  $G$  for the signal. In contrast to the ideal amplifier model described in Section 3.2, we assume that the second input field  $\hat{c}$  for the amplifying beam splitter is not a vacuum field, but a completely incoherent noise field with average photon number  $\langle \hat{n}_c \rangle$ . As in Section 3.2, the output field operator is related to the input field operator by

$$\hat{b} = g\hat{a} + \hat{L}^\dagger, \quad (3.17)$$

where  $g = \sqrt{G}$  is the amplitude gain coefficient, and  $\hat{L} = (G - 1)^{1/2}\hat{c}$  is the Langevin operator corresponding to the amplified noise source. In this more general case, however, the average photon number of the output field  $\hat{b}$  is given by

$$\langle \hat{n}_b \rangle = G\langle \hat{n}_a \rangle + (G - 1)(\langle \hat{n}_c \rangle + 1), \quad (3.18)$$

and its variance by

$$\begin{aligned} \langle \Delta \hat{n}_b^2 \rangle &= G^2 \langle \Delta \hat{n}_a^2 \rangle + (G - 1)^2 \langle \Delta \hat{n}_c^2 \rangle \\ &\quad + G(G - 1)[\langle \hat{n}_a \rangle \langle \hat{n}_c \rangle + (\langle \hat{n}_a \rangle + 1)(\langle \hat{n}_c \rangle + 1)] \\ &= G^2 \langle \Delta \hat{n}_a^2 \rangle + G(G - 1)\langle \hat{n}_a \rangle(2\langle \hat{n}_c \rangle + 1) \\ &\quad + (G - 1)(\langle \hat{n}_c \rangle + 1) + (G - 1)^2(\langle \hat{n}_c \rangle + 1)^2. \end{aligned} \quad (3.19)$$

Consistent with our assumption of incoherent noise, the variance of the noise field is assumed to obey Bose-Einstein statistics, and, in particular,  $\langle \Delta \hat{n}_c^2 \rangle = \langle \hat{n}_c \rangle + \langle \hat{n}_c \rangle^2$  [56].

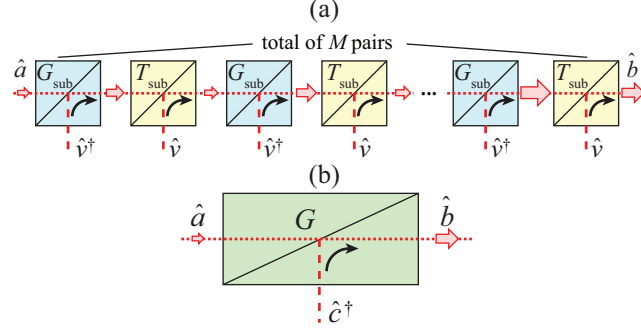


Figure 3.1: One can describe a realistic amplifier using (a) a series of alternating ideal amplifiers and attenuators, or (b) a general quantum beam splitter model.

For a non-ideal attenuator, similarly, we use the quantum beam-splitter model with a noise input  $\hat{c}$  assumed to be a (non-vacuum) incoherent field with its fluctuations obeying Bose-Einstein statistics. In this case, the annihilation operator for the output field is

$$\hat{b} = T^{1/2}\hat{a} + (1 - T)^{1/2}\hat{c}, \quad (3.20)$$

where  $T$  is the intensity transmission of the attenuator. The expectation value of the photon number of the output field is then

$$\langle \hat{n}_b \rangle = T\langle \hat{n}_a \rangle + (1 - T)\langle \hat{n}_c \rangle, \quad (3.21)$$

and the variance is

$$\begin{aligned} \langle \Delta \hat{n}_b^2 \rangle &= T^2\langle \Delta \hat{n}_a^2 \rangle + (1 - T)^2\langle \Delta \hat{n}_c^2 \rangle \\ &\quad + T(1 - T)(\langle \hat{n}_a \rangle + 1)\langle \hat{n}_c \rangle \\ &\quad + T(1 - T)(\langle \hat{n}_c \rangle + 1)\langle \hat{n}_a \rangle. \end{aligned} \quad (3.22)$$

We will show in the following that by an appropriate choice for  $\langle \hat{n}_c \rangle$ , this model can describe various types of realistic amplifiers and attenuators.

### 3.4.1 A not-entirely-inverted laser amplifier

Many practical amplifiers have both amplification and attenuation mechanisms distributed throughout the device. One such example is a not-entirely-inverted laser medium in which excited-state population density  $N_2$  provides gain, while ground-state population density  $N_1$  provides loss. The net gain coefficient per unit length  $g$  is proportional to  $N_2 - N_1$ . Assuming a uniform gain coefficient through out the amplifier, the signal gain is  $G = \exp(gL)$  where  $L$  is the total length of the amplifier.

One way to model quantum mechanically such a one-dimensional not-entirely-inverted laser amplifier is to use a series of alternating ideal sub-amplifiers and sub-attenuators [see Fig. 3.1(a)], with the gain/loss of each ideal sub-amplifier/attenuator given by

$$\begin{aligned} G_{\text{sub}} &\approx 1 + \frac{N_2}{N_2 - N_1} \frac{gL}{M}, \\ &= 1 + n_{\text{sp}} \frac{gL}{M} \end{aligned} \quad (3.23)$$

$$\begin{aligned} T_{\text{sub}} &\approx 1 - \frac{N_1}{N_2 - N_1} \frac{gL}{M}, \\ &= 1 + (1 - n_{\text{sp}}) \frac{gL}{M} \end{aligned} \quad (3.24)$$

where  $M$  is the number of sub-amplifier-attenuator pairs, and

$$n_{\text{sp}} = \frac{N_2}{N_2 - N_1}, \quad (3.25)$$

is known as the spontaneous emission factor [65], or inversion factor [66]. A large number of sub-amplifier/attenuator pairs are needed for an amplifier with a weak input field, a large gain  $G$ , or a large spontaneous emission factor  $n_{\text{sp}}$ .

Alternatively, one can use our single-step modified quantum amplifier model to describe such a not-entirely-inverted laser amplifier. Specifically, when one chooses  $\langle \hat{n}_c \rangle = n_{\text{sp}} - 1$ , (3.18) and (3.19) become

$$\langle \hat{n}_b \rangle = G \langle \hat{n}_a \rangle + (G - 1)n_{\text{sp}}, \quad (3.26)$$

and

$$\begin{aligned} \langle \Delta \hat{n}_b^2 \rangle &= G^2 \langle \Delta \hat{n}_a^2 \rangle + G(G - 1) \langle \hat{n}_a \rangle (2n_{\text{sp}} - 1) \\ &\quad + (G - 1)n_{\text{sp}} + (G - 1)^2 n_{\text{sp}}^2. \end{aligned} \quad (3.27)$$

In the limiting case when  $n_{\text{sp}} = 1$ , corresponding to complete population inversion, the noise input field  $\langle \hat{n}_c \rangle = 0$  is the vacuum field, and (3.26) and (3.27) reduce to the results of an ideal amplifier, Eqs. (3.5) and (3.6).

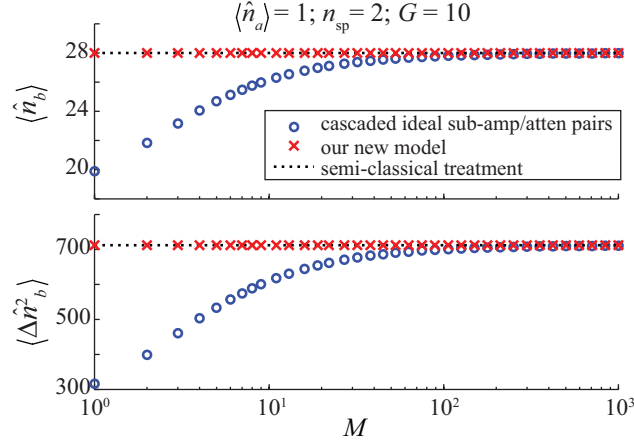


Figure 3.2: The average photon number and its variance for the output field of a not-entirely-inverted amplifier using two different models.  $M$  is the number of divided ideal sub-amplifier/attenuator pairs. The average photon number of the input field is  $\langle \hat{n}_a \rangle = 1$ , the total gain of the amplifier is  $G = 10$ , and the spontaneous emission factor is  $n_{\text{sp}} = 2$ .

The motivation for the choice  $\langle \hat{n}_c \rangle = n_{\text{sp}} - 1$  can be understood from a simple semiclassical model in which the noise arises from spontaneous emission of photons

into the propagating field. The intensity  $I$  in this model propagates according to the equation

$$\frac{dI}{dz} = gI + R_{\text{spont}}h\nu N_2, \quad (3.28)$$

where  $R_{\text{spont}}$  is the spontaneous emission rate into the single mode of frequency  $\nu$ , and  $I$  is the intensity. For the model here in which the gain and population densities are uniform within a volume  $V$ ,  $g = (V/c)R_{\text{spont}}(N_2 - N_1)$ , and it follows that the photon number  $q$  at  $z = L$  is

$$q(L) = Gq(0) + (G - 1)n_{\text{sp}}, \quad (3.29)$$

exactly as in Eq. (3.26).

As a numerical example, we calculate the average photon number and the variance of the output of a not-entirely-inverted laser amplifier modeled by the two approaches just described. In this example the average photon number of the input field is  $\langle \hat{n}_a \rangle = 1$ , the total gain of the amplifier is  $G = 10$ , and the spontaneous emission factor is  $n_{\text{sp}} = 2$ . The blue circles represent the results obtained using  $M$  pairs of ideal sub-amplifier/attenuator as the value of  $M$  increases. One sees that the calculated results using cascaded ideal sub-amplifier/attenuator pairs converges to the correct values [67, 63] after the number of pairs  $M$  is greater than 100. On the other hand, our approach gives the same correct answer using just a single step. For comparison purposes, we have also calculated the output of  $M$  cascaded generalized quantum beam splitters, each with the same value of  $n_{\text{sp}}$  and gain  $G_{\text{sub}} = G^{1/M}$ . In fact, it can be shown using our model that the output of two cascaded amplifiers with the same value of  $n_{\text{sp}}$  but with different gains  $G_1$  and  $G_2$  is identical to that of a single amplifier with  $n_{\text{sp}}$  and intensity gain  $G = G_1G_2$ . This can also be seen in Fig. 3.2 that the results obtained using our proposed treatment, indicated by the red crosses, does not change as  $M$  increases. Our model, in contrast to the model based

on alternating sub-amplifier/attenuator pairs, requires only a single calculation step, which is computationally efficient.

In this case of an attenuator ( $N_1 > N_2$ ), one can use our modified quantum beam splitter model, i.e., Eqs. (3.21) and (3.22), with  $\langle \hat{n}_c \rangle = -n_{\text{sp}}$  and intensity attenuation  $T = e^{gL}$ ; of course  $g$  is negative for an attenuator. The average value and the variance of the output photon number are

$$\langle \hat{n}_b \rangle = T \langle \hat{n}_a \rangle + n_{\text{sp}}(T - 1), \quad (3.30)$$

and

$$\begin{aligned} \langle \Delta \hat{n}_b^2 \rangle &= T^2 \langle \Delta \hat{n}_a^2 \rangle + T(T - 1) \langle \hat{n}_a \rangle (2n_{\text{sp}} - 1) \\ &\quad + (T - 1)n_{\text{sp}} + (1 - T)^2 n_{\text{sp}}^2. \end{aligned} \quad (3.31)$$

Note that all four terms in the expression of Eq. (3.31) are positive, as  $n_{\text{sp}}$  is a negative number when  $T < 1$ . Again, in the limiting case for which  $n_{\text{sp}} = 0$ , indicating that all the population is in the ground state, the noise field  $\langle \hat{n}_c \rangle = 0$  becomes the vacuum field, and the results (3.30) and (3.31) reduce to those for an ideal attenuator, Eqs. (3.14) and (3.15).

Note also that the results given by Eqs. (3.30) and (3.31) are actually of the same form as those of Eqs. (3.26) and (3.27). This indicates that, although we start from two different mathematical descriptions for amplifiers and attenuators, we have obtained a consistent description for a non-ideal laser medium which acts as either an amplifier or an attenuator.

The noise figure of such a not-entirely-inverted laser medium is therefore

$$\begin{aligned} \mathcal{F} &= 1 + \frac{G - 1}{G} \frac{\langle \hat{n}_a \rangle}{\langle \Delta \hat{n}_a^2 \rangle} (2n_{\text{sp}} - 1) \\ &\quad + \frac{G - 1}{G^2} \frac{n_{\text{sp}}}{\langle \Delta \hat{n}_a^2 \rangle} + \frac{(G - 1)^2}{G^2} \frac{n_{\text{sp}}^2}{\langle \Delta \hat{n}_a^2 \rangle}. \end{aligned} \quad (3.32)$$

$G$  can of course have any positive value, while  $n_{\text{sp}}$  is greater than one for  $G > 1$  and is negative for  $G < 1$ .

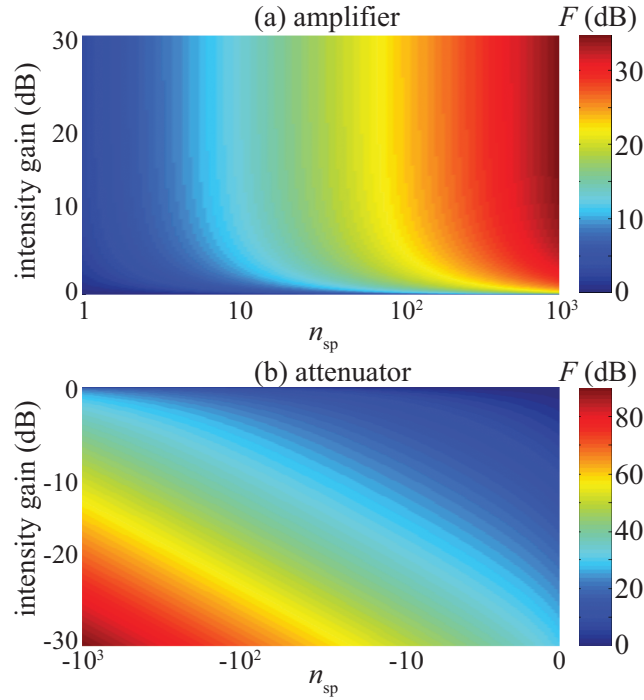


Figure 3.3: Noise figure of a laser medium as a function of intensity gain  $G$  and spontaneous emission factor  $n_{\text{sp}}$  when it operates as (a) an amplifier and (b) an attenuator. Here, the average photon number of the input field is 1000.

The noise figure  $\mathcal{F}$  of a laser medium as a function of intensity gain  $G$  and spontaneous emission factor  $n_{\text{sp}}$  when it operates as either an amplifier or an attenuator is shown in Fig. 3.3. The average photon number of the input field used in the calculation is  $\langle \hat{n}_a \rangle = 1000$ , and we assume its fluctuations obey Poisson statistics. For a given value of  $n_{\text{sp}}$ , the noise figure of a laser amplifier increases as the gain becomes larger, but it also saturates to  $2n_{\text{sp}}$  when the input signal is strong compared to  $n_{\text{sp}}$ . On the other hand, the noise figure for an attenuator increases without bound as the transmission decreases. Furthermore, besides the linear term  $(2n_{\text{sp}} - 1)/T$ , there is a second-order term proportional to  $n_{\text{sp}}^2/T^2$ . Thus, the noise figure can be more than 80 dB for an attenuator with  $T = 10^{-3}$  and  $n_{\text{sp}} = 10^3$ .

### 3.4.2 A stimulated Brillouin scattering amplifier

Stimulated Brillouin scattering (SBS) is a common nonlinear process in fiber optics. The interaction occurs through the modulation of the refractive index of the medium induced by the acoustic phonons through electrostriction. A strong pump field can create a gain resonance with a center frequency downshifted by the Stokes frequency  $\nu_B$  for signals counter-propagating through the fiber. While the signal is amplified, noise can also be introduced by the amplified spontaneous Brillouin scattering field. SBS-based slow light is one of the most common and convenient techniques to build fiber-based delay elements for current telecommunication systems [12, 13].

The excess noise of an SBS amplifier mainly comes from the amplified spontaneous Brillouin scattering [68, 69]. When the propagation loss of the fiber is negligible and the pump field is undepleted, the noise property of such an SBS amplifier can be described by choosing the value of  $\langle \hat{n}_c \rangle$  at temperature  $T$  to be

$$\langle \hat{n}_c \rangle = \frac{1}{e^{h\nu_B/kT} - 1}, \quad (3.33)$$

$\langle \hat{n}_c \rangle$  in this case is directly related to the number of thermally excited phonons per mode.

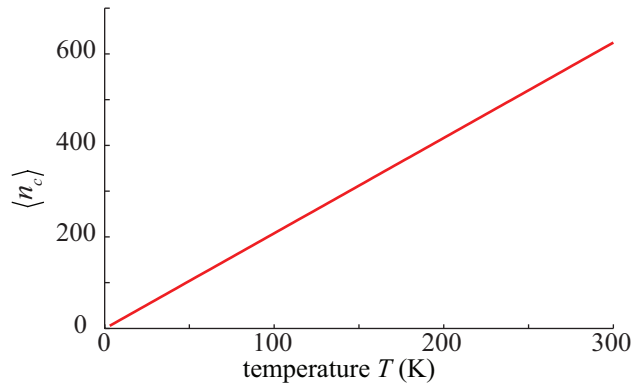


Figure 3.4: The expectation value of photon number in the noise input source  $\langle \hat{n}_c \rangle$  of a SBS medium as a function of temperature  $T$ .

Figure 3.4 shows the expectation value of the photon number of the noise input

source  $\langle \hat{n}_c \rangle$  as a function of temperature. Here the phonon frequency is assumed to be 10 GHz. At room temperature ( $T = 300$  K), the value of  $\langle \hat{n}_c \rangle$  is approximately 625, indicating that the noise figure of an SBS amplifier is much larger than that of a laser amplifier.

### 3.5 Noise figure of a gain-induced slow-light medium

There is much current interest in exploring the physics and applications involving the control of the group velocity of light. The Kramers-Kronig relations allow for slow light to be realized near the vicinity of a gain resonance, and tunable delays can be achieved by controlling the magnitude of the gain.

In many cases, the gain profile of a slow-light medium is of Lorentzian shape. In such way, the group index  $n_g$  and the gain coefficient  $g_0$  at the resonance center is related through the following expression:

$$n'_g = n_g - n = \frac{g_0 c}{2\gamma}, \quad (3.34)$$

where  $c$  is the speed of light in vacuum, and  $\gamma$  is the  $1/e$  half width of the Lorentzian gain profile. The relative group delay through the medium as compared to a reference is  $\tau_g = n'_g L/c$ , and the peak intensity gain through the same medium is  $G = \exp(g_0 L)$ , where  $L$  is the length of the medium. Thus, one has the following relation between the group delay and the peak intensity gain:

$$G = \exp(2\gamma\tau_g). \quad (3.35)$$

In writing this result in this form, we have implicitly assumed that the light pulse is spectrally sufficiently narrow that pulse distortion due to dispersion of the group velocity is small. In this case that the time delay is reliably estimated by means of the group velocity.

To maintain generality, we still analyze the noise figure  $\mathcal{F}$  of a slow-light medium in terms of gain  $G$ , and the relation between  $\mathcal{F}$  and the relative group delay  $\tau_g$  can be consequently obtained using the relation of Eq. (3.35).

For a laser medium, in which the total population in ground and excited states are assumed to be constant, changing the magnitude of the gain usually involves changing the population inversion. Assume the maximum intensity gain is  $G_{\max}$  when all the population is inverted, i.e.,  $n_{\text{sp}} = 1$ . For any given intensity gain  $G < G_{\max}$ , the value of  $n_{\text{sp}}$  is given by

$$n_{\text{sp}} = \frac{1}{2} \left( \frac{\ln(G_{\max})}{\ln(G)} + 1 \right). \quad (3.36)$$

Note that  $n_{\text{sp}}$ , but not the noise figure, can be divergent near a transmission of unity. At unity transmission, the value of  $\mathcal{F}$  can be obtained as follows:

$$\mathcal{F}(T = 1) = 1 + \ln(G_{\max}). \quad (3.37)$$

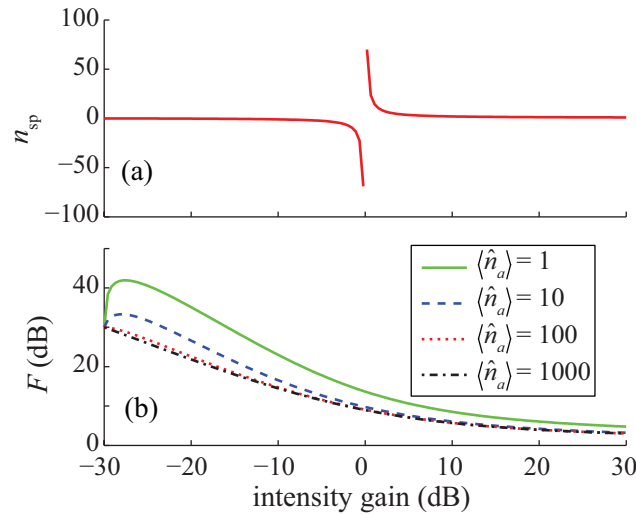


Figure 3.5: (a) The spontaneous emission factor  $n_{\text{sp}}$  and (b) noise figure  $\mathcal{F}$  of a laser medium as functions of the intensity gain for input fields with different values of average photon number.

As a numerical example of such a laser medium with  $G_{\max} = 30$  dB, we show in

Fig. 3.5 the values of  $n_{\text{sp}}$  and  $\mathcal{F}$  as functions of the gain of the medium. As expected, the magnitude of  $n_{\text{sp}}$  diverges when the transmission is close to unity. However, the value of the noise figure is always finite, and it increases as  $G$  becomes smaller. For weak input field, the noise figure actually reaches a peak value before the minimum transmission point. Working at the center of a gain or absorption resonance indicates slow or fast light, respectively. Therefore, when a laser medium is used as a tunable slow-light element, the noise is least when maximum delay is achieved, and increases generally as the delay becomes smaller.

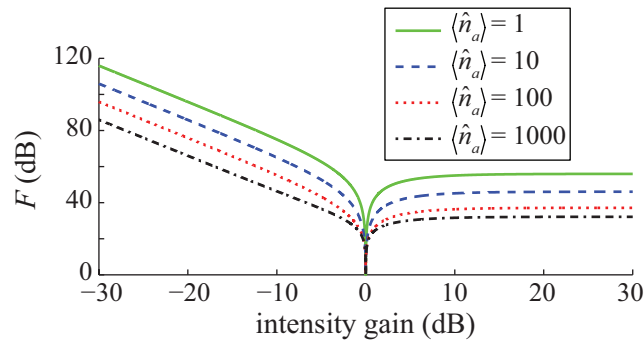


Figure 3.6: The noise figure  $\mathcal{F}$  of an SBS medium as a function of the intensity gain for input fields with different values of average photon number.

For an SBS slow-light medium, tunable delay is achieved by controlling the power of the pump field. Assuming the pump field is undepleted, the intensity gain  $G$  is independent of the properties of the noise source, which is determined by the acoustic phonons in the fiber. Thus, the noise figure of an SBS slow-light element is minimum at zero delay, and it increases monotonically as the gain and delay increases.

At the anti-Stokes resonance of the pump field, the signal field experiences loss, and the SBS medium becomes a fast-light medium. When it works as an attenuator, we can ignore the noise contribution from the spontaneous emission from the Stokes resonance by assuming the frequency component near the Stokes resonance is filtered out by, e.g., narrow-band filters. The noise figures are plotted in Fig. 3.6. As one sees from the figure, when such a SBS medium is used as a tunable slow-light element the

---

output field has least noise when there is no delay, and the noise increases as either delay or advancement increases.

## 3.6 Summary

In this chapter, we have presented a general quantum beam-splitter model for a realistic amplifier or attenuator. The model has two inputs, the signal field and a noise field. By choosing appropriately the input noise field, our model can describe various types of realistic amplifiers and attenuators. Using our model, we analyzed the noise performance of slow-light elements based on different types of amplifiers. For laser amplifiers, the smallest noise figure is obtained at largest gain or delay, while a SBS based delay element has the smallest noise figure at zero delay.

# Chapter 4

## Increasing the Fractional Delay of a Slow-Light Delay Element Using Multiple Gain Lines

### 4.1 Fractional delay and practical considerations

While the magnitude of the group index of a medium is an important figure of merit for exploring the fundamentals of slow light, a more practical figure of merit for delay-line applications is how much time delay a slow-light element can provide as compared to the temporal duration of a signal pulse or of one data bit.

This thought can be quantified using the maximum fractional delay [70] (also known as the delay-bandwidth product [71]). One definition for the maximum fractional delay  $\overline{\Delta T}_{\max}$  is given by

$$\overline{\Delta T}_{\max} \equiv \frac{\Delta T_{\max}}{\Delta \tau} = 2\pi \Delta \nu \Delta T_{\max}, \quad (4.1)$$

where  $\Delta T_{\max}$  is the maximum achievable absolute delay,  $\Delta \tau = 1/(2\pi \Delta \nu)$  is the temporal duration of the pulse, and  $\Delta \nu$  is the signal bandwidth.

In practice, a practical slow-light medium typically has frequency dependent gain and group index. As analyzed in Section 1.3, these frequency dependences will lead to pulse distortion and/or power level change [72], which then deteriorate the quality of transmitted information.

To quantify the impact of pulse distortion and power level change, various criteria have been used based on different considerations.

One set of criteria is based on the physical origins of the various distortions. The first criterion is the gain distortion factor, defined as follows [35]:

$$D_g = \frac{G_{\max} - G_{\min}}{G_{\max} + G_{\min}}, \quad (4.2)$$

where  $G_{\max/\min} = \max/\min\{\exp(0.5g(\nu)L)\}$  is the maximum/minimal frequency-dependent amplitude gain within the bandwidth experienced in a medium with length  $L$ , and  $g(\nu)$  is the frequency dependent gain coefficient of the medium.

The second criterion is the phase distortion factor given by [35]

$$D_p = \max \left\{ (n(\nu) - n(\nu_0) - \nu n_{g,\text{eff}}) L / c_0 \right\}, \quad (4.3)$$

where  $n(\nu)$  is the frequency dependent refractive index,  $\nu_0$  is the center frequency and  $n_{g,\text{eff}}$  is the effective group index obtained from a linear fit of  $n(\nu)$  within the signal bandwidth.

It has been shown [35] that a suitable criterion is to require that both  $D_g$  and  $D_p$  be less than 0.05. Since a practical medium cannot provide arbitrarily large gain to the signal, an additional criterion is that the maximum frequency dependent amplitude gain within the bandwidth  $G_{\max}$  should be less than 3.5, corresponding to a maximum power gain of less than 30 dB.

While the above three criteria emphasize the physical origin of the distortion and provides a intuitive picture of whether a given gain profile is optimum or not, the magnitude of the two distortion factors are quite difficult to be measured. Thus,

there are also other distortion factors that is more measurable and can be tested, such as the change of the full width at half maximum (FWHM) of the temporal duration of the signal pulse.

Note that when individual pulse delay is studied, the group delay is usually defined in terms of the peak position of a single Gaussian pulse [35, 73, 74, 75, 76, 77, 78]. In a real telecommunication system, however, data packets are comprised of varying sequences of “0” and “1” bits in designated time slots, and the peak positions of individual pulses often experience a pattern-dependent delay [79] due to inter-symbol interference (ISI) [80], etc. Thus, a better and more practical way to determine the delay of a data packet through a slow-light medium is to define it in terms of the best-decision-time (BDT)  $t_{\text{opt}}$  in the eye-diagram when highest data fidelity [*i.e.*, lowest bit error rate (BER)] is achieved. Note that the eye diagram is also most open at  $t_{\text{opt}}$ ; this thought can be quantified using the eye-opening metric as follows:

$$\mathcal{E} \equiv \max \left\{ P_{1,\min}(t) - P_{0,\max}(t) \right\}, \quad (4.4)$$

where  $P_{1,\min}(t)/P_{0,\max}(t)$  is the lowest/highest normalized power among all “1”/“0” bits at time  $t$  within the time slot. Consequently, the BDT delay of a data packet can be determined by comparing the values of  $t_{\text{opt}}$  for propagation through the slow-light medium and through a reference medium.

In such cases, it makes more sense to quantify the distortion in terms of system metrics as well. The first criterion is that the maximum continuous wave (CW) exponential intensity gain within the bandwidth be less than a realistic value of 7 ( $\sim 30$  dB),

$$\max\{2k_0 \Im[\tilde{n}(\nu)] L\} < 7; \quad |\nu - \nu_0| < \Delta\nu, \quad (4.5)$$

where  $\Im[\ ]$  represents the imaginary part, and  $L$  is the length of the medium. The

second criterion is that the eye-opening penalty EOP [81] be less than 1.87 dB,

$$\text{EOP} \equiv -10 \log(\mathcal{E}_{\text{out}}/\mathcal{E}_{\text{in}}) < 1.87 \text{ dB}, \quad (4.6)$$

where  $\mathcal{E}_{\text{in/out}}$  is the eye-opening at input/output of the slow-light device. Note that, for a system that has a detector-limited signal-to-noise ratio (SNR) of 35 dB, an EOP of 1.87 dB indicates [81] that with an ideal input, the output BER is still less than  $10^{-12}$ . Note also that EOP is closely related [81] to the Q-factor penalty [79], and both merits can be cascaded through various elements to describe the overall system performance.

## 4.2 Optimization design using multiple gain lines

One practical way for realizing slow light [4] is to use the strong dispersion near a resonance gain feature of a medium. However, because both the gain coefficient and group index  $n_g$  vary significantly in the vicinity of a single resonance gain line,  $\overline{\Delta T}_{\text{max}}$  is often limited by pulse distortion [79, 82], especially when  $\Delta\nu$  becomes comparable to or larger than the spectral width of the gain feature.

It has recently been shown that the distortion in such a system can be decreased by using two closely spaced gain lines instead of a single gain line [35]. Here, the concept of using three closely spaced gain lines is introduced. Our laboratory implementation of the triple gain lines does not require more instrumentation than what is required to produce a double gain line, but the distortion can be reduced significantly. In this way, a larger  $\overline{\Delta T}_{\text{max}}$  can be achieved at a larger bandwidth.

The complex refractive index for a medium with multiple Lorentzian gain lines is given by

$$\tilde{n}(\nu) = 1 + \sum_j \frac{cg_j}{4\pi\nu_0} \frac{\gamma}{\nu - \nu_0 - \delta_j + i\gamma}, \quad (4.7)$$

where  $\nu_0$  is the center frequency of the entire gain feature;  $g_j$  and  $\delta_j$  are the peak gain coefficient and the shift of the resonance center from  $\nu_0$  of the  $j^{\text{th}}$  gain line, respectively;  $c$  is the speed of light in vacuum; and  $\gamma$  is the half-width at half-maximum linewidth of each gain line. To keep  $\tilde{n}(\nu)$  even-symmetric about  $\nu_0$ , we require that  $g_j = g_{-j}$  and  $\delta_j = -\delta_{-j}$ .

Note that, for a profile containing three closely spaced gain lines, when  $\delta_1 = \gamma$  and  $g_0/g_1 = 0.5$ , both the second and third order derivative of (5.2) become zero, indicating that both the group index and the gain coefficient have a flat top at  $\nu = 0$ . Thus, the distortion can be minimized over a large bandwidth range.

To be more general to meet specific sets of distortion metrics, we scan the values of the relative center frequency  $\delta_j$  and relative strength  $g_j$  of each gain line to maximize the fractional delay  $\overline{\Delta T}_{\text{max}}$  for different values of the signal bandwidth. For single pulse optimization, we use Gaussian pulses with temporal shape as follows:

$$A(t) = \exp(-2\pi^2\Delta\nu^2(t - t_c)^2), \quad (4.8)$$

where  $t_c$  is the temporal peak position, and  $\Delta\nu$  is the signal bandwidth.

When system considerations are taken into account, 128-bit random data trains with return-to-zero modulation are used in both numerical calculation and experiment. A logical “1” bit is represented by a pulse with an input amplitude shape of

$$A(t) = \exp(-t^2/\tau^2) \quad \text{for} \quad |t| < 2\tau, \quad (4.9)$$

where  $\tau$  is the time constant and  $T_{\text{slot}} = 4\tau$  is the length of the time slot. A logical “0” bit is represented by the absence of such a pulse in the time slot. The signal bandwidth  $\Delta\nu$  is related to  $T_{\text{slot}}$  by

$$\Delta\nu = 1/2T_{\text{slot}}. \quad (4.10)$$

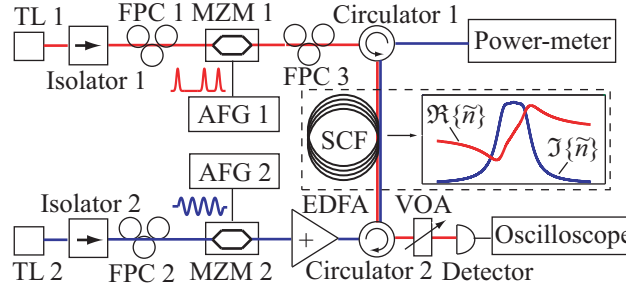


Figure 4.1: Schematic diagram of a SBS-based tunable delay line. TL: tunable laser; FPC: fiber polarization controller; MZM: Mach-Zehnder modulator; AFG: arbitrary function generator; SCF: small-core fiber; EDFA: Erbium doped fiber amplifier; VOA: variable optical attenuator. The inset on the right shows a typical profile of  $\tilde{n}$  for a triple-gain-line medium.

### 4.3 Experimental demonstration

The experiment is performed using single-mode fibers in which the gain features are produced by the stimulated Brillouin scattering (SBS) process [12, 13].

Multiple gain lines are created by amplitude modulating the pump light with a Mach-Zehnder modulator (MZM) [83, 74]. For example, when a driving voltage of the MZM is given by

$$V_{\text{MZM}} = (-V_{\pi} + rV_1/2 + V_1 \cos 2\pi\delta t), \quad (4.11)$$

where  $V_{\pi}$  is the half-wave voltage of the MZM, the pump field after modulation has the form of

$$E_{\text{p,out}} = E_{\text{p,in}} \frac{V_1}{2V_{\pi}} (r + e^{i2\pi\delta t} + e^{-i2\pi\delta t}), \quad (4.12)$$

where  $E_{\text{p,in}}$  is the input pump amplitude. One sees from the above expression that the modulated field contains three spectral lines, the carrier frequency  $\nu_0$ , and two side bands at  $\nu_0 + \delta$  and  $\nu_0 - \delta$ , respectively.

The final resulting SBS-induced gain profiled is the convolution of the pump spec-

trum with the intrinsic SBS Lorentzian gain lineshape. Thus, after amplification by an erbium-doped fiber amplifier (EDFA), such a pump field creates a triple-gain-line (TGL) feature near its Stokes shift frequency with half separation  $\delta$  and peak ratio  $r = g_0/g_1$  between the center and side gain lines. Once the shape of the gain profile is achieved, its magnitude can be tuned continuously by changing the amplification of the EDFA.

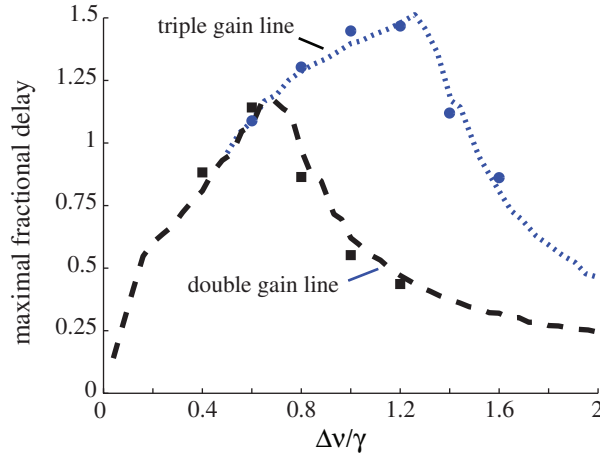


Figure 4.2: Maximum fractional delay for triple and double gain media as bandwidth increases when single pulse metrics are considered.

For optimization with single pulse considerations, we use standard single mode fiber (SMF). The FWHM of the SBS gain line of the SMF is measured to be 29 MHz. Fig. 4.2 shows the numerical prediction and experimental data on the maximum achievable delay for both double and triple gain media as the bandwidth  $\Delta\nu$  increases. In both cases, the  $\overline{\Delta T}_{\max}$  is gain limited for small  $\Delta\nu$ , and becomes amplitude-distortion limited for large  $\Delta\nu$ . By introducing a triple gain line, the distortion is reduced and therefore the peak value of  $\overline{\Delta T}_{\max}$  is increased and its position is moved towards larger bandwidth. As compared to the case of a double-gain medium, the peak value of  $\overline{\Delta T}_{\max}$  is increased about 40% for a triple gain medium, and the corresponding bandwidth is increased by 70% from  $0.75\gamma$  to  $1.3\gamma$ . For  $\Delta\nu = 1.3\gamma$ ,  $\overline{\Delta T}_{\max}$  in the triple gain medium is almost four times the value of  $\overline{\Delta T}_{\max}$  that a double gain medium can achieve.

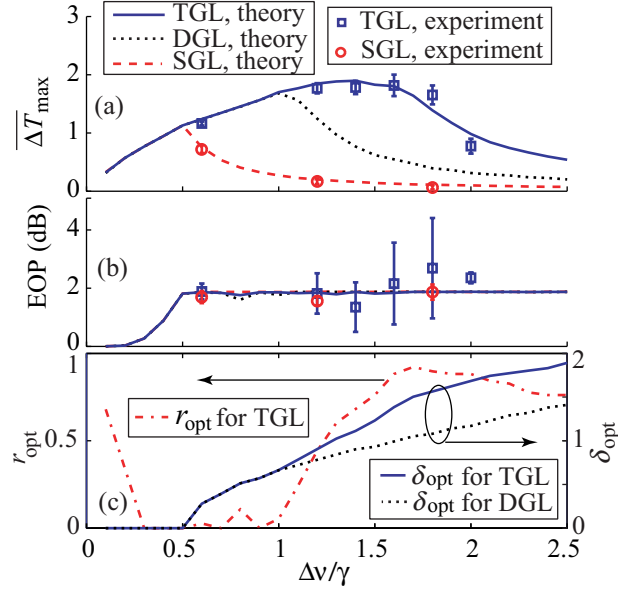


Figure 4.3: (a) Maximum achievable fractional delay  $\overline{\Delta T}_{\max}$ ; (b) corresponding eye-opening penalty EOP; and (c) optimum values of the half separation  $\delta_{\text{opt}}$  and peak ratio  $r_{\text{opt}}$  as functions of normalized bandwidth for the SGL, DGL and TGL media, respectively, when system metrics are considered.

The SBS gain medium, used in the experiment to demonstrate the optimizations based on the system metrics, is 2 km of small-core fiber (SCF). The SBS gain linewidth  $\gamma$  in the SCF is measured to be 25 MHz. Figures 4.3(a) and (b) show  $\overline{\Delta T}_{\max}$  and corresponding EOP as functions of the normalized bandwidth for the single-gain-line (SGL), double-gain-line (DGL) and TGL media, respectively. For a slow-light medium based on a fixed number of gain lines, One sees that there is a peak bandwidth  $\Delta\nu_{\text{peak}}$  at which a largest  $\overline{\Delta T}_{\max}$  can be achieved. For bandwidths less or larger than  $\Delta\nu_{\text{peak}}$ ,  $\overline{\Delta T}_{\max}$  is limited mainly by the maximum gain or the EOP criterion, respectively. As the number of lines incorporated in the gain feature increases, more degrees of freedom are available to optimize the gain and refractive index profile and thus minimize the distortion and ISI. Thus, a larger  $\overline{\Delta T}_{\max}$  at a larger  $\Delta\nu_{\text{peak}}$  can be achieved with an optimum design of relative spacing and peak ratio among the gain lines. As one sees from Fig. 4.3(a), the largest  $\overline{\Delta T}_{\max}$  for a TGL medium is around 1.9, which is about twice the largest value that can be obtained with a SGL medium.

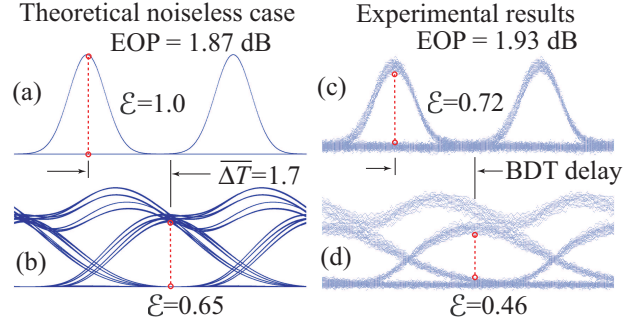


Figure 4.4: The eye diagram of (a) a theoretical noiseless input; (b) a theoretical noiseless output; (c) the actual input in the experiment; and (d) the actual output in the experiment for the optimum design of a TGL medium with  $\overline{\Delta T} \approx 1.9$  at  $\Delta\nu = 1.4\gamma$ . The dotted lines indicate the magnitude of the eye-opening  $\mathcal{E}$  of each cases.

Moreover, its peak bandwidth  $\Delta\nu_{\text{peak}}$  is about 3 times that for a SGL medium. Note that for both SGL and TGL media, the maximum CW gain within the bandwidth reaches our assumed limit of 7 in order to achieve the largest  $\overline{\Delta T}_{\text{max}}$  for each case.

Figure 4.4 shows the eye-diagrams of the input and output in a theoretical noise-free situation [(a) and (b)] and in the experiment [(c) and (d)] for the optimum design of a TGL medium at  $\Delta\nu = 1.4\gamma$  with  $\overline{\Delta T} \approx 1.9$ . The optimum parameters are  $\delta = 1.1\gamma$ ,  $r = 0.68$ , and the peak gain of the data train in the time domain is about 24 dB. One sees that the theoretical prediction and experimental results agree well and that ISI, not noise, is the main source of the eye closure and the associated reduction in data fidelity. Under such circumstances, one also sees that the largest deviation among the peak positions of different “1” bits is almost half a bit slot. Thus, it can be ambiguous and inaccurate to define the delay in terms of the peak position of any individual “1” bit.

For a given bandwidth  $\Delta\nu$ , once the optimum gain profile is obtained (*e.g.*, using the parameters plotted in Fig. 4.3 (c) for a TGL medium), tunable delay can be achieved by changing the magnitude of the gain profile. Figure 4.5 shows the simulated results of  $\overline{\Delta T}$  and EOP as the magnitude of the gain profile (normalized by the optimum value to achieve  $\overline{\Delta T}_{\text{max}}$ ) increases for the optimum designs of TGL media

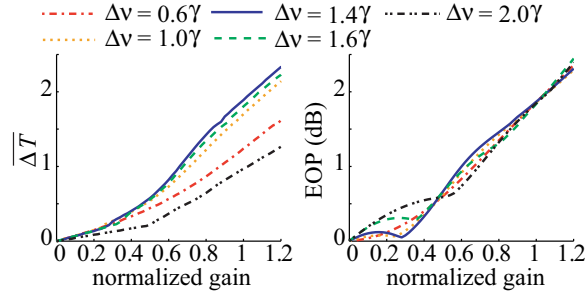


Figure 4.5: (a) Simulated results of fractional delay  $\overline{\Delta T}$ ; and (b) eye-opening penalty EOP as functions of gain (normalized by the gain required to achieve  $\overline{\Delta T}_{\max}$ ) for optimum designs of a triple-gain-medium at various bandwidths.

for various bandwidths. One sees that the delay typically increases linearly first as the gain increases from zero. This is because at small gain the distortion is small so that the BDT delay is consistent with the peak delay of the “1” pulses. As the gain becomes larger, the ISI becomes larger and  $t_{\text{opt}}$  starts to deviate from the peak positions of the “1” pulses, and therefore  $\overline{\Delta T}$  is no longer strictly linearly proportional to gain afterwards but increases faster as gain increases. Meanwhile, the eye-opening penalty also increases slowly at first (see Fig. 4.5(b)) when the distortion is small. For  $\Delta\nu = 1.4\gamma$  [when the overall largest  $\overline{\Delta T}_{\max}$  is achieved; cf. the solid line in Fig. 4.5(b)], in particular, EOP is negligible for the relative gain magnitude less than 0.3. This shows that a good design of a multi-gain-line medium can actually increase the delay with negligible loss in data fidelity.

Our study seems to indicate that by increasing the number of gain lines, the overall gain profile can provide larger fractional delay at larger signal bandwidth. One remaining question is “Is there an ultimate limit on the maximum fractional delay as the number of gain lines increases”? Since the optimal gain profile almost always has a flat top to reduce the amplitude distortion, the overall gain profile will resemble more and more likely to a rectangle shaped gain feature. The maximum achievable delay using different criteria are listed in Table 4.1. Here,  $G_{\max}$  is the maximum intensity exponential gain.

As shown in Table 4.1, the increase of the fractional delay saturates as the overall

Table 4.1: Maximum fractional delay for different gain profiles

	single gain line	double gain line	triple gain line	rectangle gain line
$\overline{\Delta T}_{\max} = 2\pi\Delta\nu\Delta T_{\max}$ ; single pulse consideration				
$G_{\max} = 5$	0.45	0.9	1.15	1.7
$G_{\max} = 7$	0.6	1.2	1.5	2.2
$\overline{\Delta T}_{\max} = \Delta T_{\max}/\tau_{\text{FWHM}}$ ; single pulse consideration				
$G_{\max} = 5$	0.32	0.65	0.83	1.23
$G_{\max} = 7$	0.43	0.87	1.08	1.59
$\overline{\Delta T}_{\max} = \Delta T_{\max}/(T_{\text{slot}}/2)$ ; system consideration				
$G_{\max} = 7$	0.7	1.0	1.2	2.0

gain profile approaches to a rectangular gain profile. No matter what consideration one adopts during the optimization, the maximum fractional delay that can be achieved using multiple closely spaced gain lines is always approximately a factor of two.

## 4.4 Summary

For delay line applications, fractional delay is a major figure of merit. In practice, this quantity is limited by the power level change through the slow-light medium as well as by the distortion introduced on the signal.

A slow-light medium based on multiple, closely spaced gain lines has been studied as a means to increase the fractional delay as compared to a single-gain-line medium. The relative spacing and strength among different gain lines has been optimized under consideration of two sets of criteria, one concentrating on single pulses and physical origins of the distortion and the other based on system performance and system metrics. The theoretical optimization predictions have been demonstrated with a tunable delay line based on SBS slow light in fiber. It has been shown that the maximum achievable fractional delay can almost be doubled at three times larger modulation bandwidth for an optimized triple-gain-line medium as compared to a single-gain-line medium, while high data fidelity is still maintained. Such scheme is

---

applicable in a straightforward way to much higher data rate using techniques that increase the effective linewidth of each gain line [77, 84] or that increase the number of gain lines [75, 78].

# Chapter 5

## Continuously Tunable, Positive and Negative Time Delays with Optimized Stimulated Brillouin Scattering Slow and Fast Light

### 5.1 Background

In a synchronized telecommunication system, each “0” or “1” bit is required to be centered with respect to a reference time clock or slot. In practice, however, the temporal positions of each data bit within an optical signal train can experience random delay or advancement due to various reasons, e.g., jitter from the modulator, random group delay fluctuation through a long optical fiber, etc. In such cases, the pulse train needs to be re-centered with respect to the time clock or time slots, and a tunable slow-light element is a good candidate for these re-timing applications such as data re-synchronization and jitter correction. For these re-timing applications, one would naturally desire a single timing element that could provide both positive and negative temporal adjustment. However, most demonstrated slow-light devices

cannot be reconfigured easily to work in the fast-light regime, and vice-versa. It has been shown recently [85] that one can achieve tunable delay and advancement by adjusting the separation between two Lorentzian gain lines. However, in the process of tuning the separation, both the gain and group index profiles can become highly frequency dependent over the signal bandwidth. This leads to significant pulse distortion and degradation of the signal fidelity, which becomes impractical for real applications. Other fast light has also been investigated in SBS systems [85, 86, 87, 88]. These fast-light techniques include working at the center of an absorption (e.g., SBS anti-Stokes) resonance center, using a saturable gain medium, using self-advancement of SBS pump field, etc. However, most fast-light techniques reported so far are not optimized and therefore can only have very limited fractional advancement.

In this chapter, we propose and demonstrate a practical design to realize continuously tunable slow and fast light module to provide positive and negative time delays. Furthermore, we use optimized gain profile for both slow- and fast-light operations, which gives a total tuning range of more than one pulse duration with very well controlled signal distortion.

## 5.2 Theory of slow and fast light using gain media

To achieve both positive and negative time delays, one needs to achieve both slow and fast light. For a single-frequency continuous-wave pump field, the SBS-induced complex refractive index near the Stokes frequency  $\nu_0$  can be approximated by a Lorentzian function as follows:

$$\tilde{n}(\nu) = n_{\text{bg}} + \frac{cg}{4\pi\nu_0} \frac{\gamma}{\nu - \nu_0 + i\gamma}, \quad (5.1)$$

where  $n_{\text{bg}}$  is the background index of refraction,  $c$  is the speed of light in vacuum, and  $g$  and  $\gamma$  are the peak gain coefficient and the SBS linewidth, respectively. The

real part of  $\tilde{n}$  has a large swing in the vicinity of the resonance, resulting in slow and fast light in the center and wings of the resonance, respectively. The general principle of switching our module between slow- and fast-light operations is to reshape the SBS-induced gain profile by modulating the pump field differently, so that the signal spectrum lies either within the center region of a single gain feature or within the transparent window between two separated gain features.

In this work, we define the fractional delay as  $\overline{\Delta T} \equiv \Delta T/\tau_p$ , where  $\Delta T$  is the absolute delay of the peak position of the pulse as compared to that of a reference, and  $\tau_p$  is the temporal full width at half maximum (FWHM) of the input pulse.

In practice,  $\overline{\Delta T}_{\max}$  is often limited by the maximum distortion or change in power level that a signal is allowed to acquire in passing through a slow-light material [72]. To achieve large fractional delay and advancement to reach a total tuning range larger than a pulse width, we choose two optimized gain profiles with low distortion for slow- and fast-light operation. In this manner, signal distortion is well controlled through the entire tuning process. Tunable delay and advancement are then achieved by controlling the pump power.

In the slow light regime, we use multiple closely spaced gain lines for slow-light operation [74, 73, 89]. The overall complex refractive index profile near the Stokes resonance is given by

$$\tilde{n}_{\text{total}}(\nu) = n_{\text{bg}} + \tilde{n}_{\text{intrinsic}}(\nu) * S_{\text{pump}}(\nu), \quad (5.2)$$

where  $\tilde{n}_{\text{intrinsic}}$  is the SBS-induced refractive index profile given by a CW pump field with unit power [see Eq. (5.1)],  $S_{\text{pump}}(\nu)$  denotes the gain spectrum of the actual pump field, and  $*$  denotes the convolution operation.

To achieve low-distortion slow light, we optimize the spacing and the relative strength to form a broad, flat-top gain profile. The desired pump spectrum can be obtained using amplitude modulation on the pump field [74, 73, 89]. One can also extend this concept to the use of a continuous pump spectrum to achieve a gain profile

as broad as tens of gigahertz [90].

For fast-light operation, we use two separated gain features, which leaves a transparent, fast-light window in between. Note that the maximum achievable fractional advancement of such a separated double gain medium is determined by factors that can be different from those for a slow-light medium [72]. First, since the signal spectrum sits between two gain features, the wing regions of the signal spectrum gets amplified more than the center. This leads to spectrum broadening, and consequently the output pulses become narrower in the time domain. Furthermore, residual frequency components due to optical noise in the input signal or spontaneous emission from the gain medium that fall on the two gain peaks get amplified much more strongly than the main spectrum of the signal. Such amplified noise can form a beating pattern in the time domain, which leads to pulse distortion and inter-symbol interference [80]. Thus, instead of the maximum pump power the system can provide, this noise constraint determines the maximum continuous-wave (CW) gain the system can have at the two gain peaks, and hence further limits the maximum advancement that such a fast-light element can produce. Given such a limit, we use two separated, flat-top gain profiles to further increase the fractional advancement. In specific, each flat-top gain profile is created using three closely spaced gain lines.

### 5.3 Experimental demonstration using stimulated Brillouin scattering

The schematic diagram of our experiment is shown in Fig. 5.1. We start with a stable laser source (Koshin LS-601A) at a frequency  $\nu_0$  near 1550 nm, and we modulate the field using a sinusoidally driven Mach-Zehnder (MZ) intensity modulator (IM 1 in Fig. 5.1), which is biased for minimum DC transmission. The modulator creates two frequency sidebands,  $\nu_0 \pm \Omega_B$ , where  $\Omega_B \approx 10.6$  GHz is the SBS Stokes shift frequency of our single-mode fiber (SMF). The modulated field then propagates through 6 km

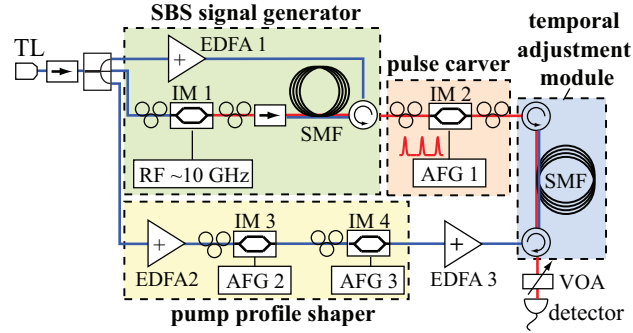


Figure 5.1: Schematic diagram of a bidirectionally tunable optical timing element using stimulated Brillouin scattering. TL: tunable laser; IM: intensity modulator; AFG: arbitrary function generator; SMF: single-mode fiber; EDFA: erbium doped fiber amplifier; VOA: variable optical attenuator.

of SMF with a strong counter-propagating pump field at  $\nu_0$ . The SBS process amplifies the component at the Stokes frequency  $\nu_0 - \Omega_B$  and attenuates the anti-Stokes frequency  $\nu_0 + \Omega_B$ , and the SMF acts like a frequency purifier. The optical field after this SBS purification stage is checked with an optical spectrum analyzer, and the power of the Stokes field at  $\nu_0 - \Omega_B$  is 20 dB higher than those at  $\nu_0$  and  $\nu_0 + \Omega_B$ . A second MZ intensity modulator (IM 2) is then used to carve out a train of Gaussian pulses with FWHM width  $\tau_{FWHM} = 6.5$  ns before the signal is sent into the SBS temporal adjustment module.

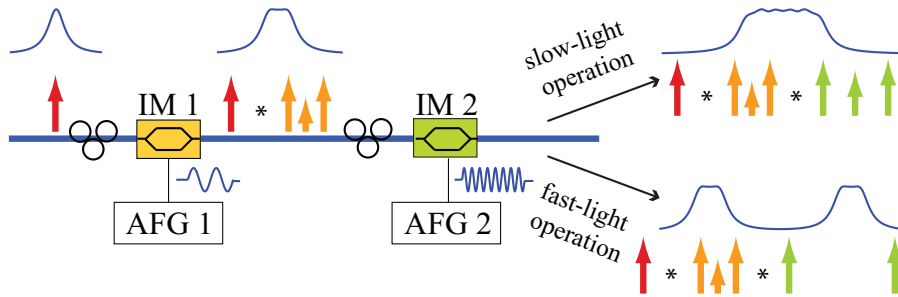


Figure 5.2: Schematics of creating multiple gain line profile using dual-stage modulation method. The orange and green arrows indicate the created discrete frequency side bands with each modulation stage.

A two-stage pump modulation is used to reconfigure the two optimized SBS gain

profiles between slow- and fast-light operations. We use one sinusoidally driven MZ intensity modulator (IM 3 in Fig. 5.1) to create three closely spaced frequency lines which lead to a single flattened gain feature approximately 80 MHz wide [73]. Note that one can use a more complicated modulation method [78, 91] to create more lines and to form a broader gain feature. A second MZ intensity modulator (IM 4) is used to configure the final gain profile for slow- or fast-light operation. The modulator is always biased at minimum DC transmission, and it is sinusoidally modulated at frequency  $f_s$ . This setting splits the gain feature produced by IM 3 into two, separated by  $2f_s$  from each other (see Fig. 5.2). For slow-light operation, the optimum value of  $f_s$  is approximately 34 MHz, and the two gain features are partially overlapped to form a broad, flat-top gain feature [see Fig. 5.3(a)]. For fast-light operation, the optimum value for  $f_s$  is approximately 148 MHz. The resulting two flat-top gain profiles are separated enough to leave a transparent fast-light window in between for our signal [see Fig. 5.3(c)], but they are also close enough that signal experiences a significant fast-light effect.

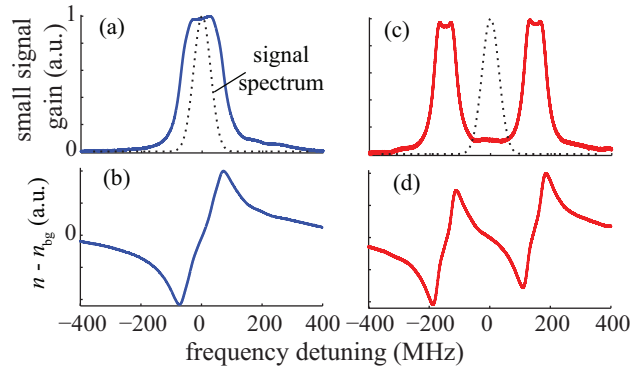


Figure 5.3: Measured small signal gain and calculated induced refractive index change as functions of frequency detuning for slow light [(a) and (b)] and fast light [(c) and (d)] configurations. The black dotted lines in (a) and (c) show the power spectrum of Gaussian pulses with FWHM of 6.5 ns.

To illustrate the low-distortion advantage of our optimized gain profiles for the slow- and fast-light operations, we performed a numerical calculation of the width of the output pulse as the delay is increased by tuning up the pump power. Since the

temporal shape of the output pulse can be irregular, such as having multiple lobes, it is more accurate to describe the temporal width of the pulse using its root-mean-square (RMS) width  $\tau_{\text{rms}}$  as follows:

$$\tau_{\text{rms}} \equiv \sqrt{\langle t^2 \rangle - \langle t \rangle^2}, \quad (5.3)$$

where

$$\langle t \rangle = \frac{\int t |A(t)|^2 dt}{\int |A(t)|^2 dt}, \quad (5.4)$$

$$\langle t^2 \rangle = \frac{\int t^2 |A(t)|^2 dt}{\int |A(t)|^2 dt}, \quad (5.5)$$

and where  $A(t)$  is the amplitude of the pulse. The temporal RMS width of the input Gaussian pulses is  $\tau_{\text{rms}} = \tau_{\text{FWHM}} / (2\sqrt{2\log(2)}) = 2.76$  ns.

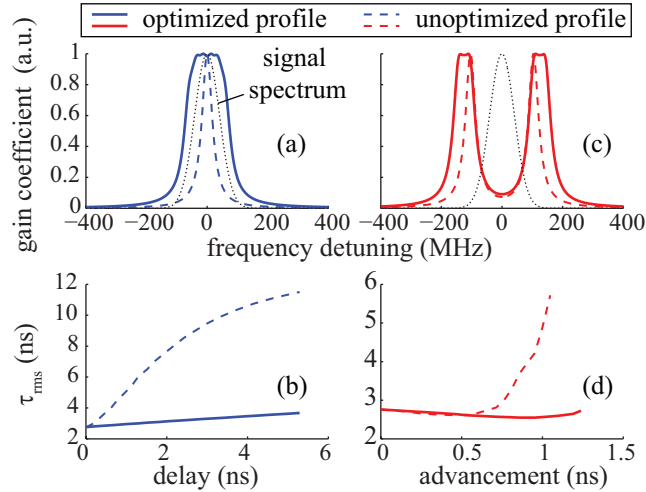


Figure 5.4: Calculated optimized and un-optimized gain profiles as functions of frequency detuning for slow light (a) and fast light (c) configurations, and the RMS width of the output pulse for different gain profiles as functions of peak delay for slow light (b) or advancement for fast light (d) configuration.

Figure 5.4 shows the numerically calculated RMS width  $\tau_{\text{rms}}$  of the output pulse propagating through optimized and un-optimized slow-light and fast-light media as

the delay or advancement increases. For the slow light configuration, the un-optimized gain profile is a single Lorentzian gain line [see the blue dashed line in Fig. 5.4(a)]. Since the signal spectrum is broader than the width of a single gain line, the pulse becomes significantly broadened as the delay increases. At the largest delay of 5.29 ns (a fractional delay of 0.82), the RMS width of the output pulse through our optimized slow-light medium is approximately 3.6 ns while a single-gain-line medium results in a RMS width of 11.5 ns. For the fast-light operation, the un-optimized gain profile is two Lorentzian gain lines separated by 206 MHz [see the red dashed line in Fig. 5.4(c)]. When the advancement is small, the RMS width of the output pulse through the un-optimized medium is approximately the same as the optimized medium. However, as the advancement becomes large, the noise amplified by the two gain peaks quickly distorts the output pulse for the un-optimized medium while the RMS width of the output pulse through the optimized medium is still well maintained. Note that this calculation assumes that the input pulse is noiseless. In a real experiment, the noise components at the two gain peaks can get amplified much faster, which leads to further distortion of the output pulse.

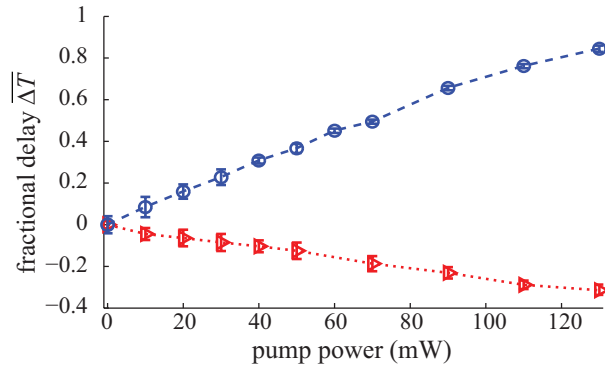


Figure 5.5: Measured fractional delay (circles) and advancement (triangles) as functions of the pump power. The error bars are the standard deviations.

The modulated pump profile is amplified using an erbium-doped fiber amplifier (EDFA 3 in Fig. 5.1) and launched into 4 km of SMF counter-propagating with the signal field. A variable optical attenuator (VOA) is used right before the output of the

module [73], and the VOA is set at constant output power mode to keep the output power at a fixed level. The amount of delay or advancement is adjusted by controlling the output power level of EDFA 3. Figures. 5.3(a) and (c) show the measured small signal gain for the fast- and slow- light configurations, respectively. One sees that the optimized flattened gain feature and the transparent window are adequately broad for the signal spectrum shown as the dotted lines. Figures. 5.3(b) and (d) show the corresponding refractive index change calculated according to the Kramers–Kronig relations. One clearly sees the slow- and fast-light regimes, indicated by positive and negative slopes of  $n$ , in the vicinity of the center frequency for the two respective configurations. Note that the two chosen gain profiles and their corresponding group index profiles for slow- and fast-light operations are quite uniform over our signal bandwidth, and therefore one can achieve large fractional delay and advancement with very low pulse distortion.

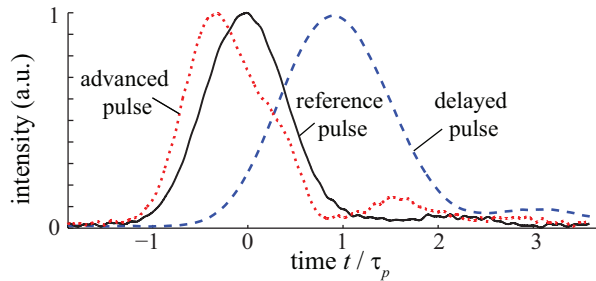


Figure 5.6: Output pulse as a function of time for reference, slow-light, and fast-light configurations.

Figure 5.5 shows the measured delay and advancement as functions of the pump power. Using a maximum pump power of 130 mW, we have achieved a fractional delay and a fractional advancement of 0.82 and 0.31, respectively, giving a total continuous tuning range of 1.13 pulse width, or about 7.35 ns for 6.5-ns pulses. Note that our setup can switch between slow- and fast-light regimes electronically without the need of rearranging the components. The FWHM of the delayed and advanced pulses are approximately 8.7 ns and 6.7 ns, respectively (see Fig. 5.6). Note that we do not

use the RMS width of the experimentally measured pulse because, in the presence of optical and detector noise, the value of  $\tau_{\text{rms}}$  does not converge as the size of the truncated time window increases, and therefore it no longer reflects accurately the width of the pulses. The fractional advancement can be further improved if each of the double gain features is broadened further and the noise level of the input signal is reduced.

## 5.4 Summary

In this chapter, we have proposed and demonstrated a single, continuously tunable, low-distortion module for delaying or advancing optical pulses using stimulated Brillouin scattering. The slow- or fast-light operation is realized using dual-stage intensity modulation, with different optimized modulation functions, on the pump field. We have continuously tuned the temporal position of 6.5 ns FWHM Gaussian pulses from a fractional advancement of 0.31 to a fractional delay of 0.82, giving a total tuning range of more than one pulse width, while the pulse distortion is kept low through out the entire tuning range. Such a device can be used for bidirectional jitter correction and data resynchronization.

# Chapter 6

## Channelized Slow Light For Discretely Tunable Optical Packet Delays

### 6.1 A fundamental limit on maximum achievable fractional delay of a slow-light element

As discussed in the previous two chapters, a primary figure of merit for the evaluation of the performance of slow-light delay devices is the maximum achievable fractional delay [70] (also known as the delay-bandwidth product). In practice, this quantity is often limited not by the amount by which the velocity can be reduced but rather by the maximum distortion or change in power level that a signal is allowed to acquire in passing through such a material [72].

To increase the maximum achievable fractional delay, many schemes [35, 73, 84] have been proposed for broadening and flattening the intrinsically narrow resonance structures. Nonetheless, there exist serious more fundamental limits [92, 76, 38] on the maximum fractional delay that a single-channel slow-light medium can produce.

Of particular interest is the Miller limit, which relates the maximum achievable fractional delay  $\tau_g \Delta\nu$  ( $\tau_g$  and  $\Delta\nu$  being the time delay and the signal bandwidth, respectively) of a device of size  $L$  with its average refractive index  $n_{\text{avg}}$  and its maximum variation of  $\Delta n$  over  $\Delta\nu$  near the center wavelength  $\lambda_0$  through the relation [38]

$$\tau_g \Delta\nu \leq n_{\text{avg}} L \Delta n / (\sqrt{3} \lambda_0). \quad (6.1)$$

Here we review briefly how one can approach this limit using an ideal, lossless, distortion-free slow-light medium. The frequency-dependent refractive index of an ideal slow-light medium near a reference frequency  $\nu_0$  is given by,

$$n(\nu) = n(\nu_0) + \frac{n'_g}{\nu_0} (\nu - \nu_0), \quad (6.2)$$

where  $n'_g = n_g - n$  is the relative group index and where  $n_g = n + \nu dn/d\nu$  is the group index. If this expression is valid for the entire signal bandwidth, than the maximum change in refractive index is given by

$$\Delta n_{\text{max}} = \frac{n'_g}{\nu_0} \Delta\nu, \quad (6.3)$$

where  $\Delta\nu$  is the signal bandwidth. The group delay a signal pulse experienced by propagating through such a medium is given by

$$\Delta T = n'_g L / c. \quad (6.4)$$

Substituting Eq. (6.3) into the above equation, one has the following expression:

$$\Delta T = \frac{\Delta n_{\text{max}} \nu_0}{\Delta\nu} L / c, \quad (6.5)$$

or

$$\begin{aligned}\Delta\nu\Delta T &= \Delta n_{\max}\nu_0 L/c \\ &= \Delta n_{\max}L/\lambda_0.\end{aligned}\tag{6.6}$$

This expression is very similar to Eq. (6.1) except for some numerical constant. The exact derivation of Eq. (6.1) can be obtained more formerly by following Ref. [38].

## 6.2 Principle of channelized slow light

Channelized slow light [93, 94, 95, 96, 97] has recently been proposed as a procedure for improving the performance of slow-light devices based on materials with an intrinsically narrow working bandwidth. The basic idea of channelization is to create separate narrow-band slow-light spectral channels for different frequency components of a broadband signal and subsequently combine these outputs to achieve large fractional delays of broadband signals. One proposal for channelized slow light is to create multiple spectral resonances in, e.g., a photorefractive crystal [94] or an electromagnetically induced transparency medium [96]. While previously reported works are capable of delaying a pulse train with discrete spectral components, they typically have serious distortion problems when dealing with signals with a continuous spectrum [94]. Moreover, such methods cannot exceed Miller’s limit since they all fall into the general category of “one-dimensional” devices. Another type of proposal uses dispersive elements such as gratings and prisms to form a continuous span of spatially separated channels [93, 94, 95, 97]. Such a treatment can effectively increase the working bandwidth, but it cannot increase the maximum fractional delay [95]. This is because the effective group index of the channelized device is reduced by the same factor as by which the working bandwidth is increased through the use of such channelization. As a result, none of the proposals of channelized slow light so far can overcome Miller’s limit for a signal with a continuous spectrum.

Here, we propose a new, practical design of a channelized delay device which, by using finite number of spatially separated channels, can overcome Miller's limit.

We first review the operation of a linear, single-channel slow-light element. The transmission through such an element can be described using a frequency-domain transfer function  $\mathcal{H}(\nu)$  according to the relation

$$E_{\text{out}}(\nu) = E_{\text{in}}(\nu)\mathcal{H}(\nu), \quad (6.7)$$

where  $E_{\text{in}}(\nu)$  and  $E_{\text{out}}(\nu)$  are the complex amplitude spectra of the input and output fields, respectively. The transfer function  $\mathcal{H}(\nu)$  is given by

$$\mathcal{H}(\nu) = \mathcal{A}(\nu)e^{i\phi(\nu)} = \exp[i2\pi\nu\tilde{n}(\nu)L/c], \quad (6.8)$$

where  $\mathcal{A}(\nu)$  and  $\phi(\nu)$  are the amplitude and phase response functions, respectively,  $\tilde{n} = n_r + in_i$  is the complex refractive index of the medium,  $L$  is the length of the medium, and  $c$  is the velocity of light in vacuum.

We consider a slow-light medium to be ideal if it possesses constant group index and gain over the signal bandwidth. In this situation, the real part of the refractive index  $n_r$  is given by (see the dotted line in Fig. 6.1)

$$n_r(\nu) = n_r(\nu_0) + \frac{n'_g}{\nu_0}(\nu - \nu_0), \quad (6.9)$$

where  $\nu_0$  is some center frequency,  $n'_g = n_g - n_r(\nu_0)$  is the reduced group index, and  $n_g = n_r + \nu dn_r/d\nu$  is the group index of the medium near  $\nu_0$ . Note that for any material medium  $n_r(\nu)$  and  $n_i(\nu)$  are related through the Kramers-Kronig (K-K) relations, and it is thus very difficult to design an ideal slow-light medium with large, uniform group index  $n_g$  and uniform  $n_i$  over a large bandwidth.

Here, we propose a new design for channelized slow light. The input signal is first spectrally sliced into  $M$  spatially separated channels with a frequency spacing of

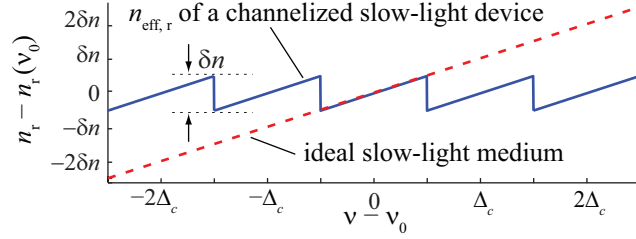


Figure 6.1: Refractive index as a function of the detuning from some center frequency  $\nu_0$  for an ideal slow-light medium and for a channelized slow-light medium. Here  $\delta n = n'_g \Delta_c / \nu_0$  is the maximum refractive index variation for both types of medium within the frequency interval  $\Delta_c$ .

$\Delta_c$ . The frequency components in each spectral channel then propagate through the corresponding narrow-band slow-light medium of length  $L$  before they are combined to restore a delayed output signal.

Since such a channelized device is still a linear system with single input and output ports, the transmission through the device can also be described by means of the transfer function  $\mathcal{H}(\nu)$  of Eq. (6.8). For the ideal case in which the spectral slicing is perfect (i.e., the transmission window in each channel is of rectangular shape without any phase distortion [35]) and the slow-light medium of length  $L$  in each channel is ideal, the transfer function of such a channelized delay device is given by

$$\mathcal{H}(\nu) = \exp[i2\pi\nu\tilde{n}_{\text{eff}}(\nu)L/c], \quad (6.10)$$

where  $\tilde{n}_{\text{eff}}(\nu)$  is the effective complex refractive index of the device and its real part  $n_{\text{eff},r}(\nu)$  is given by

$$n_{\text{eff},r}(\nu) = n_{\text{eff},r}(\nu_0) + \frac{n'_g}{\nu_0} (\nu - \nu_0 - m\Delta_c), \quad (6.11)$$

for frequency components within the  $m^{\text{th}}$  channel (i.e., for  $|\nu - \nu_0 - m\Delta_c| < \Delta_c/2$ , see also the solid line in Fig. 6.1). Because  $\tilde{n}_{\text{eff}}$  is not the property of a single uniform medium but rather is determined by distinct, spatially-separated media for frequencies within different spectral channels, it is possible to design such a channelized delay

device for which the effective group index and gain are constant over arbitrarily large bandwidth. Note that the entire channelized element is still a causal, linear element. However, because we can use non-minimal phase filters [98] to construct the spectral slicers, the magnitude and the phase of the total transfer function  $\mathcal{H}(\nu)$  of such a channelized element do not have to obey the usual Hilbert transform relations [98, 99]. Note that causality only requires that the real and imaginary part of the response function obeys K–K relation.

One sees from Eq. (6.11) that the phase response function  $\phi(\nu)$  is discontinuous at the boundaries of neighboring channels. The difference in the values of  $\phi(\nu)$  between the two sides of any boundary between adjacent channels is given by

$$\Delta\phi \approx k_0\delta n_{\text{eff}}L = 2\pi n'_g\Delta_c L/c, \quad (6.12)$$

where  $\delta n_{\text{eff}} = n'_g\Delta_c/\nu_0$  is the difference in the values of the effective refractive index of the device between the two sides of the channel boundary (cf. Fig. 6.1). This phase jump of  $\Delta\phi$  can lead to distortion and break up of the reconstructed output pulse, unless the output phase of each channel is actively adjusted by means of some additional phase shifter [94]. However, the transfer function  $\mathcal{H}(\nu)$  becomes automatically continuous (that is, there is no need for further phase adjustment) when

$$\Delta\phi = 2\pi N, \quad (6.13)$$

where  $N$  is any integer. In such cases, the difference between the transfer function at one side of a channel boundary and the other is a multiplicative factor of  $\exp(i\Delta\phi) = 1$ . Therefore, one can achieve a delayed output signal without any distortion. For a channelized device with a fixed length  $L$  and channel spacing  $\Delta_c$ , the condition of Eq. (6.13) indicates that the reduced group index  $n'_g$  of each channel needs to satisfy

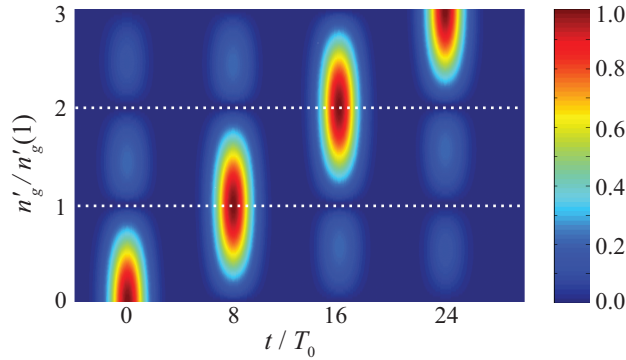


Figure 6.2: False-color representation of the amplitude of the output signal propagating through an ideal channelized delay device as a function of time and of the value of  $n'_g$ . Here the input signal is a Gaussian pulse with a half width to the  $1/e$  intensity value of  $T_0$ , and the channel spacing  $\Delta_c$  is set equal to  $1/(8T_0)$ . The time axis is set so that  $t = 0$  indicates no delay as in the case in which  $n'_g = 0$ .

the following condition:

$$n'_g(N) = \frac{Nc}{L\Delta_c}. \quad (6.14)$$

Under such conditions, the transmission through the channelized delay device is equivalent to that through an ideal slow-light medium with the same length  $L$  and reduced group index  $n'_g = n'_g(N)$  over the entire signal bandwidth. Thus, a distortion-free signal can be produced at the output port of the device with a group delay  $\tau_g(N)$  given by

$$\tau_g(N) = \frac{n'_g(N)L}{c} = \frac{N}{\Delta_c}. \quad (6.15)$$

Some numerical predictions based on these considerations are displayed graphically in Fig. 6.2. Here we consider an input signal in the form of a Gaussian pulse and we calculate the output pulse shape through use of the transfer function of Eq. (6.10). The amplitude of the output is then plotted against time on the horizontal axis and the reduced group index  $n'_g$  on the vertical axis. We see that for specific values of  $n'_g$  (see the white dotted line in Fig. 6.2) the output is in the form of a well defined

pulse, whereas for other values of  $n'_g$  pulse breakup occurs. Since the values of  $n'_g$  that allow an undistorted output pulse are spaced discretely at integer multiples of  $c/(L\Delta_c)$ , the possible time delays are also distributed discretely in integer multiples of the time interval  $\Delta_c^{-1}$ .

For an input signal of a bandwidth  $\Delta\nu$ , the number of required channels is  $M = \Delta\nu/\Delta_c$ . Moreover, the maximum variation in the (effective) refractive index of the channelized device is given by  $\Delta n = n'_g\Delta_c/\nu_0$ , which is independent of the signal bandwidth. Thus, the fractional delay can be written terms of  $\Delta n$  as follows:

$$\tau_g\Delta\nu = \frac{n'_gL\Delta\nu}{c} = \frac{\Delta n\nu_0L\Delta\nu}{\Delta_c c} = \frac{M\Delta nL}{\lambda_0}. \quad (6.16)$$

This equation is of similar form to the expression of Miller's limit [cf. Eq. (6.1)]. Besides the difference of some numerical constants, our expression has a factor of  $M$  in the numerator. Since  $M$  is a free design parameter determined by the channel spacing relative to the signal bandwidth, the fractional delay of a channelized delay device is not restricted to Miller's limit. Indeed, there is no obvious limit to how large the fractional delay can become in a channelized device.

Note that in our proposed channelized device, frequency components in different spectral channels also propagates through different physical channels. In such a case, if one modifies Miller's limit so the length of device "L" is modified into the sum of the length of all physical channels, than the maximum achievable delay of our proposed channelized device is still consistent with Miller's limit.

Let us next consider not a single pulse but rather a wave train (data packet) in the form of  $B$  pulses, each with a temporal spacing of  $\tau_b$ . The duration of this wave train is then of the order of  $\tau_p = B\tau_b$ . We want to determine the extent to which we can achieve a large fractional delay of the entire wave train. The ability to perform such packet delay is important for various applications such as all-optical buffering and routing. When the condition of Eq. (6.14) is satisfied, the fractional delay of the

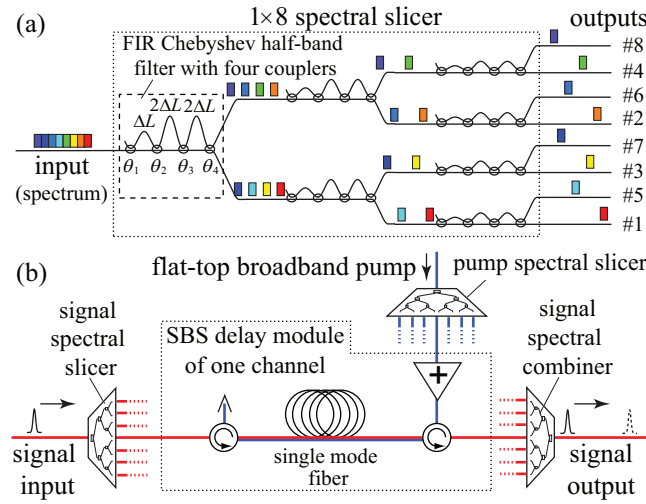


Figure 6.3: Schematic diagrams of (a) a  $1 \times 8$  spectral slicer using cascaded half-band filters; and (b) a channelized SBS slow-light delay element.

entire data packet is given by

$$\frac{\tau_g(N)}{\tau_p} = \frac{n'_g(N)L}{cB\tau_b} = \frac{N}{\Delta_c B\tau_b}. \quad (6.17)$$

One sees that when the channel spacing  $\Delta_c$  satisfies the following condition:

$$\Delta_c = 1/(B\tau_b), \quad (6.18)$$

the channelized element can achieve discretely tunable delays that are integer multiples of the time duration of the entire data packet. Crucially, no dynamic control of the phase of the output of each channel is required to achieve this control of the signal delay.

## 6.3 A numerical example using stimulated Brillouin scattering slow light

To illustrate more explicitly the promise of channelized slow-light devices, we next present a practical design for a channelized slow-light buffer for high speed telecommunication systems and we analyze its performance. We consider a signal data rate of 40 Gbps. Each ‘1’ bit is represented by a Gaussian pulse and a ‘0’ bit is represented by the absence of the pulse. The temporal full width at half maximum (FWHM) of the ‘1’ bit is 12.5 ps, which is consistent with a return-to-zero (RZ) amplitude modulation format of 40 Gbps with 50% duty cycle. For illustrative purposes we consider a data packet containing 4 bits. In order to achieve packet delays, the channel bandwidth is determined, according to Eq. (6.18), to be  $\Delta_c = 10$  GHz. We choose the total number of channels to be  $M = 7$  to cover the entire signal spectrum [as indicated by the dotted line in Fig. 6.4(a)].

As an example, we construct the spectral slicer by cascading a series of flat-top finite impulse response (FIR) Chebyshev half-band filter with 4 couplers [100] as shown in Fig. 6.3(a). After the spectral components in each channel are delayed, we use another spectral slicer in a reverse fashion to combine all the spectral components to restore the broadband signal. The two spectral slicers are designed to have opposite dispersions [101] so that the cascaded transfer function of the two slicers has negligible phase distortion.

We choose stimulated Brillouin scattering (SBS) as the slow-light mechanism [12, 13] to be implemented in each spectral channel. A spool of single mode fiber is contained in each channel, and the delay is controlled by selecting the appropriate pump power for each channel. The SBS Stokes shift frequency  $\Omega_S$  of the single mode fiber at the operating wavelength of 1550 nm is assumed to be a typical value of 12 GHz. The SBS pump-field spectral profile for each signal channel is achieved by filtering a broadband flat-top pump field (using, e.g., current modulation [102])

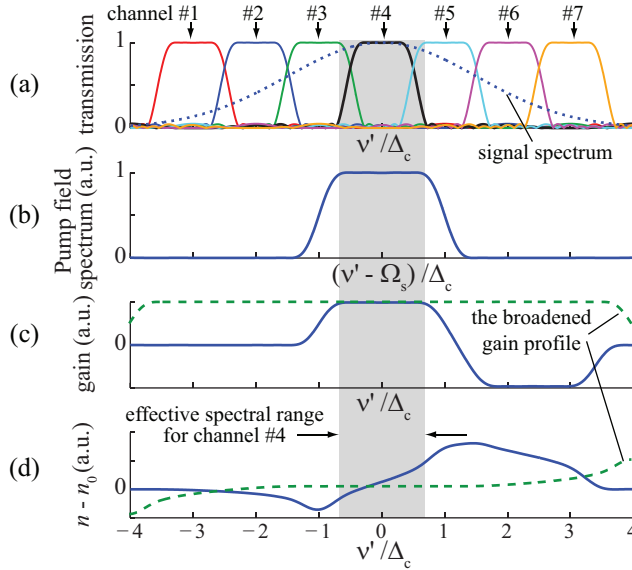


Figure 6.4: (a) Transmission of each of the seven physical signal channels of a channelized SBS delay element; (b) corresponding pump field spectrum for one particular signal channel (channel #4); and the SBS-induced (c) gain and (d) refractive index variation as functions of the detuning for channel #4 (solid line) and for a broadened gain profile (dashed line), respectively.

through an additional spectral slicer. The schematic diagram of the channelized delay element is plotted in Fig. 6.3(b). For simplicity, we show the SBS delay line of only one signal channel. Note that the use of spectral slicers has associated insertion loss, which is typically frequency-insensitive. Such losses would reduce the signal power level, which may reduce the signal-to-noise ratio when the signal is detected. However, SBS is a gain-induced slow-light process, and therefore such losses can be compensated by the SBS gain or by adding an additional amplifier module after the channelized device. Moreover, since only the frequency components within the SBS gain profile (which in our case only covers the signal bandwidth) experience the gain, the SBS process acts like a bandpass filter and may actually reduce the optical noise level outside the signal bandwidth and consequently increase the optical signal-to-noise ratio.

The transmissions windows of the seven signal spectral channels are plotted in

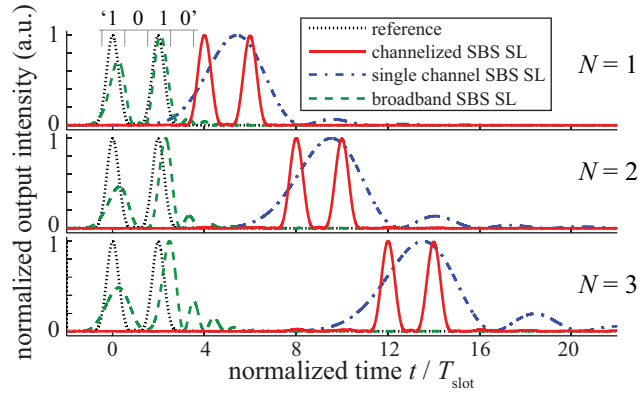


Figure 6.5: Outputs of a 40 Gbps, RZ data train ‘1010’ after propagating through a channelized SBS delay element with  $\Delta_c$  of 10 GHz (solid line), a single channel narrow-band SBS delay element (dash-dotted line) and a single channel broadband SBS delay element (dashed line), respectively. The dotted line is the reference output.

Fig. 6.4(a). Figure 6.4(b) shows the pump field profile for signal channel #4, and the resulting gain and refractive index as functions of frequency detuning  $\nu'$  are plotted in Figs. 6.4 (c) and (d), respectively. One sees that both  $g$  and  $n$  are very close to those of an ideal slow-light medium with constant group index and gain over the entire transmission window of the signal channel (see the gray region in Fig. 6.4).

Next, we numerically model the propagation of a wave packet containing the data stream of ‘1010’ through the channelized delay element. For comparison, we also treat the transmission through two other types of single-channel delay elements. One is an narrow-band delay element which is equivalent to channel #4 of our channelized device. The other has a flat-top broadband gain profile [see the dashed lines in Fig. 6.4 (c) and (d)] across the entire 70 GHz signal bandwidth, which is equivalent to the case in which the spectral channels are spatially overlapping. For the second element, we assume that the anti-Stokes SBS absorption features are compensated (e.g., using multiple pump fields [103, 104]) and the signal experiences only the 70 GHz broadband gain feature.

The output waveforms for delays of 1, 2 and 3 packet lengths are plotted as the solid lines in Figs. 6.5(a)-(c), respectively. One sees that our channelized delay element

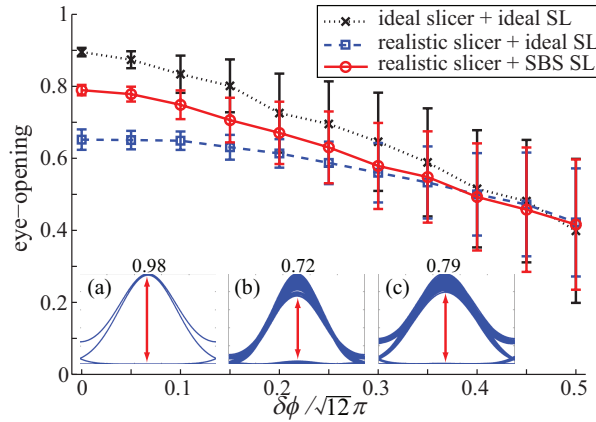


Figure 6.6: Eye-openings of three channelized devices as functions of the standard deviation phase noise level  $\delta\phi$  among different spectral channels. The insets show typical eye-diagrams for (a) an ideal channelized slow-light device; (b) an channelized device with realistic spectral slicers and ideal slow-light media; and (c) an realistic channelized SBS slow-light device, respectively. The corresponding eye-openings are given on top of each eye-diagram, respectively.

can achieve large packet delays with nearly no pulse distortion because it provides uniform effective group index and gain over the entire 70 GHz signal bandwidth.

The outputs of the other two types of delay elements with the same maximum (line-center) CW gain are also plotted for comparison. One sees that the narrow-band single-channel delay element achieves similar amount of delay (see the dash-dotted lines in Fig. 6.5) because  $n'_g$  within its working bandwidth is the same as that in our channelized element. However, because its 12 GHz working bandwidth is much less than the 70 GHz signal bandwidth, significant pulse broadening occurs at the output and the data information of ‘1010’ is completely lost.

On the other hand, the broadband delay element possesses enough working bandwidth for the signal, but the delay is very limited (see the dashed lines in Fig. 6.5) because  $n'_g$  decreases significantly [see the dashed line in Fig. 6.4(d)] as a consequence of the broadening of the gain. Furthermore, the output signal also shows large distortion because  $n'_g$  is not uniform over the signal bandwidth.

For practical applications, it is important to evaluate the performance of our chan-

nelized delay module under the influence of imperfections. In particular, we consider the influence of relative phase fluctuations among the different spectral channels on the quality of the restored output signals. Such phase fluctuations can be induced by e.g., temperature fluctuations of individual slow-light elements (fibers in our case), etc., which introduce the additional random phase  $\delta\phi(m)$  to the phase response function  $\phi_m(\nu)$  for the  $m^{\text{th}}$  spectral channel.

Here we use the metric of eye-opening to quantify the influences of these phase fluctuations. The eye-opening metric is defined as the maximum opening of the eye-diagram (see, for example, the insets of Fig. 6.6), and it is closely related to the Q-factor and the bit-error-rate of the system [80, 81, 79, 73].

We consider three different models of the channelized devices. One is an ideal device with ideal spectral slicers whose transmission windows are of rectangular shape and with ideal slow-light media that have uniform group index and zero gain. The second is a semi-ideal device with realistic spectral slicers composed of cascaded half-band filters as described above and an ideal slow-light medium in each channel. The third is the most realistic model using realistic spectral slicers and SBS slow light. All three devices are set to provide one four-bit-long data packet delay.

For each phase noise level  $\delta\phi$ , we add a random phase  $\delta\phi(m)$  to the phase response of the  $m^{\text{th}}$  channel, and  $\delta\phi(m)$  is uniformly distributed in the interval of  $[-\sqrt{3}\delta\phi, \sqrt{3}\delta\phi]$ . Note that the standard deviation of such a phase noise distributions is equal to  $\delta\phi$ . We then calculate the eye-openings of the output signal through each channelized device with an input signal of a 128-bit pseudo-random data train. The calculation is performed 200 times for each phase noise level and for each device, and the average eye-openings for the three devices are plotted in Fig. 6.6 as functions of the phase noise level  $\delta\phi$ . One sees that as  $\delta\phi$  increases, the eye-opening gradually becomes smaller. If we require that the decrease of the eye-opening due to phase fluctuations should be less than 10%, one sees from Fig. 6.6 that the phase noise level  $\delta\phi$  should be less than approximately  $\pi/(5\sqrt{12})$  (i.e., the largest phase fluctuations

---

should be less than  $\lambda/10$ ) for all three models. Note that since such phase fluctuations are typically slowly-varying in time and independent on the fractional delay of the device, they can be compensated by e.g., using additional low-speed phase modulators.

## 6.4 Summary

In this chapter, we have proposed a new procedure for increasing the fractional delay of a slow-light system by utilizing spatially separated channels, each of which possesses a small group velocity over a narrow spectral frequency band. We have shown that by properly choosing the group index of each channel, one can achieve discretely tunable delays without the need to adjust the phase of each channel. Furthermore, we have shown that by using spatially separated channels, such a channelized device can exceed the fundamental limit of the delay-bandwidth product for a single channel slow-light device. We have proposed a practical design of such a device using spectral slicers and SBS slow light, and numerical simulation shows that discretely tunable packet delay can be achieved with negligible signal distortion.

# Chapter 7

## Slow Light Interferometry

### 7.1 Background

While many current applications of slow light focus on taking advantage of ultra-slow group velocities of optical pulses propagating inside the medium, the impact of the large dispersion inside a slow-light medium on the phase change of different frequency components of the optical fields has sometimes been overlooked.

Moreover, interferometers with high spectral sensitivity are becoming more and more desired in applications such as metrology [105], optical sensing [106], quantum information processing [107], biomedical engineering [108], etc. A number of schemes have been proposed to enhance the performance of interferometers, such as using PhC structures to minimize the size of an on-chip nonlinear electric-optic modulation devices [31] and EIT to increase the rotation sensitivity of a Sagnac interferometer [109].

In this chapter, we show how using slow light can benefit various types spectroscopic interferometers. We first derive the effect for both two-beam and multiple-beam interferometers, and use a proof-of-principle experiment to demonstrate the effect. We further analyze more practical situations when loss/gain of the slow-light medium is taken into account.

## 7.2 Two-beam interferometers

First, we consider the case of a Mach-Zehnder (M-Z) interferometer as a typical example of a two-beam interferometer. A slow-light medium of length  $L$  is placed in one of its arms (see Fig. 7.1), and the two arms are adjusted in such a way that the optical path difference between the arms is equal to the optical path length through the slow-light medium. The transmission of such an interferometer, when the slow-light medium is assumed transparent, is then given by

$$T = \frac{1}{2}(1 + \cos \Delta\phi), \quad (7.1)$$

where  $\Delta\phi$  is the phase difference between the two arms expressed by

$$\Delta\phi(\nu) = \frac{2\pi\nu}{c}n(\nu)L, \quad (7.2)$$

and where  $\nu$  is the frequency of the input field,  $c$  is the speed of light in vacuum, and  $n(\nu)$  is the refractive index of the slow-light medium.

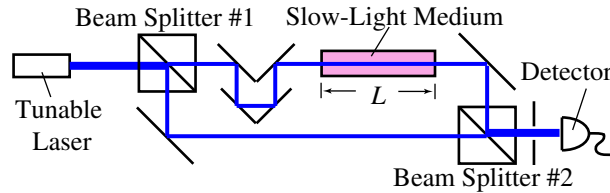


Figure 7.1: Schematic diagram of a Mach-Zehnder interferometer containing a slow-light medium in one arm.

For spectroscopic applications, a change in frequency  $\omega$  will produce a change in the phase difference term  $\Delta\phi$ , which will consequently lead to a change in the transmission intensity which enables the detection of the frequency shift. The spectral sensitivity of such an M-Z interferometer can be described by the rate at which the phase difference term  $\Delta\phi$  changes with frequency  $\nu$ . Taking the derivative of  $\Delta\phi$  with

respect to frequency  $\nu$ , one obtains the following expression:

$$\frac{d\Delta\phi}{d\nu} = \frac{d}{d\nu} \left( \frac{2\pi\nu n(\nu)L}{c} \right) = \frac{2\pi L}{c} \left( n + \nu \frac{dn}{d\nu} \right) = \frac{2\pi L n_g}{c}, \quad (7.3)$$

where  $n_g \equiv n + \nu dn/d\nu$  is the group index of the medium.

Thus, one sees that the spectral sensitivity is proportional to the group index  $n_g$  of the medium that is inside the interferometer. For common interferometers in which non-dispersive media (or media with small dispersion) are used,  $n_g$  equals (or approximates) the phase index  $n$ , and therefore the dependence of spectral sensitivity on dispersion can often be neglected. However, if a slow-light medium with very large group index  $n_g$  is used, the spectral sensitivity of such an interferometer can be greatly enhanced. Alternatively, for a given required spectral sensitivity, a shorter path length can be used for a slow-light medium. The resulting reduction in the device size could be important in applications where space is limited or where high stability is required.

If one defines the spectral resolution  $\delta\nu_{\min}$  of a M-Z interferometer to be the frequency difference between adjacent transmission peaks and valleys, one obtains the following quantified expression for the spectral resolution:

$$\delta\nu_{\min} = \frac{c}{2Ln_g}. \quad (7.4)$$

### 7.3 Multiple-beam interferometers

To investigate the performance of multiple-beam interferometers, we use as a typical example the Fabry-Perot (F-P) interferometer (see Fig. 7.2). For the case in which the F-P etalon is a slow-light medium of thickness  $L$ , the transmission of the interferometer as a function of the incidence angle  $\theta$  within the medium is given by

[110],

$$T(\theta) \approx \frac{T_s^2 T_L(\theta)}{(1 - R_s T_L(\theta))^2} \frac{1}{1 + \mathcal{F}^2 \sin^2 \Delta\phi(\theta)}, \quad (7.5)$$

where  $T_s$  and  $R_s$  are the transmissivity and reflectivity at the air-medium interface, respectively,  $T_L(\theta) \equiv \exp(-\alpha L / \cos \theta)$  is the transmissivity of a plane wave at incidence angle  $\theta$  through the medium,  $\Delta\phi = kL \cos \theta + \psi_0$  is the phase difference term,  $\alpha$  and  $k$  are the absorption coefficient and the wave number of the field inside the slow-light medium, respectively,  $\psi_0$  is the phase change of field due to reflection at the medium-air interface and  $\mathcal{F}$  is the finesse defined as

$$\mathcal{F} \equiv \frac{2R_s^{1/2} T_L(\theta)}{[1 - R_s T_L(\theta)]}. \quad (7.6)$$

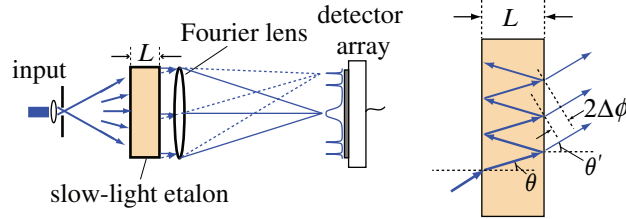


Figure 7.2: Left: Schematic diagram of a slow-light Fabry-Perot interferometer. Right: A close look at the multiple beam interference within the F-P etalon.

The angle between the center of the  $m^{\text{th}}$  fringe and the normal incidence direction is given by

$$\theta_m = \cos^{-1} \left( 1 - \frac{(M - m)\lambda}{2Ln} \right), \quad (7.7)$$

where  $M \approx 2Ln/\lambda$  is the order of the fringe at normal incidence.

The spectral sensitivity of the  $m^{\text{th}}$  order fringe is therefore given by

$$\begin{aligned}\frac{d\theta_m}{d\lambda} &= \frac{M - m}{2L \sin \theta_m} \left( \frac{1}{n} - \frac{\lambda dn}{n^2 d\lambda} \right) \\ &= \frac{(M - m)n_g}{2n^2 L \sin \theta_m}.\end{aligned}\quad (7.8)$$

For the case in which the finesse is high (i.e., small angular spread of the fringes), the angular spread [full width at half maximum (FWHM)] of the  $m^{\text{th}}$  order fringe is determined through the relation  $\delta\Delta\phi_m = 2/\mathcal{F}$  and is given by

$$\delta\theta_m = \frac{\lambda}{\pi L n \sin \theta_m \mathcal{F}}.\quad (7.9)$$

Thus, the spectral resolution of the  $m^{\text{th}}$  order fringe is given by

$$\delta\lambda_m = \frac{d\lambda}{d\theta} \delta\theta_m = \frac{2n\lambda}{(M - m)n_g \pi \mathcal{F}}.\quad (7.10)$$

For a F-P interferometer, one typically has the relation  $M \gg m$ . Thus, one can obtain the following expression for the spectral resolution of a F-P interferometer:

$$\delta\lambda_{\min} \approx \frac{2n\lambda}{M n_g \pi \mathcal{F}} = \frac{\lambda^2}{n_g L \pi \mathcal{F}}.\quad (7.11)$$

One sees that when gain or absorption is negligible, the spectral resolution of a slow-light F-P interferometer is inversely proportional to the group index of the etalon medium.

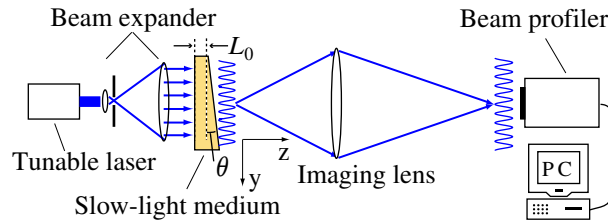


Figure 7.3: Schematic diagram of a wedged shear interferometer containing a slow-light medium.

A wedged shear interferometer is another example of a multiple-beam interferometer. As one sees in Fig. 7.3, a collimated beam is normally incident on a wedge plate. Due to the interference among the light waves bouncing back and forth between the two surfaces of the wedge plate, tilt fringes occur at the exit surface. When the wedge angle  $\theta$  is small (*i.e.*, the change of the thickness of the wedge plate across the incident area of the beam is much less than its average thickness  $L_0$ ), the intensity transmission as a function of lateral position  $y$  can be written as [110]

$$T(y) \approx \frac{T^2 T_L}{(1 - RT_L)^2} \frac{1}{1 + \mathcal{F} \sin^2 \Delta\phi(y)}, \quad (7.12)$$

where  $T$  and  $R$  are the transmissivity and reflectivity at the air-medium interface, respectively,  $T_L \equiv e^{-\alpha L_0}$  is the transmissivity through the medium,  $\Delta\phi = k(L_0 + \theta y) + \psi_0$  is the phase difference term,  $\alpha$  and  $k$  are the absorption coefficient and the wave number of the field inside the wedge plate, respectively,  $\psi_0$  is the phase change of field due to reflection at the medium-air interface and  $\mathcal{F}$  is the finesse defined as  $\mathcal{F} \equiv 4RT_L^2/(1 - RT_L)^2$ . The position of the  $m^{\text{th}}$ -order fringe peak is given by

$$y_m = \frac{(m\pi - \psi_0)c}{n\theta\omega} - \frac{L_0}{\theta}. \quad (7.13)$$

If the frequency of the incident field changes slightly, the fringe peak  $y_m$  will shift laterally. The rate of movement of the fringes as a function of frequency is given by,

$$\frac{dy_m}{d\omega} = -\frac{(m\pi - \psi_0)c}{\theta n^2 \omega^2} \left( n + \omega \frac{dn}{d\omega} \right) \approx -\frac{\bar{m}\pi c n_g}{\theta n^2 \omega^2}, \quad (7.14)$$

where  $\bar{m} \approx n\omega L_0/(\pi c)$  is the approximated order-number of the fringe peak (again, the small wedge angle condition of  $L_0 \gg \theta y_{\text{max}}$  is assumed). One can further normalize this fringe movement rate with the fringe period  $\Lambda = \pi c/n\omega\theta$  and obtain the following

normalized expression for the rate of fringe movement,

$$\frac{1}{\Lambda} \frac{dy_m}{d\omega} \approx -\frac{\bar{m}n_g}{n\omega} = -\frac{L_0n_g}{\pi c}, \quad (7.15)$$

or

$$\frac{1}{\Lambda} \frac{dy_m}{d\lambda} \approx \frac{\bar{m}n_g}{n\lambda} = \frac{2L_0n_g}{\lambda^2}. \quad (7.16)$$

One sees from Eqs. (7.15) and (7.16) that the movement rate is proportional to the group index  $n_g$  of the wedge plate. Note that the wedge interferometer is designed to monitor the frequency shift of the incident light by detecting the lateral movement of the fringes, and therefore its spectral sensitivity is directly proportional to the rate of the fringe movement, *i.e.*, proportional to  $n_g$ . Also note that other wavelength-dependent variables in Eq. (7.12), such as  $R$ ,  $T$  and  $\mathcal{F}$ , usually vary slowly within the wavelength range of interest, and therefore their impact on the spectral sensitivity can be ignored.

## 7.4 Experimental demonstration

A proof-of-principle experiment is carried out using a wedged shear interferometer. The slow-light medium used as the wedge plate in the interferometer is a  $\text{CdS}_{0.625}\text{Se}_{0.375}$  *c*-cut single crystal. The wedge plate is about 0.5 mm thick, and the angle between the two surfaces is about  $2.28^\circ$ . The absorption edge of this direct-bandgap semiconductor sample is measured to be 2.15 eV (*i.e.*, 578 nm) at room temperature. According to the Kramers-Kronig relation, the refractive index of this sample experiences a rapid change near the absorption edge and consequently gives a large group index in that region. The refractive index (for ordinary polarized light)

as a function of wavelength can be determined through the relation [111],

$$n_o(\omega) = \sqrt{1 + 2c_0^o [y_B - q \tan^{-1}(y_B/q)]}, \quad (7.17)$$

where  $c_0^o$  and  $y_B$  are coefficients whose numerical values are 0.996 and 3.324 for  $\text{CdS}_{0.625}\text{Se}_{0.375}$ , respectively,  $q \equiv \sqrt{1 - \hbar\omega/G}$ , and  $G = 2.15$  eV is the bandgap energy. Numerically, the values of the refractive index  $n$  and group index  $n_g$  at  $\lambda = 605$  nm are 2.64 and 3.87, respectively. As the wavelength is tuned towards the absorption edge), the group index increases much faster than the phase index. At  $\lambda = 587.5$  nm,  $n$  has a value of 2.69, almost the same as that at  $\lambda = 605$  nm, but the group index now is almost twice as large as  $n$  with a value of 4.80. Because the change of  $n$  and  $n_g$  as the wavelength decreases from 605 to 587.5 nm are very different, it enables us to distinguish experimentally whether the spectral sensitivity of the interferometer is dependent on  $n$  or  $n_g$ .

A Rhodamine 6G dye laser is used as the tunable source in the experiment. The fringe patterns on the exit surface of the wedge plate are imaged onto a CCD beam profiler using an imaging lens and are recorded digitally. Note that the imaging lens would not be required if the CCD were attached directly to the exit surface of the wedge plate. To determine the spectral sensitivity near each wavelength, the fringe patterns are recorded while the laser is detuned near this wavelength with a detuning step size of 0.01 nm for 21 steps. The relative peak positions are determined at each detuning step, and the fringe movement rate near this wavelength is calculated using linear fitting of the peak positions. The wavelengths at which the spectral sensitivity are measured are chosen from 605 nm to 587.5 nm with an decrement of 2.5 nm each time.

Figure 7.4 shows the relative rate of fringe movement (normalized by the fringe period) at different wavelengths. The spectral sensitivity of this interferometer increases from 10.7 periods/nm to 13.5 periods/nm (see squares in Fig. 7.4) as the wavelength changes from 605 nm to 587.5 nm. This increase agrees very well with the change

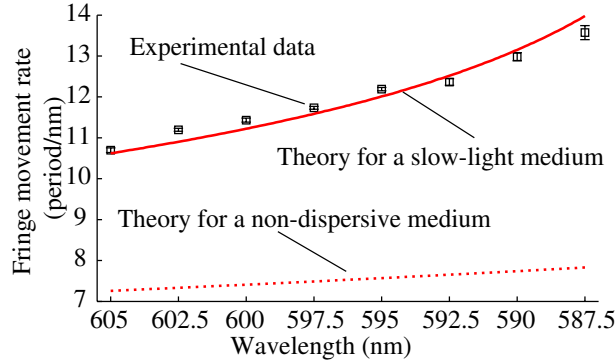


Figure 7.4: Relative rate of fringe movement as a function of wavelength. The squares are experimental data with standard deviation bars, the solid line is the theoretical prediction and the dashed line is the prediction if dispersion is neglected.

of group index of  $\text{CdS}_{0.625}\text{Se}_{0.375}$  as the wavelength is tuned towards the absorption edge. The solid line in Fig. 7.4 shows the theoretical predictions given by Eq. (7.16). One clearly sees that it matches very well with the experimental results. Also note that the rate of fringe movement (*i.e.*, the spectral sensitivity) of our interferometer with a slow-light medium is about twice as large as that of an interferometer with a non-dispersive medium with the same refractive index [*i.e.*, replacing  $n_g$  by the phase index  $n$  in Eq. (7.16); cf. the dotted line in Fig. 7.4]. Furthermore, the sensitivity for the non-dispersive interferometer changes only slightly as the wavelength changes from 605 nm to 587.5 nm.

## 7.5 Practical considerations

As shown in the previous two sections, the enhancement factor of the spectral resolution of a slow-light interferometer is equal to the group index of the slow-light medium in ideal cases when its group index is uniform and absorption/gain is negligible. However, in practice, a slow-light medium typically has associated gain or loss and has dispersion of the group index, which poses a further question: “What is the maximum achievable enhancement of the spectral performances of a slow-light

interferometer when realistic conditions of the medium is considered?”

We use two figures of merit to evaluate the spectral performance of an interferometer under practical considerations. The first one is the spectral resolution  $\delta\nu_{\min}$ , which describes the minimum frequency difference that the interferometer can resolve. This quantity also describes how sensitive an interferometer is to the change of the input frequency when it is used as a frequency monitor or sensor.

Secondly, the maximum usable spectral bandwidth of an interferometer, which we call it the working bandwidth, is an important quantity. Since the working bandwidth can be limited both by the dispersive properties of the slow-light medium and by the construction of the interferometer itself, we will use this figure of merit to evaluate specific slow-light processes in Chapter 9.

For a M-Z interferometer, the output transmission is given by

$$T = \frac{1}{4}(1 + e^{-\alpha L} + 2e^{-0.5\alpha L} \cos \Delta\phi), \quad (7.18)$$

where  $\alpha$  is the absorption coefficient of the medium. The spectral resolution is still given by Eq. (7.4), and one sees that the resolution is inversely proportional to the group index  $n_g$  as well as the length of the medium  $L$ . However, given a value of  $n_g$ , as the length  $L$  becomes larger, the associated gain or absorption mechanism of the slow-light medium will either amplify or attenuate the beam passing through the arm in which the slow-light medium is inserted. This will consequently change the fringe visibility at the output. The visibility of such a M-Z interferometer is given by

$$\mathcal{V} \equiv \frac{I_{\text{out,max}} - I_{\text{out,min}}}{I_{\text{out,max}} + I_{\text{out,min}}} = \frac{2e^{-0.5\alpha L}}{1 + e^{-\alpha L}}. \quad (7.19)$$

For a lossless M-Z interferometer, the value of the visibility  $\mathcal{V}$  is 1. The associated loss or gain of the slow-light medium will decrease the fringe visibility  $\mathcal{V}$ . For definiteness, we require that the loss through the slow-light medium be less than  $1/e$  (or gain less than a factor of  $e$ ), and consequently we obtain the following restriction

on the maximum length  $L$  of the medium,

$$|\alpha L| \leq 1. \quad (7.20)$$

Note that this requirement indicates that the visibility  $\mathcal{V}$  is always no less than 0.65. Substituting this requirement into Eq. (7.4), one obtains the following expression for the minimum spectral resolution for a M-Z interferometer with a lossy slow-light medium:

$$\delta\nu_{\min} = \left| \frac{c\alpha}{2n_g} \right|. \quad (7.21)$$

Such an expression for the spectral resolution is also applicable to other types of two-beam interferometers, such as a Michelson interferometer.

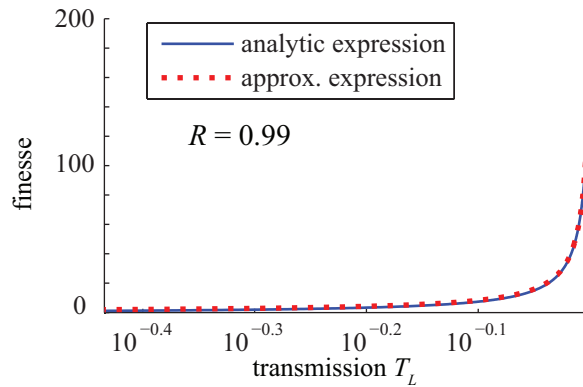


Figure 7.5: Finesse of a F-P interferometer as a function of single path transmission  $T_L$ . Here the reflectivity at the air-etalon interface is assumed to be 0.99.

To see more clearly how the absorption or gain of the slow-light medium influence the spectral resolution of multiple-beam interferometers, we recall that the expression of  $\mathcal{F}$  [cf. Eq. (7.6)] is dependent on the single pass transmission  $T_L$  of the light field. When the fractional loss or gain of the field after a single pass through the slow-light medium is small, one has  $T_L = \exp(-\alpha L) \approx 1 - \alpha L$ . In such cases and with the reflectivity at the air-etalon interface being high,  $R_s \approx 1$ , the finesse  $\mathcal{F}$  can be

approximated by (see also Fig. 7.5)

$$\mathcal{F} \approx \frac{2}{1 - R + \alpha L}. \quad (7.22)$$

And the expression of Eq. (7.11) for the resolution of a F-P interferometer can be approximated by

$$\begin{aligned} \delta\lambda_{\min} &\approx \frac{\lambda^2(1 + \alpha L - R_s)}{2n_g L \pi} \\ &= \left| \frac{\lambda^2(1 - R_s)}{2n_g L \pi} + \frac{\lambda^2 \alpha}{2n_g \pi} \right|, \end{aligned} \quad (7.23)$$

or in frequency units

$$\delta\nu_{\min} = \left| \frac{c(1 - R_s)}{2\pi n_g L} + \frac{c\alpha}{2\pi n_g} \right|. \quad (7.24)$$

One sees that the resolution is given by the sum of two terms. The first term is the expression for an ideal, lossless slow-light interferometer, and is inversely proportional to the group index  $n_g$ . The second term is proportional to the ratio between  $\alpha$  and  $n_g$ . In principle, the first term can be made to vanish when the reflectivity at the surface  $R_s$  approaches unity. In such cases, the overall spectral resolution will be primarily determined by the second term such that

$$\delta\nu_{\min} \approx \left| \frac{c\alpha}{2\pi n_g} \right|. \quad (7.25)$$

Figure 7.6 shows some theoretical calculations on the minimum spectral resolution of a F-P interferometer as a function of the etalon thickness  $L$ . We consider the etalon to be composed of four different materials, a non-slow-light medium with refractive index of unity, and three slow-light medium with the same group index  $n_g = 10$  and different values of the absorption coefficient. The reflectivity at the air-etalon interface is all assumed to be  $R_s = 0.99$ . The green dash-dotted line is the result of a non-slow-

light medium. The blue solid and the red dashed lines are the analytic [Eq. (7.11)] and approximated [Eq. (7.24)] expressions for the slow-light cases, respectively. One can see from the figure that when the single pass transmission through the etalon is high (loss being low), the spectral resolution of a slow-light F-P interferometer is indeed enhanced by a factor of  $n_g$  as compared to a conventional non-slow-light version. However, the absorption eventually limits the finest spectral resolution, and our approximated expression of Eq. (7.24) accurately reveals this limit.

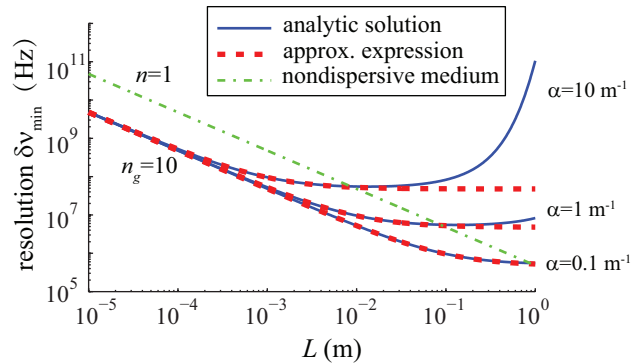


Figure 7.6: Resolution of a F-P interferometer as a function of the etalon thickness  $L$  for the etalon being composed of different materials.

Note that if the slow-light medium has gain such that the single-pass gain  $gL$  is comparable to the loss at the reflection  $1 - R_s$ , the two terms in Eq. (7.24) would become comparable to each other but with opposite signs. In this case, one can obtain very high spectral resolution as long as the gain is not saturated. Note that the expression of Eq. (7.24) is also valid for other types of multiple-beam interferometer, such as a wedged shear interferometer [11].

## 7.6 Summary

In this chapter, we have shown that the spectral sensitivity of an interferometer scales with the group index of the material within it and hence can be greatly enhanced by introducing a slow-light medium. The enhancement effect has been demonstrated

---

experimentally with a wedged shear interferometer based on a  $\text{CdS}_{0.625}\text{Se}_{0.375}$  semiconductor material. The change of the spectral sensitivity of the interferometer at different wavelengths agrees well with the change of the group index at these wavelengths. In our proof-of-principle setup, the spectral sensitivity is enhanced by approximately a factor of 2, which is limited by the value of  $n_g$  of  $\text{CdS}_{0.625}\text{Se}_{0.375}$ . We have further analyzed the influence of associated gain/loss of slow-light medium on the minimum achievable spectral resolution of different types of interferometers, and we see that for both two-beam and multiple-beam interferometers, the limiting resolution scales with  $c\alpha/n_g$ .

# Chapter 8

## Slow Light Fourier-Transform Interferometry

### 8.1 Conventional Fourier transform interferometry

Fourier-transform (FT) interferometry [112] is a powerful technique that has intrinsically high signal-to-noise ratio (SNR) and can have high resolving power. These properties have led to its many applications in biomedical engineering, metrology [113], astronomy, etc. A conventional FT interferometer [see Fig. 8.1(a)] is typically comprised of a fixed arm and a moving arm, both of which contain non-dispersive media (typically air) with refractive index  $n$ . The length of the moving arm can be changed to achieve a variable optical delay time (ODT)  $\tau = nL/c$ , where  $L$  is the length difference between the two arms, and  $c$  is the speed of light in vacuum. The output intensity is given by

$$(2I_{\text{out}} - I_{\text{in}}) = \int_0^{\infty} I_{\text{in}}(\nu) \cos(2\pi n\nu L/c) d\nu. \quad (8.1)$$

Assuming

$$I_{\text{in}}(\nu) = I_{\text{in}}(-\nu), \quad (8.2)$$

One has

$$\begin{aligned} (I_{\text{out}} - 0.5I_{\text{in}}) &= \int_0^{\infty} I_{\text{in}}(\nu) e^{i2\pi\nu L/c} d\nu + \int_0^{\infty} I_{\text{in}}(-\nu) e^{-i2\pi\nu L/c} d\nu \\ &= \int_{-\infty}^{\infty} I_{\text{in}}(\nu) e^{i2\pi\nu L/c} d\nu. \end{aligned} \quad (8.3)$$

The above expression shows that the output intensity is the Fourier transform of the intensity spectrum of the laser source. For simplicity, we define the normalized output intensity as

$$I'_{\text{out}} \equiv I_{\text{out}} - 0.5I_{\text{in}}. \quad (8.4)$$

By measuring the output intensity while adjusting the optical path difference  $L$  from zero to a large number  $L_{\text{max}}$ , the spectrum of the source can be obtained as

$$I_{\text{in}}(\nu) = \int_{-\infty}^{\infty} I'_{\text{out}}(l) e^{-i2\pi\nu l/c} dl, \quad (8.5)$$

where

$$I'_{\text{out}}(l) = I'_{\text{out}}(-l). \quad (8.6)$$

To resolve the spectrum of an input optical field with center frequency  $\nu$ ,  $\tau$  needs to be tuned from zero to a maximum value  $\tau_{\text{max}}$  with a step size comparable to  $1/\nu$ . The spectral resolution is given by  $\delta\nu_{\text{min}} = 1/(2\tau_{\text{max}})$  [112]. To achieve a high spectral resolution, one needs a large device size [typically with the order of  $c/(2n\delta\nu_{\text{min}})$ ] and a large number of data acquisition steps [determined by  $\nu/(2\delta\nu_{\text{min}})$ ]

for each measurement. Thus, the resolution of a conventional FT interferometer is typically of the order of 1 nm, which needs approximately 1000 measuring steps.

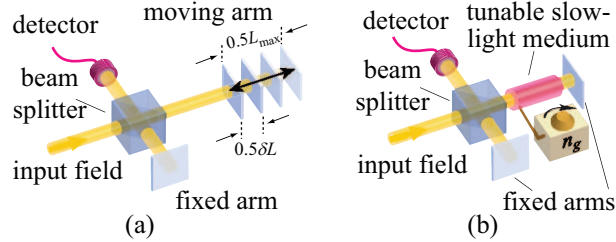


Figure 8.1: Schematic diagrams of (a) a conventional FT interferometer with one moving arm and one fixed arm; and (b) a FT interferometer with a tunable slow-light medium in one of the two fixed arms.

## 8.2 A slow-light Fourier transform interferometer

In this chapter, we propose and demonstrate a new type of FT interferometer that uses a continuously tunable slow-light medium to realize a tunable group delay between the two arms [see Fig. 8.1(b)]. We first develop the theory for the ideal case in which the slow-light medium has a uniform group index  $n_g$  (defined by  $n_g \equiv n + \nu dn/d\nu$ ) and thus no group velocity dispersion over the frequency range of interest. The frequency dependence of the refractive index of such an ideal tunable slow-light medium in the vicinity of a reference frequency  $\nu_0$  is given by

$$n(\nu) \approx n(\nu_0) + \frac{n'_g \nu'}{\nu_0}, \quad (8.7)$$

where  $\nu' \equiv \nu - \nu_0$  is the frequency detuning and  $n'_g \equiv n_g - n$  is the relative group index. We assume that for such a medium  $n'_g$  can be varied continuously, for example by changing the number density of an atomic vapor, from zero to a maximum value  $n'_{g,\max}$ . Note that  $\nu_0$  is a reference frequency chosen such that  $n(\nu_0)$  remains constant as  $n'_g$  is tuned. We consider a Mach-Zehnder (M-Z) interferometer with such a tunable slow-light medium of length  $L$  in one arm and a non-dispersive reference medium of length

$L_2$  and refractive index  $n_2$  in the other arm. For simplicity, we let  $I(\nu) = |E(\nu)|^2$ . When the input field has multiple frequency components, the output intensity at each of the two ports of such a M-Z interferometer (see Fig. 8.2) is given by

$$I_{\text{out},\pm} = \frac{1}{4} \int I_{\text{in}}(\nu) |e^{ik[n(\nu_0) + \frac{n'_g \nu'}{\nu_0}]L} \pm e^{ikn_2 L_2}|^2 d\nu, \quad (8.8)$$

where  $k = 2\pi\nu/c$  is the wave number at frequency  $\nu$  in vacuum. Note that, in practice, both arms also contain other non-dispersive media such as beam splitters and air. However, the optical path lengths contributed from these media are assumed to be balanced between the two arms, and therefore are not shown in Eq. (8.8). When the two arms are balanced such that  $n_2 L_2 = n(\nu_0)L$ , one can rewrite Eq. (8.8) as follows:

$$\begin{aligned} I_{\text{out},\pm} &= \frac{1}{4} \int I_{\text{in}}(\nu) |e^{ik \frac{n'_g \nu'}{\nu_0} L} \pm 1|^2 d\nu \\ &= \frac{1}{2} I_{\text{in}} \pm \frac{1}{2} \int I_{\text{in}}(\nu) \cos k \frac{n'_g \nu'}{\nu_0} L d\nu. \end{aligned} \quad (8.9)$$

By subtracting the two outputs, and approximating  $k$  by  $k_0$ , one obtains the following relation

$$I'_{\text{out}} \equiv I_{\text{out},+} - I_{\text{out},-} \approx \int I_{\text{in}}(\nu) \cos 2\pi \frac{n'_g \nu'}{c} L d\nu, \quad (8.10)$$

where  $I'_{\text{out}}$  is the modified output that can be directly measured by using a balanced homodyne detection method [114]. Note that, for a pulse with center frequency near  $\nu_0$ , the relative delay between the two arms of the interferometer is given by

$$\tau_g = \frac{n_g L}{c} - \frac{n_2 L_2}{c} = [n_g - n(\nu_0)] \frac{L}{c} = \frac{n'_g L}{c}. \quad (8.11)$$

We assume that the incident field contains only frequency components that are larger than  $\nu_0$ , as is in the case of the experiment shown below. In this way, one can

obtain the following inverse Fourier transform relation:

$$\begin{aligned} I'_{\text{out}}(\tau_g) &= \int_{-\infty}^{\infty} I_{\text{in}}(\nu_0 + \nu') \cos 2\pi\nu'\tau_g d\nu' \\ &= \Re\left\{ \int_{-\infty}^{\infty} I_{\text{in}}(\nu_0 + \nu') e^{i2\pi\nu'\tau_g} d\nu' \right\}, \end{aligned} \quad (8.12)$$

where  $\Re\{\}$  denotes the real part. Thus, one can retrieve the input spectrum by applying a Fourier transform to the output intensity scan as a function of  $\tau_g$  and taking only the result with positive detuning  $\nu' > 0$ . Note that expression (8.12) is similar to that of a conventional FT interferometer (e.g., Eq. (11.4) in Ref. [112]), except that in the present case the Fourier conjugate pair is the detuning  $\nu'$  and the group delay  $\tau_g$  instead of the absolute frequency  $\nu$  and the ODT  $\tau$ .

In the ideal case in which the slow-light medium is lossless, the spectral resolution  $\delta\nu$  of such a slow-light FT interferometer is limited by the largest achievable group delay  $\tau_{g,\text{max}}$  to

$$\delta\nu = 1/(2\tau_{g,\text{max}}) = c/(2n'_{g,\text{max}}L). \quad (8.13)$$

Since  $n'_{g,\text{max}}$  can be very large when a suitable slow-light medium is used, the spectral resolution of the slow-light FT interferometer can be enhanced by the significant factor of  $n'_{g,\text{max}}$  with respect to that of a conventional setup. Alternatively, for a specified spectral resolution  $\delta\nu$ , the device size can be decreased by a factor of  $n'_{g,\text{max}}$ .

The total spectral range of such a FT interferometer is given by

$$\Delta\nu = c/(2\delta n'_g L), \quad (8.14)$$

where  $\delta n'_g$  is the step size of the change in  $n'_g$ . Note that our slow-light FT interferometer does not require any moving arms, which is advantageous in certain situations in which vibration and translation errors of a moving arm could introduce measurement errors and decrease the SNR.

The theory of Eqs. (8.7) – (8.12) can be extended to the more general case in which the slow-light medium has an arbitrary frequency dependence of the refractive index near  $\nu_0$  in the form of  $n(\nu) = n(\nu_0) + (n'_g/\nu_0)f(\nu')$  where  $f(\nu')$  describes the normalized dispersion function near  $\nu_0$ . In such a case, one can replace  $\nu'$  by  $f(\nu')$  in Eqs. (8.8) – (8.12) and obtain the following inverse FT relation:

$$I'_{\text{out}}(\tau_g(\nu_0)) = \Re\left\{\int_{-\infty}^{\infty} I_{\text{in}}(\nu' + \nu_0)e^{i2\pi f(\nu')\tau_g(\nu_0)}d\nu'\right\}, \quad (8.15)$$

where  $\tau_g(\nu_0)$  is the group delay of a pulse centered at  $\nu_0$ . Note that  $\tau_g(\nu_0)$  can be determined from the group delay of a pulse centered at any known frequency  $\nu + \nu'$  through the relation  $\tau_g(\nu_0) = n'_g(\nu_0)\tau_g(\nu_0 + \nu')/n'_g(\nu_0 + \nu')$ . The Fourier transform of  $I'_{\text{out}}(\tau_g(\nu_0))$  gives first the spectrum  $I_{\text{in}}$  as a function of  $f(\nu')$ . When each value of  $f(\nu')$  corresponds to a unique value of  $\nu_0 + \nu'$  within the spectral range of interest, one can then map out the input spectrum  $I_{\text{in}}(\nu_0 + \nu')$  from  $I_{\text{in}}(f)$ . The spectral resolution near frequency  $\nu_0 + \nu'$  is given by  $\delta\nu(\nu_0 + \nu') = \max\{c/[2n'_{g,\text{max}}(\nu_0 + \nu')L], c\alpha(\nu_0 + \nu')/[2n'_g(\nu_0 + \nu')]\}$ , where  $n'_{g,\text{max}}(\nu_0 + \nu')$  and  $\alpha(\nu_0 + \nu')$  are the maximum relative group index and the absorption coefficient of the medium at frequency  $\nu_0 + \nu'$ , respectively.

### 8.3 Experimental demonstration

We have constructed a slow-light FT interferometer possessing a M-Z geometry to demonstrate the properties of our proposed scheme (see Fig. 8.2). A 10-cm-long rubidium vapor cell is used as the slow-light medium. The tunability of the group index is realized by controlling the temperature and thereby the atomic number density of the cell. A tunable continuous wave (CW) diode laser operating at approximately 780 nm with a linewidth of approximately 100 kHz is used as the primary source. An acousto-optic modulator (AOM) is used to produce a second CW field whose frequency is 80 MHz lower than the primary field. The two fields are combined and used as the input field. Balanced homodyne detection is used to measure the output inten-

sity  $I'_{\text{out}}$ . For monitoring purposes, a part of the primary laser is directed through a Mach-Zehnder modulator (MZM), which is driven by an arbitrary waveform generator (AWG) to produce a pulse train with 4 nano-second pulse duration. By measuring the group delay  $\tau_g$  experienced by such pulses of known frequency in propagating through the vapor cell, the value of  $n'_g$  at the primary frequency is obtained.

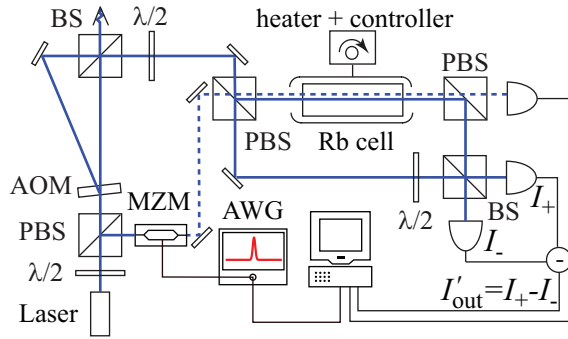


Figure 8.2: Experimental setup of the FT interferometer using a rubidium vapor cell as the slow-light medium.

The refractive index of a rubidium vapor near the  $D_2$  transition lines can be approximated as [115, 116],

$$n(\nu) = 1 - \frac{A}{2} \sum_{j=1}^4 \frac{g_j}{\nu - \nu_j + i\gamma}, \quad (8.16)$$

where the four terms in the summation correspond to the four major hyperfine transitions of the rubidium  $D_2$  lines [see Fig. 8.3],  $g_j$  and  $\nu_j$  are the relative peak strength and the frequency center of the  $j^{\text{th}}$  resonance, respectively,  $\gamma \approx 6$  MHz is the homogeneously broadened linewidth of the Rb resonances, and  $A$  is a coefficient determined by the atomic number density and the dipole transition moments. The frequency spacing between the centers of neighboring resonances from low to high frequencies are 1.22 GHz, 3.035 GHz, and 2.58 GHz, respectively. The natural abundances of  $^{87}\text{Rb}$  and  $^{85}\text{Rb}$  are 28% and 72% respectively; therefore the relative peak strengths among the four resonances are  $g_1 : g_2 : g_3 : g_4 = (5/8) \times 0.28 : (7/12) \times 0.72 : (5/12) \times 0.72 :$

$(3/8) \times 0.28$ . The transmission as a function of detuning  $\nu'$  through the vapor cell at a temperature of approximately 100 °C is plotted in Fig. 8.3(a). The thick and thin curves show the measured data and the theory of Eq. (8.16) (with  $A = 1.14 \times 10^6$  Hz), respectively. The reference frequency  $\nu_0$  is chosen between the resonances of the  $^{85}\text{Rb}$   $F = 2 \rightarrow F'$  and  $^{87}\text{Rb}$   $F = 1 \rightarrow F'$  transitions so that  $n(\nu_0) = 1$  according to Eq. (8.16). Note that the theory curve for the absorption, which is based on the use of Eq. (8.16), fits the data very well in the wings of the lines but not near the resonances themselves. This is because Eq. (8.16) ignores the influence of Doppler broadening and the resulting Gaussian lineshape. Since Gaussian lineshapes decay much more rapidly in the wings than do Lorentzian lineshapes, Eq. (8.16) accurately describes the atomic response at the frequencies (the gray region in Fig. 8.3) at which our measurements were performed. The calculated corresponding refractive index  $n$ , and group index  $n_g$  are plotted in Fig. 8.3(b) and 8.3(c), respectively, as functions of  $\nu'$ .

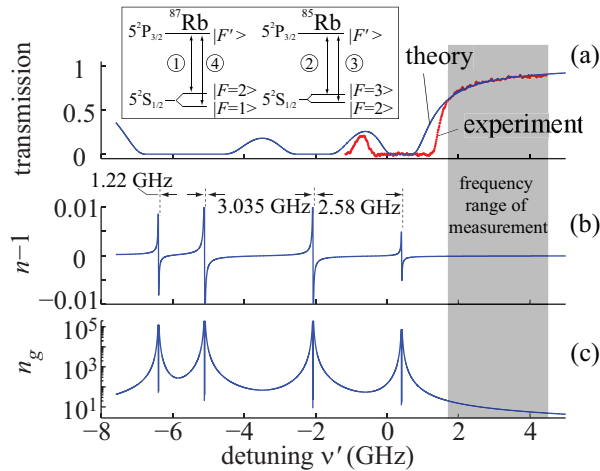


Figure 8.3: (a) Transmission; (b) refractive index  $n$ ; and (c) group index  $n_g$  of the 10-cm-long rubidium vapor cell at the temperature of approximately 100 °C as functions of detuning  $\nu'$ . The thick curve is the measured transmission, and the thin curves are the fitted theory using Eq. (8.16). The inset shows the energy levels of the  $^{87}\text{Rb}$  and  $^{85}\text{Rb}$  D<sub>2</sub> transitions; and the gray region is the frequency region over which the spectral measurement are performed.

The primary frequency of the input field is chosen to be approximately 1.79 GHz higher than the reference frequency  $\nu_0$  so that the dispersion model of Eq. (8.16) can be used. At room temperature, the vapor pressure is practically zero so that  $n'_g \approx 0$ . As the temperature rises, the atomic number density increases [*i.e.*,  $A$  in Eq. (8.16) increases] and therefore  $n'_g$  increases. In the experiment, the pulse delay  $\tau_g$  and the output intensity  $I'_{\text{out}}$  are measured simultaneously as the vapor cell is heated from room temperature to approximately 120 °C in a time of approximately 1 minute. The maximum group delay is approximately 40 nanoseconds, which corresponds to  $n'_{g,\text{max}} \approx 120$  at the primary frequency.

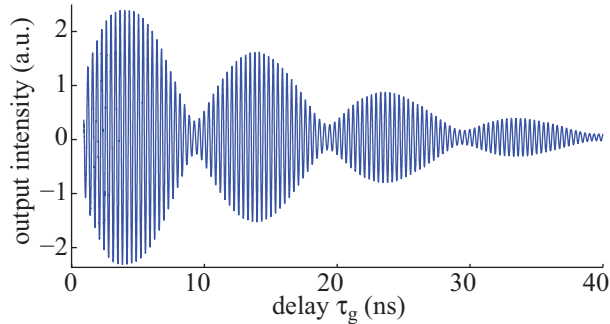


Figure 8.4: Output intensity of the slow-light FT interferometer as a function of the group delay  $\tau_g$  for an input field of two sharp spectral lines separated by 80 MHz.

Figure 8.4 shows the experimental data for the output intensity  $I'_{\text{out}}$  as a function of the group delay  $\tau_g$  at the primary frequency. The interference pattern clearly shows the beating between the two closely spaced spectral lines. Note that the envelope of  $I'_{\text{out}}$  is not at a maximum when  $n'_g$  approaches zero, which is probably because the phase difference (*e.g.*, due to the coatings on the surfaces of various optical elements in our setup) between the two arms is not the same for different frequency components of the input field even when  $n'_g = 0$ .

The input spectrum is retrieved through the FT relation of Eq. (8.15) and the mapping process described above. The result is plotted as the solid line in Fig. 8.5. The dotted line is the actual input spectrum, and the dashed line shows the simulated result which is obtained from the calculated  $I'_{\text{out}}$  using the actual input spectrum, the

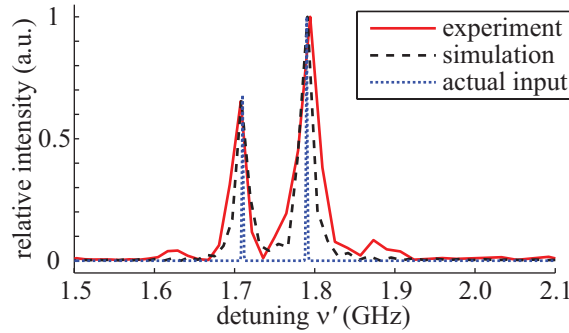


Figure 8.5: Retrieved spectrum of the input field using experimental data (solid line) and simulated data (dashed line) and the actual spectrum of the input field (dotted line). The resolution of a conventional FT interferometer of the same size would be approximately 100 times worse.

rubidium model of Eq. (8.16) and the assumption of a balanced, noise-free interferometer. One sees that the experimental result accurately resolves the position and the profile of the input field. The spectral resolution demonstrated in the experiment is approximately 15 MHz. This value agrees with the simulation result, and is limited by the absorption of our slow-light medium. In contrast, a conventional setup with an OPD between the two arms limited to 10 cm could produce a spectral resolution no better than approximately 1.5 GHz. Thus, through use of slow-light methods, we have enhanced the resolution by a factor approximately equal to the maximum group index (100) of our slow-light medium.

## 8.4 Practical considerations

In practice, however, a variable slow-light medium typically has associated frequency-dependent loss, which is usually linearly proportional to the reduced group index  $n'_g$ . In this case, the output of the interferometer can be re-written in the following form:

$$\begin{aligned}
 & I_{\text{out}}(\tau_g) \\
 &= \Re\left\{ \int_{-\infty}^{\infty} I_{\text{in}}(\nu_0 + \nu') e^{-\frac{\alpha(\nu_0 + \nu')}{2} L} e^{i2\pi\nu'\tau_g} d\nu' \right\}. \quad (8.17)
 \end{aligned}$$

For an input field containing only an infinitely narrow spectral line centered at  $\nu_1$ , the output as a function of the group delay is given by

$$I'_{\text{out}} = \Re\{e^{-0.5\alpha(\nu_1)L} e^{i2\pi(\nu_1 - \nu_0)\tau_g}\}. \quad (8.18)$$

To retrieve the input spectrum, one needs to take the Fourier transform of the output  $I_{\text{out}}(\tau_g)$  as follows,

$$\begin{aligned} I_{\text{in}} &= \text{FT}\{\Re\{e^{-0.5\alpha(\nu_1)L} e^{i2\pi(\nu_1 - \nu_0)\tau_g}\}\} \\ &= \int_{-\infty}^{\infty} e^{-\frac{\alpha(\nu_1)L}{2\tau_g}|\tau_g|} e^{-i2\pi\tau_g(\nu' - \nu_1 + \nu_0)} d\tau_g \\ &= \int_{-\infty}^{\infty} e^{-\sigma|\tau_g|} e^{-i2\pi\tau_g\nu''} d\tau_g, \end{aligned} \quad (8.19)$$

where  $\sigma \equiv \alpha(\nu')L/(2\tau_g)$  and  $\nu'' \equiv \nu' - \nu_1 + \nu_0$  is the frequency detuning from  $\nu'$ . Note that  $\sigma$  is independent of  $\tau_g$ . Consequently, one can calculate the above Fourier transform as follows:

$$\begin{aligned} I_{\text{in}}(\nu'') &= \int_0^{\infty} e^{-\sigma\tau_g} e^{-i2\pi\tau_g\nu''} d\tau_g + \int_{-\infty}^0 e^{\sigma\tau_g} e^{-i2\pi\tau_g\nu''} d\tau_g \\ &= \frac{1}{\sigma + i2\pi\nu''} + \frac{1}{\sigma - i2\pi\nu''} \\ &= \frac{C}{\nu''^2 + \gamma_{\text{eff}}^2}, \end{aligned} \quad (8.20)$$

where  $C$  is a constant independent of  $\nu''$ , and  $\gamma_{\text{eff}}$  is the effective linewidth given by

$$\gamma_{\text{eff}} = \frac{\sigma}{2\pi} = \frac{c\alpha}{4\pi n'_g}. \quad (8.21)$$

One sees that the retrieved spectrum is a Lorentzian-shaped line with a FWHM linewidth of

$$\delta\nu_2 = 2\gamma_{\text{eff}} = c\alpha/2\pi n'_g. \quad (8.22)$$

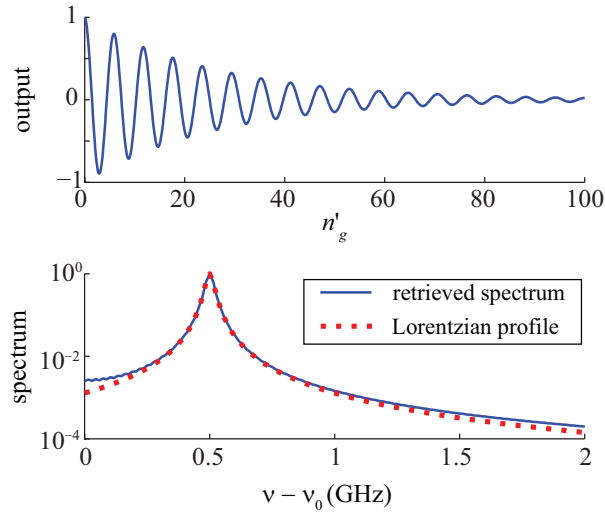


Figure 8.6: (a) Simulated output of a slow-light FTI as the reduced group index  $n'_g$  increases when the input field only contains a single frequency. (b) The retrieved spectrum as compared to a Lorentzian-shaped spectral line.

As a numerical example, we simulate the output [see Fig. 8.6(a)] of an ideal SL-FTI when the input field has only one frequency which is 0.5 GHz away from the reference frequency  $\nu_0$ . The ratio of  $\alpha/n'_g$  is assumed to be 0.75, and the length of the variable slow-light medium is 10 cm. One sees that due to the existence of absorption, the fringe visibility dies off as the reduced group index increases. When one takes the Fourier transform, the retrieved spectrum, as plotted in blue solid curve in Fig. 8.6(b), is indeed well approximated by a Lorentzian shaped spectral line with linewidth given by Eq. 8.22 [see the red dotted line in Fig. 8.6(b)].

When both the maximum group index and absorption are considered, the overall spectral resolution of the slow-light FT interferometer is given by

$$\delta\nu_{\min} = \max \left[ \frac{c}{2n'_{g,\max}L}, \frac{c\alpha}{2\pi n'_g} \right]. \quad (8.23)$$

Since the first term can always be made arbitrarily small by increasing the medium length  $L$ , and the spectral resolution of a practical slow-light FTI will be primarily limited by the second contribution.

## 8.5 Summary

In this chapter, we have proposed and experimentally demonstrated a new type of Fourier-transform interferometer that has two fixed arms with a tunable slow-light medium in one arm. We have shown that in such a FT interferometer the spectrum of the input field and the modified output intensity as a function of group delay form a Fourier transform pair. Since the maximum group delay through a slow-light medium can be very large under proper conditions, such a slow-light FT interferometer can provide very high spectral resolution. Moreover, a slow-light FT interferometer might be expected to outperform a conventional FT interferometer by eliminating instabilities and positioning errors associated with the moving arm of a conventional device. Furthermore, we show that when absorption is present, the intrinsic spectral line retrieved has a Lorentzian shape, and the linewidth again scales with the ratio between the absorption coefficient and the reduced group index.

# Chapter 9

## Evaluating Slow Light Processes for Interferometry Applications

### 9.1 Introduction

There are many physical processes that have been proposed and demonstrated to realize slow and fast light. While each slow light processes has its own beauty in physics and implementation, one way or the other, some of them maybe more suitable for interferometry applications than others. To have a better understanding on which slow-light processes have more potentials in interferometry, we here investigate the performance of slow-light interferometers when three specific slow-light mechanisms are used.

As derived in the pervious two chapters, the spectral resolutions of the three types of interferometers (two-beam, multiple-beam and Fourier-transform interferometers) we have considered are limited by  $|c\alpha/(2n_g)|$ ,  $|c\alpha/(2\pi n_g)|$  and  $|c\alpha/(2\pi n'_g)|$ , respectively. For definiteness, we define the characteristic spectral resolution as

$$\delta\nu_c \equiv |c\alpha/(2\pi n'_g)| \tag{9.1}$$

for the remaining of this chapter. Note also that we assume that the group index  $n_g$  is much larger than the refractive index  $n$  such that  $n'_g \approx n_g$ .

Besides the minimum spectral resolution, another figure of merit we consider here is the working bandwidth as compared to the characteristic spectral resolution. This thought is quantified by working finesse, which is defined by

$$\mathcal{F}_w = \Delta\nu_w / \delta\nu_c, \quad (9.2)$$

where the working bandwidth  $\Delta\nu_w$  of a slow-light medium is calculated such that the spectral resolution within the working bandwidth does not vary by more than a factor of 2.

## 9.2 Single isolated Lorentzian gain line

Single-resonance gain features are commonly used to achieve slow light [12, 117, 35, 73] because of the rapid change of the refractive index in the vicinity of the resonance center. For example, the gain coefficient, refractive index, and reduced group index of an unsaturated Lorentzian gain line [12, 117] as functions of the frequency detuning  $\nu' = \nu - \nu_0$  from the resonance center  $\nu_0$  are given by

$$g(\nu') = g_0 \frac{\gamma^2}{\nu'^2 + \gamma^2}, \quad (9.3)$$

$$n(\nu') = n(0) + \frac{g_0}{2k_0} \frac{\gamma\nu'}{\nu'^2 + \gamma^2}, \quad (9.4)$$

and

$$n'_g(\nu') = \frac{cg_0\gamma}{4\pi} \frac{-\nu'^2 + \gamma^2}{(\nu'^2 + \gamma^2)^2}, \quad (9.5)$$

where  $g_0$  and  $k_0$  are the gain coefficient and the wave number at the center frequency  $\nu_0$ , respectively,  $\gamma$  is the half width at half maximum (HWHM) linewidth, and  $n(0)$  is the background refractive index at the resonance center.

From the above expressions, one can obtain the ratio between  $g$  and  $n'_g$  as

$$\frac{g(\nu')}{n'_g(\nu')} = -\frac{4\pi\gamma\nu'^2 + \gamma^2}{c\nu'^2 - \gamma^2}. \quad (9.6)$$

The characteristic spectral resolution at the resonance center is then given by

$$\delta\nu_c(\nu' = 0) = \left| \frac{c\alpha(0)}{2\pi n'_g(0)} \right| = 2\gamma. \quad (9.7)$$

One sees from Eq. (9.6) that the spectral resolution is frequency dependent and deteriorates as the frequency moves away from the resonance center. The working bandwidth is determined through the relation

$$\delta\nu_c(\nu' = 0.5\Delta\nu_w) = 2\delta\nu_c(\nu' = 0), \quad (9.8)$$

and is given by

$$\Delta\nu_w = \frac{2\gamma}{\sqrt{3}}. \quad (9.9)$$

Consequently, the working finesse  $\mathcal{F}_w$  is given by

$$\mathcal{F}_w = \frac{1}{\sqrt{3}}. \quad (9.10)$$

We see that the working finesse is independent of the linewidth of the resonance, and is less than unity, which is due to the rapid change in spectral resolution [see Fig. 9.1(b)] caused by the rapid variation of the group index and the gain coefficient in the vicinity of a Lorentzian resonance center [see Fig. 9.1(a)]. This result indicates that such a slow-light medium may be useful for detecting the frequency shift of an

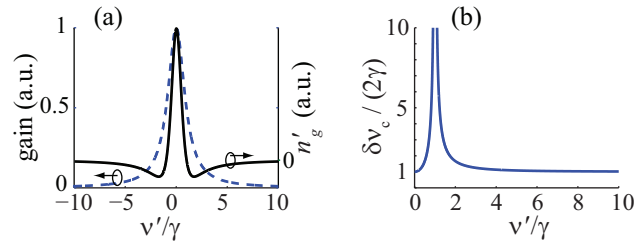


Figure 9.1: (a) The reduced group index  $n'_g$  and gain coefficient  $g$ , and (b) the characteristic spectral resolution  $\delta\nu_c$  as functions of the normalized frequency detuning from the resonance center for a single Lorentzian gain line medium.

input field, but is not suitable for constructing a spectrometer to measure a broad spectrum because of its very limited working finesse near the resonance center.

Two techniques can be used to overcome this limitation. One is to use a broadened gain feature with a flattened top (e.g., using multiple gain lines [35, 73]) instead of a single Lorentzian gain line to increase the working bandwidth. The other is to put the gain feature on a broadband absorption background to make the medium transparent near the resonance center. Using the latter technique, one can make the absolute magnitude of the gain coefficient be very small near the resonance center, and consequently achieve high spectral resolution because the characteristic spectral resolution will no longer be restricted by Eq. (9.7).

Note however that the ratio given by Eq. (9.6) does not change much in the wings of the resonance when the frequency detuning  $\nu'$  is much larger than  $\gamma$  [also see Fig. 9.1(b)]. This result indicates that such a slow-light medium can be used in a spectrometer if the working frequency range is chosen to be in the wing of the resonance center [118], so long as the strength of the resonance is great enough to provide a large group index in the wing region.

### 9.3 Separated double absorption lines

It has recently been shown that the use of the transparency window between two separated absorption features is a very effective technique to realize slow light [10,

15]. Here we consider the case in which two identical, Lorentzian resonance lines of HWHM linewidth  $\gamma$  and separated by  $2\Delta$  are used. The absorption coefficient, relative refractive index  $n'(\nu') \equiv n(\nu') - n(\nu' = 0)$  and reduced group index as functions of the detuning  $\nu' = \nu - \nu_0$  from the center frequency  $\nu_0$  half way between the two resonance lines are given by

$$\alpha(\nu') = \alpha_0 \left[ \frac{\gamma^2}{(\nu' - \Delta)^2 + \gamma^2} + \frac{\gamma^2}{(\nu' + \Delta)^2 + \gamma^2} \right], \quad (9.11)$$

$$n'(\nu') = -\frac{\alpha_0}{2k_0} \left\{ \frac{\gamma(\nu' - \Delta)}{(\nu' - \Delta)^2 + \gamma^2} + \frac{\gamma(\nu' + \Delta)}{(\nu' + \Delta)^2 + \gamma^2} \right\}, \quad (9.12)$$

and

$$n'_g(\nu') = \frac{c\alpha_0\gamma}{4\pi} \left[ \frac{(\nu' - \Delta)^2 - \gamma^2}{[(\nu' - \Delta)^2 + \gamma^2]^2} + \frac{(\nu' + \Delta)^2 - \gamma^2}{[(\nu' + \Delta)^2 + \gamma^2]^2} \right]. \quad (9.13)$$

Thus, the ratio between  $n'_g$  and  $\alpha$  is given by

$$\frac{n'_g(\nu')}{\alpha(\nu')} = \frac{c}{4\pi} \left[ \frac{1}{\gamma} + \frac{2\gamma}{\nu'^2 + \gamma^2 + \Delta^2} - \frac{2\gamma}{(\nu' - \Delta)^2 + \gamma^2} - \frac{2\gamma}{(\nu' + \Delta)^2 + \gamma^2} \right]. \quad (9.14)$$

The characteristic spectral resolution near the center frequency  $\nu_0$  is thus given by

$$\delta\nu_c(\nu' = 0) = \left| \frac{c\alpha(0)}{2\pi n'_g(0)} \right| = 2\gamma \frac{\Delta^2 + \gamma^2}{\Delta^2 - \gamma^2}. \quad (9.15)$$

For the case in which the half separation  $\Delta$  between the two resonance centers is much larger than the resonance linewidth  $\gamma$ ,  $\delta\nu_c$  is approximately equal to  $2\gamma$  [see Fig. 9.2(b)].

Note that in the cases in which  $\Delta \gg \gamma$ , the working bandwidth is approximately

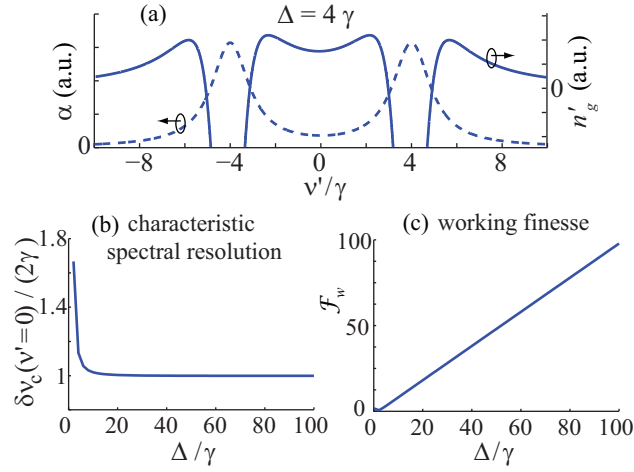


Figure 9.2: (a) The reduced group index and absorption coefficient as functions of detuning for a double-absorption-line medium with  $\Delta = 4\gamma$ ; (b) the characteristic spectral resolution at  $\nu' = 0$ , and (c) the working finesse as functions of the normalized half separation between the two resonance centers.

equal to the separation between the two resonances  $2\Delta$ . Therefore, the working finesse in this case can be approximated by

$$\mathcal{F}_w \approx \frac{\Delta}{\gamma}. \quad (9.16)$$

As long as the strength of the resonances is great enough, the working finesse can be very high, linearly proportional to the separation between the two resonance centers [see Fig. 9.2(c)]. Note that we require that the reduced group index within the entire working bandwidth to be of the same sign (either positive or negative for slow or fast light cases, respectively). Thus, the working finesse becomes zero when  $\Delta = \gamma$ . For  $\Delta < \gamma$  the double resonance medium becomes a single absorption line medium, and therefore the working finesse is also reduced to that of a single-gain-line medium.

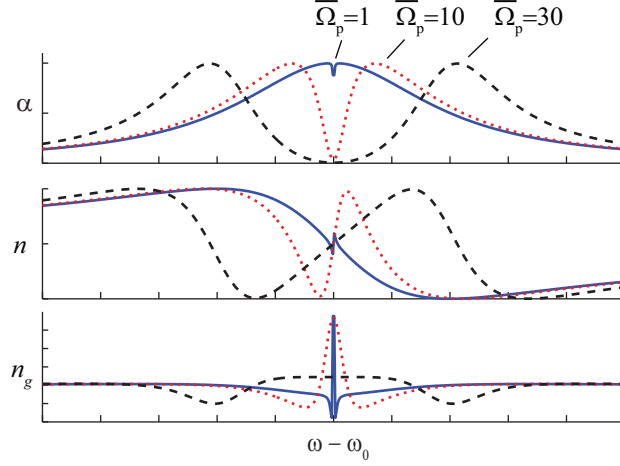


Figure 9.3: Absorption coefficient, refractive index, and group index as functions of frequency detuning for a EIT medium with three different pump field strength.

## 9.4 Electromagnetically induced transparency

Electromagnetically induced transparency (EIT) is a quantum optical process that can achieve very large group indices of the order of millions [119, 2, 120]. In the case of zero pump detuning [see Fig. 9.4(a)], the analytic expression for the complex refractive index of a  $\Lambda$ -type EIT medium as a function of the frequency detuning  $\nu' = \nu - \nu_0$  from the EIT resonance center  $\nu_0$  is given by [4]

$$\tilde{n}(\nu') = \frac{\alpha_0}{2k_0} \frac{\gamma_{ba}(\nu' + i\gamma_{ca})}{|\Omega_p|^2 - (\nu' + i\gamma_{ba})(\nu' + i\gamma_{ca})}, \quad (9.17)$$

where  $\alpha_0$  and  $k_0$  are the background absorption coefficient (when the pump field is absent) and the wave number at the EIT center frequency, respectively,  $\gamma_{ca}$  and  $\gamma_{ba}$  are the dephasing rates of the transitions from levels  $|c\rangle$  to  $|a\rangle$  and from  $|b\rangle$  to  $|a\rangle$ , respectively, and  $\Omega_p$  is the pump Rabi frequency.

For a typical EIT medium with  $\gamma_{ba} \gg \gamma_{ca}$ , one can expand Eq. (9.17) in a Taylor series, keep terms up to the third order, and obtain the following approximate expressions for the absorption coefficient and the refractive index near the EIT resonance

center (within the transparency window),

$$\alpha(\nu') \approx \frac{\alpha_0}{1 + |\bar{\Omega}_p|^2} \left( 1 + \frac{\nu'^2}{A^2} \right), \quad (9.18)$$

and

$$n(\nu') \approx 1 + \frac{\alpha_0 c}{4\pi\nu_0} \frac{B\nu'}{1 + |\bar{\Omega}_p|^2} \left( 1 + \frac{\nu'^2}{C^2} \right), \quad (9.19)$$

where  $\bar{\Omega}_p \equiv \Omega_p / \sqrt{\gamma_{ba}\gamma_{ca}}$  is the normalized pump Rabi frequency,  $\bar{\gamma} \equiv \gamma_{ba}/\gamma_{ca}$ ,  $A^2 \equiv \gamma_{ba}^2 (1 + |\bar{\Omega}_p|^2)^2 / [(\bar{\gamma}^2 + 2\bar{\gamma})|\bar{\Omega}_p|^2 - 1]$ ,  $B \equiv (|\bar{\Omega}_p|^2 - \bar{\gamma}^{-1}) / [\gamma_{ca}(1 + |\bar{\Omega}_p|^2)]$ , and  $C^2 \equiv \gamma_{ca}\gamma_{ba}(|\bar{\Omega}_p|^2 + 1)^2(|\bar{\Omega}_p|^2 - \bar{\gamma}^{-1}) / [|\bar{\Omega}_p|^4 - (3\bar{\gamma}^{-1} + \bar{\gamma} + 2)|\bar{\Omega}_p|^2 + \bar{\gamma}^{-2}]$ .

The reduced group index  $n'_g$  is then given by

$$n'_g(\nu') = \frac{\alpha_0 c}{4\pi} \frac{B}{|\bar{\Omega}_p|^2 + 1} \left( 1 + \frac{3\nu'^2}{C^2} \right). \quad (9.20)$$

Using these expressions, one can obtain the following result for the ratio of  $\alpha$  to  $n'_g$ ,

$$\frac{\alpha(\nu')}{n'_g(\nu')} = \frac{4\pi C^2}{cBA^2} \frac{(A^2 + \nu'^2)}{(C^2 + 3\nu'^2)}. \quad (9.21)$$

At the EIT resonance center (i.e.,  $\nu' = 0$ ), one obtains the following expression for the characteristic spectral resolution,

$$\delta\nu_c(\nu' = 0) = \left| \frac{c\alpha(0)}{2\pi n'_g(0)} \right| = \frac{2}{B} = 2\gamma_{ca} \frac{|\bar{\Omega}_p|^2 + 1}{|\bar{\Omega}_p|^2 - \bar{\gamma}^{-1}}. \quad (9.22)$$

As the pump Rabi frequency increases, the characteristic spectral resolution approaches its minimum value  $\delta\nu_c \rightarrow 2\gamma_{ca}$ . Note that this resolution is much finer than the intrinsic linewidth  $\gamma_{ba}$  associated with the transition from level  $|b\rangle$  to  $|a\rangle$ .

One sees from Eq. (9.21) that the resolution  $\delta\nu_c$  will deteriorate as the signal frequency is detuned away from the EIT resonance center. The working bandwidth  $\Delta\nu_w$  is determined through the relation that the resolution at the boundary  $\delta\nu_c(\nu' =$

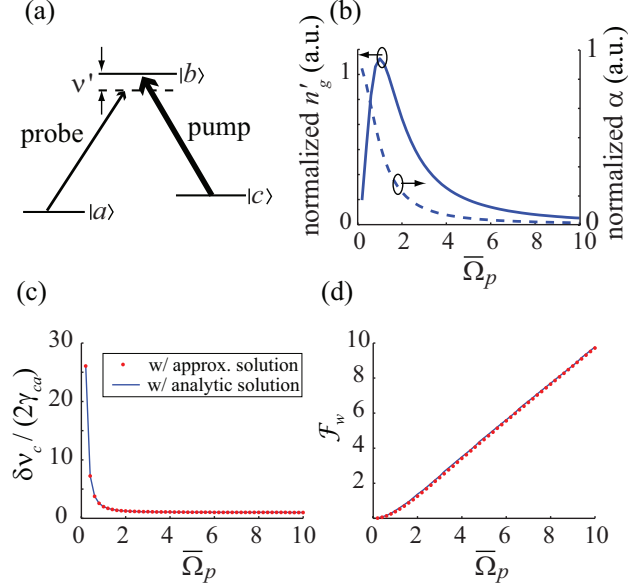


Figure 9.4: (a) Energy level diagram of a  $\Lambda$ -type EIT system; (b) the reduced group index and absorption coefficient at the center frequency, (c) the characteristic spectral resolution at  $\nu' = 0$ , and (d) the working finesse, all plotted as functions of the normalized pump Rabi frequency for an EIT medium with  $\bar{\gamma} = 100$ . The dots are results using the approximate expression of Eqs. (9.22) and (9.25), and the solid lines are results based on the analytical expression of Eq. (9.17).

$0.5\Delta\nu_w$ ) of the working bandwidth is twice as large as the resolution at the EIT resonance center, i.e.,

$$\frac{A^2 + (0.5\Delta\nu_w)^2}{C^2 + 3(0.5\Delta\nu_w)^2} = 2\frac{A^2}{C^2}. \quad (9.23)$$

For a large pump Rabi frequency, one obtains the following expression for the working bandwidth,

$$\Delta\nu_w = 2\sqrt{\frac{A^2C^2}{C^2 - 6A^2}} \approx \frac{2\gamma_{ba}|\bar{\Omega}_p|}{\sqrt{\bar{\gamma}(\bar{\gamma} - 5)}}. \quad (9.24)$$

Since  $\gamma_{ba} \gg \gamma_{ca}$  (i.e.,  $\bar{\gamma} \gg 1$ ), the working bandwidth can be further approximated as

$\Delta\nu_w \approx 2\gamma_{ca}|\bar{\Omega}_p|$ . Consequently, the working finesse  $\mathcal{F}_w$  is given by

$$\mathcal{F}_w = B\sqrt{\frac{A^2C^2}{C^2 - 6A^2}} = \frac{|\bar{\Omega}_p|^2 + 1}{|\bar{\Omega}_p|^2 - \bar{\gamma}^{-1}}\sqrt{\frac{\bar{\gamma}}{\bar{\gamma} - 5}}|\bar{\Omega}_p|. \quad (9.25)$$

For a large pump Rabi frequency and a large  $\bar{\gamma}$ , the working finesse becomes  $\mathcal{F}_w \approx |\bar{\Omega}_p|$ , i.e., the normalized pump Rabi frequency.

Figure 9.4(b) shows the normalized reduced group index and the absorption coefficient at the EIT resonance center as the normalized pump Rabi frequency  $\bar{\Omega}_p$  increases. One sees that the group index reaches its maximum when  $\bar{\Omega}_p$  is approximately equal to 1. For  $\bar{\Omega}_p > 1$ , the value of the group index decreases due to the power broadening of the transparency window. Meanwhile, the absorption coefficient decreases monotonically as  $\bar{\Omega}_p$  increases. As a result, the characteristic spectral resolution  $\delta\nu_c$  rapidly becomes smaller first as  $\bar{\Omega}_p$  increases from zero, and gradually approaches to its theoretical limit  $2\gamma_{ca}$  for  $\bar{\Omega}_p > 2$  [see Fig. 9.4(c)]. On the other hand, one sees from Fig. 9.4(d) that the working finesse is approximately equal to the value of the normalized Rabi frequency  $\bar{\Omega}_p$  as predicted in Eq. (9.25).

Note also that the characteristic resolution of an EIT medium is limited by the decay rate between the two ground state, which is typically much less than the linewidth of the transition between the excited state and one ground state. Therefore, an slow-light interferometer based on EIT can potentially achieve higher spectral resolution as compared to an interferometer based on double-absorption lines.

## 9.5 Summary

The spectral performance of slow light interferometers using three specific slow light processes has been evaluated in terms of the characteristic spectral resolution and the working finesse. It has been shown that while the characteristic resolution is typically limited by the linewidth of a resonance-induced slow-light medium, it can be much smaller if a broadband absorption or gain can be added on the narrow gain or

---

absorption feature to make the slow-light medium more transparent over the spectral region for which the group index is large. Moreover, it has been shown that there is no fundamental upper limit for the working finesse that a slow light interferometer can achieve.

Of the three types of slow light processes studied here, EIT media have the potential to achieve the finest spectral resolution, because the linewidth is limited by the decay rate between two ground states, which is typically much less than that of a transition between an excited state and a ground state. However, double-absorption-line media have more applicability because it can be more easily implemented and controlled [118]. These analyses provide guidelines for how to choose appropriate slow-light techniques for interferometry applications to meet specific demands on the spectral performance.

# Chapter 10

## On-Chip Slow-Light Interferometers

We have shown in previous chapters that slow light can greatly enhance the spectral resolution of spectroscopic interferometers. On the other hand, slow light can also greatly reduce the size of a spectroscopic interferometer while maintaining the same resolution. Following this thought, we here study the possibility of building on-chip spectrometers using slow light that have unprecedented spectral performances.

### 10.1 Design of the geometry of an on-chip spectrometer

There are many different geometries that can be applied to construct an on-chip spectrometer, such as Mach-Zehnder interferometer, etched diffraction grating, arrayed waveguide grating, and so on.

The M-Z interferometer has been studied in detail in Chapter 7. For an on-chip M-Z interferometer, the slow-light medium can be replaced with a slow-light waveguide. To better understand other types of spectrometers, we start by analyzing a planar diffraction grating. The grating equation, which links the incident and the

$m^{\text{th}}$ -order diffracted field, is

$$n_{\text{inc}} \sin \theta_{\text{inc}} + n_{\text{diff}} \sin \theta_{\text{diff},m} = \frac{m\lambda}{\Lambda}, \quad (10.1)$$

where  $n_{\text{inc}}$  and  $n_{\text{diff}}$  are the refractive indices of the materials in the incident and diffracted regions, respectively,  $\theta_{\text{inc}}$  is the incidence angle,  $\theta_{\text{diff},m}$  is the  $m^{\text{th}}$ -order diffraction angle,  $\lambda$  is the vacuum wavelength of the incident field, and  $\Lambda$  is the grating period. In non-slow-light cases, in which neither  $n_{\text{inc}}$  nor  $n_{\text{diff}}$  is wavelength dependent, the angular dispersion can be calculated as follows:

$$\frac{d\theta_{\text{diff},m}}{d\lambda} = \frac{m}{\Lambda n_{\text{diff}} \cos \theta_{\text{diff},m}}. \quad (10.2)$$

This result shows that one would prefer a high diffraction order and a small grating period to obtain a high angular dispersion. This usually leads to high diffraction angles, which then has practical issues of effective length of the grating and aberrations for concave gratings.

Next, we consider an ideal slow-light medium with the refractive index of the form of

$$n(\nu) = n_0 + \frac{n'_g}{\nu_0}(\nu - \nu_0), \quad (10.3)$$

where  $n'_g = n_g - n$  is the reduced group index of the medium in the vicinity of the center frequency  $\nu_0$ , and where  $n_g = n + \nu \, dn/d\nu$  is the group index of the medium. If both the incident and diffracted regions are composed of such a slow-light medium (i.e.,  $n_{\text{inc}} = n_{\text{diff}} = n(\nu)$ ), the angular dispersion of the grating near  $\nu_0$  is given instead by

$$\frac{d\theta_{\text{diff},m}}{d\lambda} = \frac{m}{\Lambda n \cos \theta_{\text{diff},m}} - \frac{m\lambda}{\Lambda n^2 \cos \theta_{\text{diff},m}} \frac{dn}{d\lambda} = \frac{mn_g}{\Lambda n^2 \cos \theta_{\text{diff},m}}. \quad (10.4)$$

Similarly, by using a slow-light waveguide slab in the incident and diffracted beams

of an integrated grating (e.g., an etched diffraction grating), one can enhance the angular dispersion of the grating and consequently enhance the spectral resolution by a factor of  $n_g/n$ , the ratio between the group index and the effective mode index of the slow-light slab.

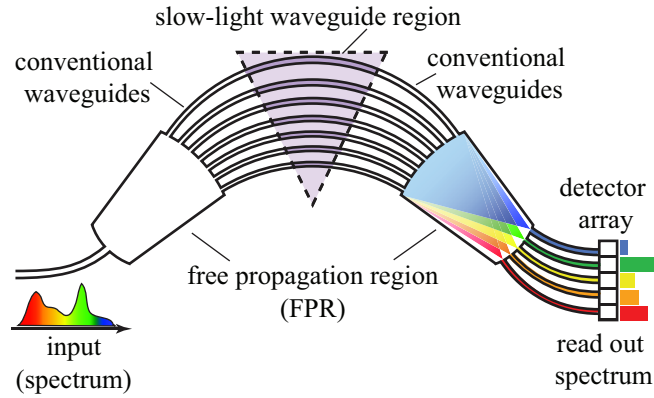


Figure 10.1: Schematic diagram of a slow-light arrayed waveguide grating spectrometer.

Another important type of integrated grating devices is arrayed waveguide gratings (AWGs; [121]). AWGs are commonly used as wavelength multiplexers and demultiplexers in wavelength division multiplexing (WDM) telecommunications systems. A conventional AWG is typically comprised of three parts as shown in Fig. 10.1. The input signal field first propagates through a free-propagation region (FPR) to expand its beam width. The field is then coupled into a series of waveguides. The waveguides are designed such that the lengths of neighboring waveguides differ by a fixed amount  $\Delta l = m\lambda_0/n_{\text{eff}}$  where  $\lambda_0$  is the designed central (vacuum) wavelength of the device, and  $n_{\text{eff}}$  is the effective refractive index (i.e., mode index) of the waveguides. The output ports of these waveguides are spaced periodically (with a period of  $\Lambda$ ) at the entrance to a second FPR, and the fields exiting from the waveguides array will constructively interfere and focus at the other side of the second FPR. The diffraction equation of such an AWG is given by

$$n_{\text{wg}}\Delta l + n_{\text{FPR}}\Lambda(\sin \theta_{\text{inc}} + \sin \theta_{\text{diff},m}) = m\lambda, \quad (10.5)$$

where  $n_{\text{wg}}$  and  $n_{\text{FPR}}$  are the effective mode indices for the waveguides and the FPR, respectively.

When the dispersion of  $n_{\text{wg}}$  and  $n_{\text{FPR}}$  are negligible, the angular dispersion of such an AWG is given by

$$\frac{d\theta_{\text{diff},m}}{d\lambda} = \frac{m}{n_{\text{eff}}\Lambda \cos \theta_{\text{diff},m}} \quad (10.6)$$

Since  $m$  is independent of  $\Lambda$  in this case, an AWG can, in principle, have arbitrarily large angular dispersion. However, a large angular dispersion indicates that  $\Delta l$  must be large, which leads to an increased footprint of the device.

If the dispersion of  $n_{\text{wg}}$  and  $n_{\text{FPR}}$  are taken into account, the diffraction equation becomes modified as follows:

$$\begin{aligned} \frac{d\theta_{\text{diff},m}}{d\lambda} &= \frac{mn_{g,\text{FPR}}}{n_{\text{FPR}}^2\Lambda \cos \theta_{\text{diff},m}} - \frac{\Delta l}{n_{\text{FPR}}\Lambda \cos \theta_{\text{diff},m}} \frac{dn_{\text{wg}}}{d\lambda} \\ &\quad + \frac{n_{\text{wg}}\Delta l}{n_{\text{FPR}}^2\Lambda \cos \theta_{\text{diff},m}} \frac{dn_{\text{FPR}}}{d\lambda} \\ &= \frac{mn_{g,\text{FPR}}}{n_{\text{FPR}}^2\Lambda \cos \theta_{\text{diff},m}} \\ &\quad + \frac{n_{\text{wg}}\Delta l}{n_{\text{FPR}}\lambda\Lambda \cos \theta_{\text{diff},m}} \left( \frac{n'_{g,\text{wg}}}{n_{\text{wg}}} - \frac{n'_{g,\text{FPR}}}{n_{\text{FPR}}} \right). \end{aligned} \quad (10.7)$$

Here, we consider the case in which the waveguide has large modal dispersion (i.e., large dispersion on the effective index), but the dispersion of the FPR is negligible. In such a case, the angular dispersion becomes

$$\frac{d\theta_{\text{diff},m}}{d\lambda} = \frac{m}{n_{\text{FPR}}\Lambda \cos \theta_{\text{diff},m}} + \frac{n'_{g,\text{wg}}\Delta l}{n_{\text{FPR}}\lambda\Lambda \cos \theta_{\text{diff},m}}. \quad (10.8)$$

One sees that in such a case, the angular dispersion of the AWG comes from two contributions, one containing the non-slow-light contribution and one containing the

slow-light contribution from the waveguide.

In practice, an AWG can work in a configuration such that the diffraction angle for the central wavelength is zero degree to minimize the influence of aberrations, etc. In such cases, the diffraction order  $m$  of the AWG depends primarily on the waveguide increment  $\Delta l$  such that  $m \approx n_{\text{wg}}\Delta l/\lambda$ , and the angular dispersion is given by

$$\frac{d\theta_{\text{diff},m}}{d\lambda} \approx \frac{n_{g,\text{wg}}\Delta l}{n_{\text{FPR}}\lambda\Lambda \cos \theta_{\text{diff},m}} \quad (10.9)$$

$$= \frac{n_{g,\text{wg}}m}{n_{\text{FPR}}n_{\text{wg}}\Lambda \cos \theta_{\text{diff},m}}. \quad (10.10)$$

One sees that by using a slow-light waveguide array, the angular dispersion of an AWG can be enhanced by a factor of  $n_{g,\text{wg}}/n_{\text{wg}}$ , and therefore one can enhance the spectral resolution by the same factor.

Here, we demonstrate our design using a numerical example based on the Silicon-On-Insulator (SOI) platform. We assume the center wavelength to be  $1.55 \mu\text{m}$ . The refractive indices for Si and  $\text{SiO}_2$  are  $n_{\text{Si}} = 3.476$  and  $n_{\text{SiO}_2} = 1.5$ , respectively. We assume the spacing between the output of neighboring waveguides to be  $3 \mu\text{m}$ , the diffraction angle  $\theta_{\text{diff}} = 0^\circ$  at the center wavelength, and the length of the FPR to be  $R_{\text{FPR}}1.5 \text{ mm}$ .

Figure.10.2 shows the calculated transverse dispersion at the focal plane of the output FPR of a slow-light AWG as a function of the group index  $n_{g,\text{wg}}$  of the waveguides. Here the transverse dispersion  $dx/d\lambda = R_{\text{FSR}}d\theta_{\text{diff},m}/d\lambda$ , where the angular dispersion  $d\theta_{\text{diff},m}/d\lambda$  is given by Eq. 10.9. When the  $n_{g,\text{wg}} = 3$  and  $\Delta_L = 10 \mu\text{m}$ , the transverse dispersion is approximately  $2.8 \mu\text{m}/\text{nm}$ , which is just adequate to separate two wavelength differing  $1 \text{ nm}$  as two spectral channels in a wavelength division multiplexing system. When  $n_{g,\text{wg}} = 100$ , the transverse dispersion increases to  $94 \mu\text{m}/\text{nm}$ . If we let  $\Delta L = 40 \mu\text{m}$ , the transverse dispersion is  $375 \mu\text{m}/\text{nm}$ . If the distance between neighboring output waveguide is  $3 \mu\text{m}$ , this indicates a spectral

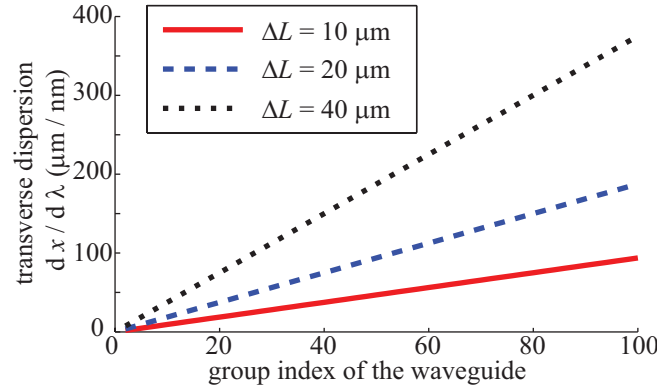


Figure 10.2: Linear transverse dispersion at the focal plane of the output FPR as a function of the group index of the waveguide of a slow-light AWG with  $\Delta L = 10$ , 20 and 40  $\mu\text{m}$ , respectively.

resolution of 1 GHz. Note that the group index in photonic crystal waveguides can be as large as 230 [20, 122] or even more, which indicates the possibility of a further increase in the spectral resolution.

## 10.2 Photonic crystal waveguide

One essential component of the slow-light on-chip spectrometer described in the previous section is a group of the slow-light waveguides, which are the waveguides within the triangle areas in Fig. 10.1. In this section, we show that a slab photonic crystal (PhC) line-defect waveguides can be used as slow-light waveguides to be incorporated into the on-chip slow-light spectrometer. A slab photonic crystal is a two-dimensional periodic structure fabricated on a planar waveguide slab, such as a silicon-on-insulator (SOI) platform. Figure 10.3 shows an example of a PhC single-line-defect waveguide on SOI platform. The light is confined by index contrast in  $z$  direction, and by the photonic crystal structures in the  $x - y$  plane.

One approach to achieve slow light in a PhC waveguide is to design the bandgap of the PhC waveguide such that the working frequency is very close to a band edge. One advantageous property of photonic crystal waveguides is scalability, i.e., the frequency

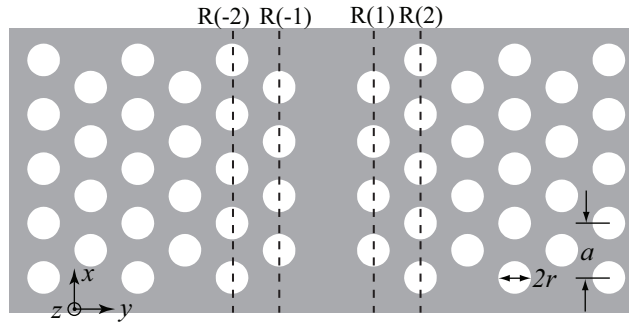


Figure 10.3: Two-dimensional schematic diagram of a slab photonic crystal single line defect (W1) waveguide with lattice constant  $a$  and hole radius  $r$ .

properties of the bandgaps and of the dispersion relations are all proportional to the lattice constant (periodicity) of the PhC structure, provided that the refractive index is dispersionless.

As an example, we study one particular design of a PhC W1 waveguide [123]. Here the term “W1” indicates that one row of holes is missing as a line defect. The geometric parameters of such a W1 PhC waveguide are the lattice constant  $a$  and air-hole radius  $r$ . We here choose  $a = 405$  nm and  $r = 0.3a$ . We calculated the dispersion diagram of such a PhC W1 waveguide using a planar wave expansion analysis package (MIT MPB [124]). The dispersion relation of the fundamental guided band in the second Brillouin zone is plotted in Fig. 10.4(a). Here  $\lambda_{\text{vac}}$  is the optical wavelength in vacuum.

The corresponding effective mode index  $n_{\text{eff}}$  and reduced group index  $n'_g \equiv \omega(dn_{\text{eff}}/d\omega)$  are plotted in Fig. 10.4(b) and (c), respectively. One sees that this guided mode cuts off at approximately  $1.57$   $\mu\text{m}$ , and therefore the group index increases rapidly as the wavelength approaches the band edge. For example,  $n'_g = 100$  and  $200$  for  $\lambda = 1.5640$   $\mu\text{m}$  and  $1.5647$   $\mu\text{m}$ , respectively.

While working near the band edge, as in the above design, can achieve a large group index, the group index is highly frequency dependent. In practical applications, one would prefer a slow-light waveguide to have a large working bandwidth over which the group index is constant.

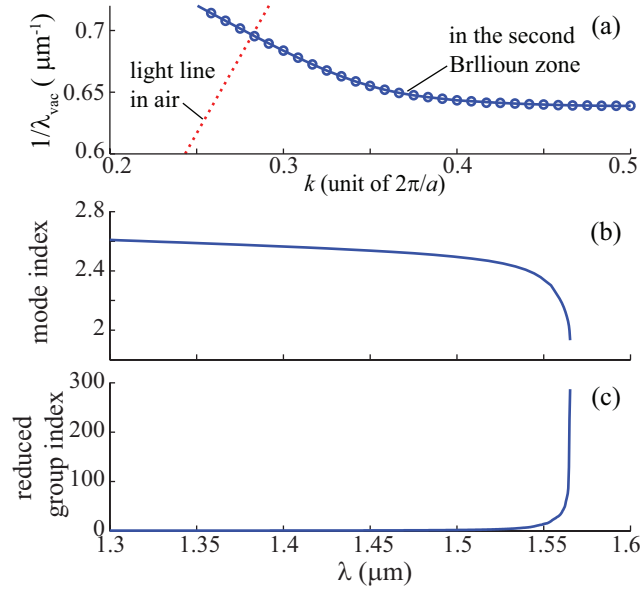


Figure 10.4: (a) Dispersion relations of the fundamental guided Bloch modes of a PhC W1 waveguide; corresponding effective mode index (b) and reduced group index  $n'_g$  (c) as functions of wavelength for such a waveguide structure.

The need for a flat-band slow-light waveguide leads to the need to optimize the PhC waveguide geometry, such as changing the shape, size and position of some holes [125], and longitudinal period of a few rows near the line defect.

### 10.3 Design of a flat-band slow-light photonic crystal waveguide

To design a flat-band slow-light photonic crystal waveguide, we start from taking a more careful look at the parameters in our 2-D model. The PhC structure is fabricated on a SOI platform, in which the silicon (Si) core layer is 275–285 nm thick for the samples we have and the silica (SiO<sub>2</sub>) substrate is 3  $\mu\text{m}$ . The frequency-dependent refractive index of Si in the near IR wavelength regime can be approximated using

the following Sellmeier model [126]:

$$n^2(\lambda) = \epsilon_1 + \frac{A}{\lambda^2} + \frac{B\lambda_1^2}{\lambda^2 - \lambda_1^2}, \quad (10.11)$$

where  $\epsilon_1 = 11.6858$ ,  $A = 0.939816$ ,  $B = 8.10461 \times 10^{-3}$ , and  $\lambda_1 = 1.1071 \mu\text{m}$ , respectively. Here  $\lambda$  is in the unit of  $\mu\text{m}$ . The frequency-dependent refractive index of  $\text{SiO}_2$  can be approximated using the following Sellmeier model:

$$n^2(\omega) = 1 + \sum_{j=1}^3 \frac{B_j \omega_j^2}{\omega_j^2 - \omega^2}, \quad (10.12)$$

where  $B_1 = 0.6961663$ ,  $B_2 = 0.4079426$ ,  $B_3 = 0.8974794$ ,  $\lambda_1 = 0.0684043 \mu\text{m}$ ,  $\lambda_2 = 0.1162414 \mu\text{m}$ , and  $\lambda_3 = 9.896161 \mu\text{m}$ , respectively.  $\omega_j$  can be determined through the relation  $\lambda_j = 2\pi c/\omega_j$ .

At the wavelength of 1550 nm, the above models give refractive indices of 3.474 and 1.444 for Si and  $\text{SiO}_2$ , respectively.

In reality, the modes supported by either the waveguides or the photonic crystal structures are of three dimensional (3-D), and a 3-D simulation and analysis seem to be most appropriate. However, 3-D analysis typically requires a large amount of computation time and resource. Thus, we here use two-dimensional simulations for most of the analysis and design.

To convert the 3-D problem into a 2-D model, we use the effective index treatment. The effective mode index of a slab SOI waveguide is calculated and used as the effective index of the waveguide region in the 2-D model. The calculation results are shown in Fig. 10.5 as a function of the thickness of the Si layer. In our case the Si slab is 280 nm thick, therefore the effective index for TE and TM like modes are 2.998 and 2.4193, respectively. Here, a TE like mode is defined such that the main  $E$  field component is in the  $y$  direction, and a TM like mode is defined such that the main  $H$  field component is in the  $y$  direction. Hereafter, we will use these two values as the

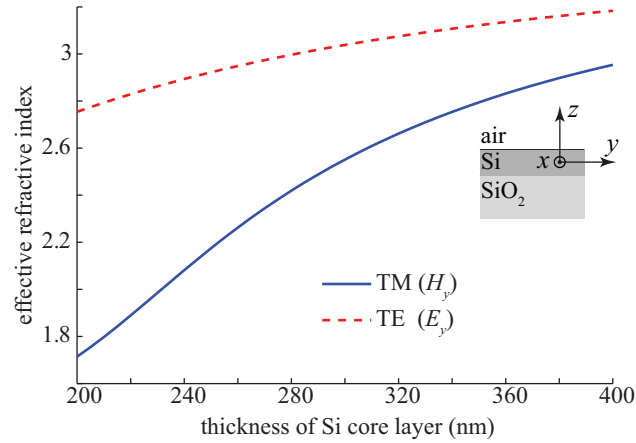


Figure 10.5: Effective indices of a slab SOI waveguide for two different polarizations as functions of the thickness of the silicon core layer.

effective index for two polarizations for the waveguide region in the 2-D model.

We here propose a new geometry for a flat-band, slow-light PhC waveguide. Our geometry is still based on W1 line defect waveguide, in which one row of holes is removed to serve as the core of the waveguide. Besides that, the first rows on each side of the defect line are truncated into semicircles. Due to the shape of the first rows, we name our proposed structure “a calzone line-defect waveguide” following Ref. [127], a schematic diagram of which is plotted in Fig. 10.6. The design parameters of such a calzone line-defect waveguide include the width of the line defect  $w$ , the radius of the holes  $r$ , and the lattice constant  $a$ .

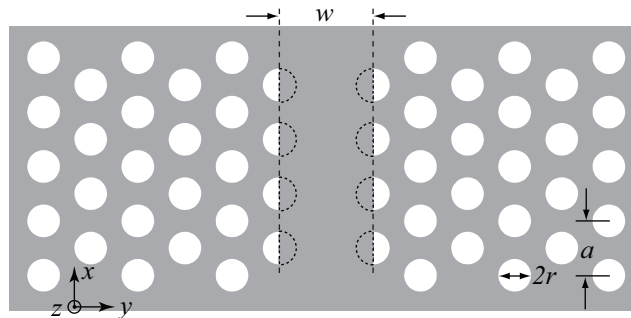


Figure 10.6: Two-dimensional schematics of a slab photonic crystal calzone line-defect waveguide with lattice constant  $a$  and hole radius  $r$ .

As an example, we choose the parameters  $a = 403$  nm,  $r = 0.3$ , and  $w = 0.7 \times \sqrt{3}a = 488.6$  nm. The calculated dispersion relation over the wavelength range near 1550 nm is shown in Fig. 10.7(a). The corresponding effective mode index  $n_{\text{eff}}$  and reduced group index  $n'_g$  as functions of wavelength are plotted in Fig. 10.7(b) and (c), respectively. One sees that for this design, there is a plateau near  $\lambda = 1551$  nm over which the group index is approximately 60. If we define the working bandwidth by requiring that the group index does not change by more than 10% within the bandwidth, the example structure has a working bandwidth of 3.2 nm. This design can be incorporated into the slow-light AWG shown in the previous section for a on-chip spectrometer with 2 GHz resolution.

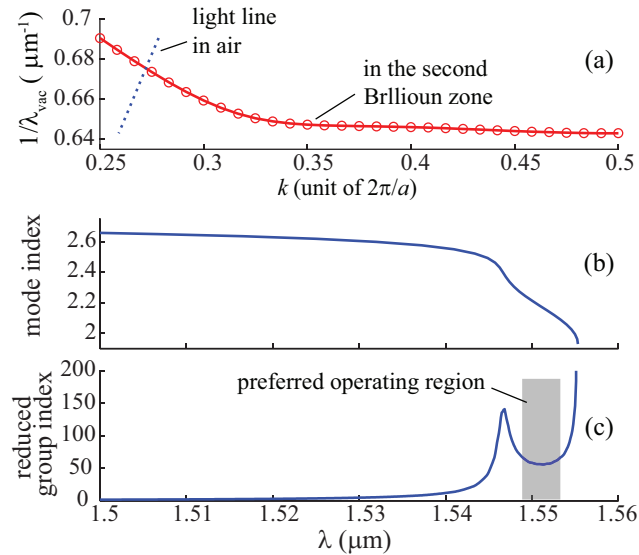


Figure 10.7: (a) dispersion relations of the fundamental guided Bloch modes of a flat-band calzone line-defect waveguide with  $a = 403$  nm,  $r = 0.3$ , and  $w = 488.6$  nm; corresponding effective mode index (b) and reduced group index  $n'_g$  (c) as functions of wavelength for such a waveguide structure.

We have also analyzed the effect of any changes of the values of  $r$  and  $w$  on the mode dispersion. Generally speaking, an increasing  $r$  leads to a higher but narrower group index plateau with a shift towards shorter wavelengths. Meanwhile, as  $w$  increases, on the other hand, the group index plateau shifts towards longer wavelengths

(lower frequency), and the height of the plateau decreases while its width increases. With further optimizing other parameters of the waveguide structure, one can further increase the group index of the waveguide with an adequate bandwidth over a few nanometers.

## 10.4 Coupling between a normal waveguide and a slow-light waveguide

Besides the geometry of the slow-light waveguide, another challenge to design a complete device is to couple light into and out of the slow-light waveguides. In particular, our proposed on-chip interferometers use conventional waveguides, e.g., channel SOI waveguides, as the main guides for the on-chip device. Thus, the challenge here is to design the connection between a channel SOI waveguide and a slow-light photonic crystal waveguide.

The coupling efficiency between two different waveguides are determined by various factors. The first factor is the effective mode indices of the two waveguides. This is in analogy to Snell's law of transmission at interface between two media. Besides this impedance matching issue, another important factor is the matching of the spatial profiles of the modes supported by the two connecting waveguides. The coupling efficiency into a single mode waveguide can be estimated using the overlap integral as follows:

$$T_{\text{cpl}} = \frac{\int dy |E_{\text{inc}}(y) E_{\text{wg}}^*(y)|^2}{\sqrt{\int dy |E_{\text{inc}}(y) E_{\text{inc}}^*(y)|^2 \int dy |E_{\text{wg}}(y) E_{\text{wg}}^*(y)|^2}}, \quad (10.13)$$

where  $E_{\text{inc}}(y)$  is the spatial profile of the incident field, and  $E_{\text{wg}}(y)$  is the spatial mode profile of the exit waveguide.

For a channel waveguide, the spatial mode profile is independent of the position along the waveguide direction (e.g.,  $x$  direction in Fig. 10.8). However, the spatial

mode profile is  $x$  dependent for a photonic crystal waveguide since the waveguide itself has a geometry change that is periodic along the waveguide. In such a case, it is natural that the coupling efficiency may change when the photonic crystal waveguide starts with a different position within its period.

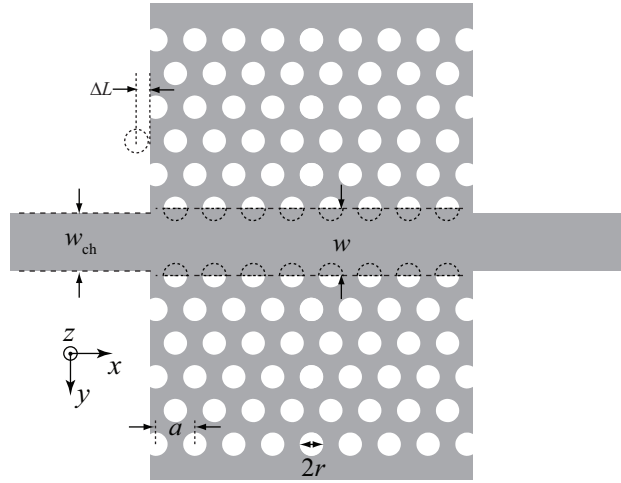


Figure 10.8: Two-dimensional schematics of connecting SOI channel waveguides with a photonic crystal calzone line-defect waveguide slab. Here  $\Delta L$  is the difference between the actual start of the PhC slab and the start of the original unmodified slab.

Furthermore, both the effective mode index and the spatial mode profile of photonic crystal waveguides can be frequency dependent, the coupling efficiency can also be frequency dependent. To optimize the coupling efficiency, we here first calculated the transmission as a function of wavelength through a channel-PhC-channel waveguide structures (see Fig. 10.8). We also change the total length of the photonic crystal region such that the interface between the channel waveguide and the calzone line defect waveguide changes. The total length of the original unmodified PhC slab is 12 lattice constant with 23 rows of honey-comb-shape spaced holes. We modify the total length with respect to the original PhC section by  $2\Delta L$  ( $\Delta L$  on each interface). If  $\Delta L$  is smaller than zero, the device may start in the middle of a row of holes as shown in Fig. 10.8, and if  $\Delta L$  is larger than zero, the extra length is all silicon without any PhC structures.

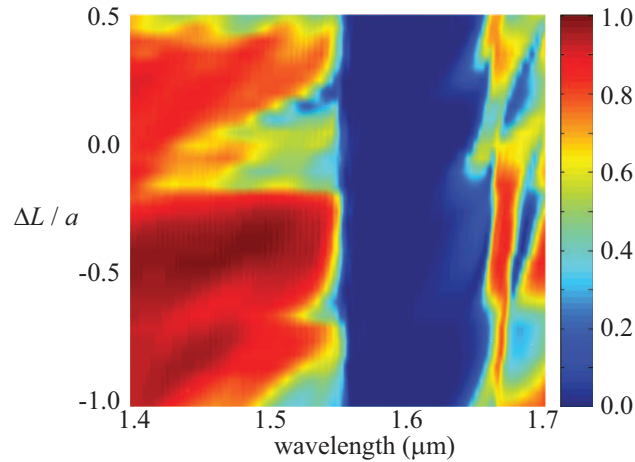


Figure 10.9: TE Transmission through a channel-PhC-channel waveguide structure as a function of wavelength and the modification of the PhC slab length  $\Delta L$ .

Using a commercial software package, Lumerical FDTD solutions, we calculated the transmission of TE polarized light (main component of  $E$ -field in  $y$ -direction) at different wavelength through such a channel-PhC-channel waveguide structure as we change the total length of the PhC slab by  $2\Delta L$ . We choose the width of the channel waveguide to be 300 nm as a typical value in a real device. The geometry of the calzone photonic crystal line-defect waveguide is described in the previous section with  $a = 403$  nm,  $r = 0.3$ , and  $w = 0.7 \times \sqrt{3}a = 488.6$  nm. The calculated transmission at wavelengths from 1.4 to 1.7  $\mu\text{m}$  is plotted in Fig. 10.9. One can see that the transmission below approximately 1.55  $\mu\text{m}$  or larger than 1.66  $\mu\text{m}$  is relatively high, and almost zero in between. This is consistent with the band diagram calculation using MPB, in which the forbidden band is located between 1.58  $\mu\text{m}$  and 1.65  $\mu\text{m}$ .

Besides the transmission over the large wavelength range of 300 nm, we are more interested in the transmission over the wavelength regime in which the photonic crystal waveguide structure has large slow-light effect. The flat-band slow-light regime of our calzone PhC structure is in the wavelength range between 1549.5 and 1552.8 nm, in which the group index is varied within 10%. The average group index with stan-

standard deviation over such wavelength range as a function of  $\Delta L$  is plotted in Fig. 10.10. One can see that the transmission has a large variation for different values of  $\Delta L$ , and the largest transmission of approximately 0.65 is achieved when  $\Delta L = -0.25a$ , where  $a$  is the lattice constant of the PhC structure.

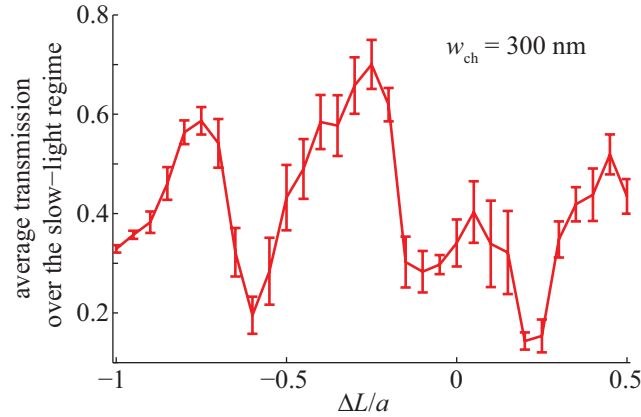


Figure 10.10: Average transmission over the slow-light regime through a channel-PhC-channel waveguide structure as a function of the modification of the PhC slab length  $\Delta L$ .

We have also changed the width  $w_{\text{ch}}$  of the channel waveguide and see if there is an optimum width for coupling light in and out of PhC slab. For a wide range of  $w_{\text{ch}}$  (approximately from 240 nm to 400 nm), the highest transmission occurs at  $\Delta L = 0.25a$ , the value of which is plotted in Fig. 10.11. As one sees, for the current parameter space, maximum transmission is achieved when  $w_{\text{ch}} = 300$  nm and  $\Delta L = -0.25a$ . One also sees that the transmission is not very sensitive to  $w_{\text{ch}}$  near 300 nm, which makes the fabrication more tolerant to experimental errors.

## 10.5 Overview of fabrication procedures

A quick summary of the fabrication procedures is shown in Fig. 10.12. We start with commercial SOI wafers with the top Silicon layer approximately 280 nm thick and Silica BOX layer approximately 3  $\mu\text{m}$  thick. We first spin coat approximately 200 nm thick of a positive e-beam resist (HSQ) followed by a 90 second pre-bake at 90  $^{\circ}\text{C}$ . We

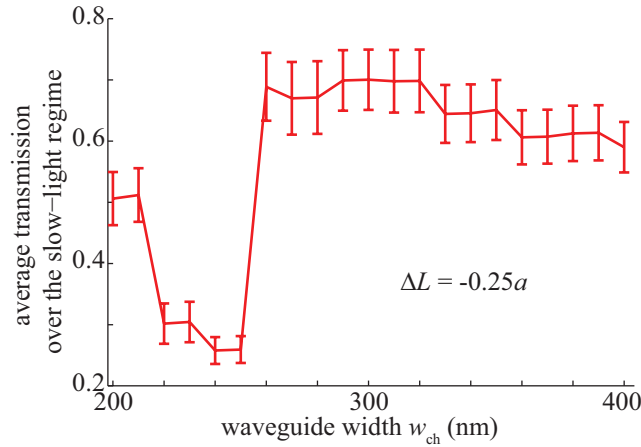


Figure 10.11: Average transmission over the slow-light regime through a channel-PhC-channel waveguide structure as a function of the width of the channel waveguide  $w_{ch}$ .

then use an e-beam lithography system (JEOL9300) to write the desired waveguide structures on the e-beam resist. After the patterns are written, the sample is taken out and developed using an e-beam resist developer (MIF 300), and only the written patterns are kept while the unexposed parts are washed away. The pattern on the e-beam resist is then treated with a resist hardening process (Branson resist stripper, process #3 for 5 minutes). After the hardening process, the sample goes through a chlorine etching process using PT-770 inductively coupled plasma (ICP) etching machine during which the pattern is transferred from the resist to the Silicon layer. The etching time is controlled such that the top Si waveguide layer is just etched through. We then dip the sample into HF for a few seconds to remove the residual e-beam resist and end up with a SOI waveguide structure.

In practice, since SOI waveguide has a Si substrate, the supported waveguide mode is actually leaky mode, which means that energy will leak into the bottom Si substrate as the mode propagates. One way to reduce the energy leaking is to remove the Silica BOX layer such that the top Si waveguide layer is surrounded by air on both sides and consequently has better energy confinement. This under-etch process is more commonly used on the photonic crystal waveguide part, but not the

conventional SOI channel waveguides. A second resist layer (usually photo-resist) is spun on top of the fabricated sample. After aligning with the existing pattern, an exposure window is patterned onto the photo-resist using a photo-lithography system (e.g., a stepper). The exposed resist is developed so only the under-etching area is not covered by the resist. the sample then goes through a selective isotropic etching process [e.g., reactive ion etching (RIE)]. The sample is then dipped into HF for a few seconds to remove the residual photo-resist and a suspended silicon photonic crystal structure is achieved.

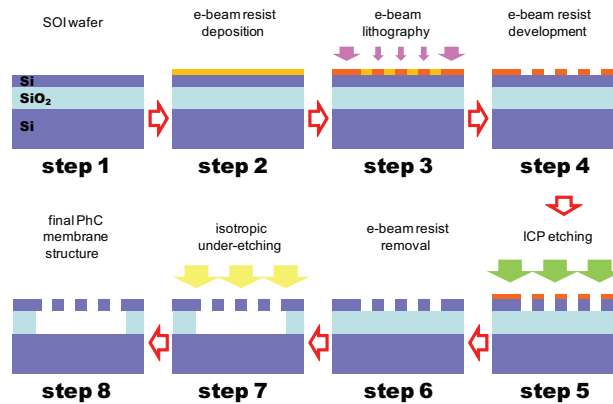


Figure 10.12: Schematic Flow Chart of fabricating a suspended silicon photonic crystal waveguide.

## 10.6 Summary

In this chapter, we have extended our concept of slow-light interferometers towards on-chip devices. We have proposed both designs of an integrated spectrometer based on a slow-light arrayed waveguide grating and designs of slow-light waveguide using calzone photonic crystal line-defect waveguides. We have also designed the connection between a normal channel waveguide and a photonic crystal waveguide to maximize the transmission. Our simulation suggests the possibility of building an chip-scale spectrometer with an spectral resolution in the order of GHz, which is approximately

100 times better than current technology. The fabrication and characterization of the device based on silicon-on-insulator platform is under progress.

# Bibliography

- [1] P. W. Milonni, *Fast light, slow light and left-handed light* (Institute of Physics, Bristol and Philadelphia, 2005).
- [2] S. E. Harris and L. V. Hau, “Nonlinear optics at low light levels,” *Phys. Rev. Lett.* **82**, 4611–4614 (1999).
- [3] M. S. Bigelow, N. N. Lepeshkin, and R. W. Boyd, “Observation of ultraslow light propagation in a ruby crystal at room temperature,” *Phys. Rev. Lett.* **90**, 113903 (2003).
- [4] R. W. Boyd and D. J. Gauthier, “‘Slow’ and ‘fast’ light,” in “Progress in Optics,” , vol. 43, E. Wolf, ed. (Elsevier Science, Amsterdam, 2002), pp. 497–530.
- [5] R. D. L. KRONIG, “On the theory of dispersion of x-rays,” *J. Opt. Soc. Am.* **12**, 547–556 (1926).
- [6] H. Kramers, “La diffusion de la lumiere par les atomes,” *Atti Cong. Intern. Fisica*, (Transactions of Volta Centenary Congress) Como **2**, 545–557 (1927).
- [7] P. Ku, C. Chang-Hasnain, and S. Chuang, “Variable semiconductor all-optical buffer,” *Electronics Letters* **38**, 1581 – 1583 (2002).
- [8] M. S. Bigelow, N. N. Lepeshkin, and R. W. Boyd, “Superluminal and slow light propagation in a room-temperature solid,” *Science* **301**, 200–202 (2003).

- 
- [9] A. Schweinsberg, N. N. Lepeshkin, M. S. Bigelow, R. W. Boyd, and S. Jarabo, “Observation of superluminal and slow light propagation in erbium-doped optical fiber,” *Europhys. Lett.* **73**, 218–224 (2006).
- [10] R. M. Camacho, M. V. Pack, J. C. Howell, A. Schweinsberg, and R. W. Boyd, “Wide-bandwidth, tunable, multiple-pulse-width optical delays using slow light in Cesium vapor,” *Phys. Rev. Lett.* **98**, 153601 (2007).
- [11] Z. Shi, R. W. Boyd, D. J. Gauthier, and C. C. Dudley, “Enhancing the spectral sensitivity of interferometers using slow-light media,” *Opt. Lett.* **32**, 915–917 (2007).
- [12] Y. Okawachi, M. S. Bigelow, J. E. Sharping, Z. Zhu, A. Schweinsberg, D. J. Gauthier, R. W. Boyd, and A. L. Gaeta, “Tunable all-optical delays via Brillouin slow light in an optical fiber,” *Phys. Rev. Lett.* **94**, 153902 (2005).
- [13] M. Herráez, K. Y. Song, and L. Thévenaz, “Optically controlled slow and fast light in optical fibers using stimulated Brillouin scattering,” *Appl. Phys. Lett.* **87**, 081113 (2005).
- [14] Y. Okawachi, M. A. Foster, J. E. Sharping, A. L. Gaeta, Q. Xu, and M. Lipson, “All-optical slow-light on a photonic chip,” *Opt. Express* **14**, 2317–2322 (2006).
- [15] R. M. Camacho, M. V. Pack, and J. C. Howell, “Slow light with large fractional delays by spectral hole-burning in rubidium vapor,” *Phys. Rev. A* **74**, 033801 (2006).
- [16] L. Yi, W. Hu, Y. Su, M. Gao, and L. Leng, “Design and system demonstration of a tunable slow-light delay line based on fiber parametric process,” *IEEE Phot. Tech. Lett.* **18**, 2575–2577 (2006).
- [17] E. Shumakher, A. Willinger, R. Blit, D. Dahan, and G. Eisenstein, “Large tunable delay with low distortion of 10 Gbit/s data in a slow light system based

- on narrow band fiber parametric amplification,” *Opt. Express* **14**, 8540–8545 (2006).
- [18] M. Soljačić, S. G. Johnson, S. Fan, M. Ibanescu, E. Ippen, and J. D. Joannopoulos, “Photonic-crystal slow-light enhancement of nonlinear phase sensitivity,” *J. Opt. Soc. Amer. B* **19**, 2052–2059 (2002).
- [19] H. Gersen, T. J. Karle, R. J. P. Engelen, W. Bogaerts, J. P. Korterik, N. F. van Hulst, T. F. Krauss, and L. Kuipers, “Real-space observation of ultraslow light in photonic crystal waveguides,” *Phys. Rev. Lett.* **94**, 073903 (2005).
- [20] Y. A. Vlasov, M. O’Boyle, H. F. Hamann, and S. J. McNab, “Active control of slow light on a chip with photonic crystal waveguides,” *Nature* **438**, 65–69 (2005).
- [21] T. F. Krauss, “Slow light in photonic crystal waveguides,” *Journal of Physics D: Applied Physics* **40**, 2666–2670 (2007).
- [22] T. Baba, “Slow light in photonics crystals,” *Nature Photonics* **2**, 465–473 (2008).
- [23] S. P. Anderson, A. R. Shroff, and P. M. Fauchet, “Slow light with photonic crystals for on-chip optical interconnects,” *Advances in Opt. Technol.* **2008**, 293531 (2008).
- [24] J. E. Heebner and R. W. Boyd, “Slow light with low dispersion and nonlinear enhancement in a lattice-shifted photonic crystal waveguide,” *J. Mod. Opt.* **49**, 2629–2636 (2002).
- [25] A. Yariv, Y. Xu, R. K. Lee, and A. Scherer, “Coupled-resonator optical waveguide: a proposal and analysis,” *Opt. Lett.* **24**, 711–713 (1999).
- [26] F. Xia, L. Sekaric, and Y. Vlasov, “Ultracompact optical buffers on a silicon chip,” *Nature Photonics* **1**, 65–71 (2007).

- [27] D. Janner, G. Galzerano, G. D. Valle, P. Laporta, S. Longhi, and M. Belmonte, “Slow light in periodic superstructure Bragg gratings,” *Phys. Rev. E* **72**, 056605 (2005).
- [28] A. Willner, B. Zhang, L. Zhang, L. Yan, and I. Fazal, “Optical signal processing using tunable delay elements based on slow light,” *IEEE J. Sel. Topics Quantum Electron.* **14**, 691–705 (2008).
- [29] G. Lenz, B. Eggleton, C. Madsen, and R. Slusher, “Optical delay lines based on optical filters,” *Quantum Electronics, IEEE Journal of* **37**, 525–532 (2001).
- [30] J. Mørk, R. Kjør, M. van der Poel, and K. Yvind, “Slow light in a semiconductor waveguide at gigahertz frequencies,” *Opt. Express* **13**, 8136–8145 (2005).
- [31] M. Soljačić, S. G. Johnson, S. Fan, M. Ibanescu, E. Ippen, and J. D. Joannopoulos, “Photonic-crystal slow-light enhancement of nonlinear phase sensitivity,” *J. Opt. Soc. Amer. B* **19**, 2052–2059 (2002).
- [32] G. S. Pati, M. Salit, K. Salit, and M. S. Shahriar, “Demonstration of a tunable-bandwidth white-light interferometer using anomalous dispersion in atomic vapor,” *Physical Review Letters* **99**, 133601 (2007).
- [33] C. Monat, B. Corcoran, M. Ebnali-Heidari, C. Grillet, B. J. Eggleton, T. P. White, L. O’Faolain, and T. F. Krauss, “Slow light enhancement of nonlinear effects in silicon engineered photonic crystal waveguides,” *Opt. Express* **17**, 2944–2953 (2009).
- [34] B. Corcoran, C. Monat, C. Grillet, D. J. Moss, B. J. Eggleton, T. P. White, L. O’Faolain, and T. F. Krauss, “Green light emission in silicon through slow-light enhanced third-harmonic generation in photonic-crystal waveguides,” *Nature Photonics* **3**, 206–210 (2008).

- [35] M. D. Stenner, M. A. Neifeld, Z. Zhu, A. M. Dawes, and D. J. Gauthier, “Distortion management in slow-light pulse delay,” *Opt. Express* **13**, 9995–10002 (2005).
- [36] M. Abraham, *Rend. Circ. Matem. Palermo* **28**, 1 (1909).
- [37] H. Minkowski, *Nachr. Ges. Wiss. Gottn Math.-Phys. Kl.* **53**, 472–525 (1908).
- [38] D. A. B. Miller, “Fundamental limit to linear one-dimensional slow light structures,” *Phys. Rev. Lett.* **99**, 203903 (2007).
- [39] R. N. C. Pfeifer, T. A. Nieminen, N. R. Heckenberg, and H. Rubinsztein-Dunlop, “Colloquium: Momentum of an electromagnetic wave in dielectric media,” *Rev. Mod. Phys.* **79**, 1197–1216 (2007).
- [40] E. A. Hinds and S. M. Barnett, “Momentum exchange between light and a single atom: Abraham or Minkowski?” *Phys. Rev. Lett.* **102**, 050403 (2009).
- [41] L. D. Landau and E. Lifshitz, *Electrodynamics of Continuous Media* (Oxford, Pergamon, 1975).
- [42] J. C. Garrison and R. Y. Chiao, “Canonical and kinetic forms of the electromagnetic momentum in an ad hoc quantization scheme for a dispersive dielectric,” *Phys. Rev. A* **70**, 053826 (2004).
- [43] E. Fermi, “Quantum theory of radiation,” *Rev. Mod. Phys.* **4**, 87 (1932).
- [44] N. L. Balazs, “The energy-momentum tensor of the electromagnetic field inside matter,” *Phys. Rev.* **91**, 408–411 (1953).
- [45] S. M. Barnett and R. Loudon, “On the electromagnetic force on a dielectric medium,” *Journal of Physics B: Atomic, Molecular and Optical Physics* **39**, S671 (2006).

- [46] P. W. Milonni and R. W. Boyd, “Recoil and photon momentum in a dielectric,” *Laser Phys.* **15**, 1432–1438 (2005).
- [47] D. F. Nelson, “Momentum, pseudomomentum, and wave momentum: Toward resolving the Minkowski-Abraham controversy,” *Phys. Rev. A* **44**, 3985–3996 (1991).
- [48] L. Allen and J. H. Eberly, *Optical Resonance and Two-Level Atomes* (Wiley, New York, 1975).
- [49] J. P. Gordon, “Radiation forces and momenta in dielectric media,” *Phys. Rev. A* **8**, 14–21 (1973).
- [50] J. Ruseckas, G. Juzeliūnas, P. Öhberg, and S. M. Barnett, “Polarization rotation of slow light with orbital angular momentum in ultracold atomic gases,” *Phys. Rev. A* **76**, 053822 (2007).
- [51] P. C. Chaumet and M. Nieto-Vesperinas, “Time-averaged total force on a dipolar sphere in an electromagnetic field,” *Opt. Lett.* **25**, 1065–1067 (2000).
- [52] P. W. Milonni, R. Loudon, P. R. Berman, and S. M. Barnett, “Linear polarizabilities of two- and three-level atoms,” *Phys. Rev. A* **77**, 043835 (2008).
- [53] J. E. Molloy and M. J. Padgett, “Lights, action: optical tweezers,” *Contemp. Phys.* **43**, 241–258 (2002).
- [54] S. Poole, D. Payne, R. Mears, M. Fermann, and R. Laming, “Fabrication and characterization of low-loss optical fibers containing rare-earth ions,” *J. Light-wave Technol.* **4**, 870 – 876 (1986).
- [55] E. Desurvire, D. Bayart, B. Desthieux, and S. Bigo, *Erbium-Doped Fiber Amplifiers: Device and System Development* (Wiley, New York, 2002), 3rd ed.

- [56] Y. Yamamoto, “Noise and error rate performance of semiconductor laser amplifiers in PCM-IM optical transmission systems,” *IEEE J. Quantum Electron.* **16**, 1073–1081 (1980).
- [57] R. H. Stolen, E. P. Ippen, and A. R. Tynes, “Raman oscillation in glass optical waveguide,” *Appl. Phys. Lett.* **20**, 62–64 (1972).
- [58] I. D. Leon and P. Berini, “Amplification of long-range surface plasmons by a dipolar gain medium,” *Nature Photonics* **4**, 382–387 (2010).
- [59] C. J. Chang-Hasnain and S. L. Chuang, “Slow and fast light in semiconductor quantum-well and quantum-dot devices,” *J. Lightwave Technol.* **24**, 4642–4654 (2006).
- [60] P. W. Milonni, “Controlling the speed of light pulses,” *Journal of Physics B: Atomic, Molecular and Optical Physics* **35**, R31 (2002).
- [61] J. B. Khurgin, “Slow light in various media: a tutorial,” *Adv. Opt. Photon.* **2**, 287–318 (2010).
- [62] C. M. Caves, “Quantum limits on noise in linear amplifiers,” *Phys. Rev. D* **26**, 1817–1839 (1982).
- [63] E. Desurvire, “A three-dimensional quantum vacuum-noise/signal beamsplitter model for nonideal linear optical amplifiers,” *Optical Fiber Technology* **5**, 82 – 91 (1999).
- [64] Y. Yamamoto and H. A. Haus, “Preparation, measurement and information capacity of optical quantum states,” *Rev. Mod. Phys.* **58**, 1001–1020 (1986).
- [65] C. Henry, “Theory of the linewidth of semiconductor lasers,” *Quantum Electronics, IEEE Journal of* **18**, 259 – 264 (1982).

- [66] K. Petermann, *Laser Diode Modulation and Noise* (Kluwer Academic, Dordrecht, 1988), chap. 2.
- [67] S. Donati and G. Giuliani, “Noise in an optical amplifier: formulation of a new semiclassical model,” *IEEE J. Quantum Electron.* **33**, 1481–1488 (1997).
- [68] N. Olsson and J. Van Der Ziel, “Characteristics of a semiconductor laser pumped Brillouin amplifier with electronically controlled bandwidth,” *J. Light-wave Technol.* **5**, 147 – 153 (1987).
- [69] R. W. Tkach and A. R. Chraplyvy, “Fibre Brillouin amplifiers,” *Optical and Quantum Electronics* **21**, S105–S112 (1989).
- [70] R. W. Boyd, D. J. Gauthier, A. L. Gaeta, and A. E. Willner, “Maximum time delay achievable on propagation through a slow-light medium,” *Phys. Rev. A* **71**, 023801 (2005).
- [71] R. Tucker, P. Ku, and C. Chang-Hasnain, “Delay–bandwidth product and storage density in slow-light optical buffers,” *Electronics Letters* **41**, 208–209 (2005).
- [72] R. W. Boyd and P. NARUM, “Slow- and fast-light: fundamental limitations,” *J. Mod. Opt.* **54**, 2403–2411 (2007).
- [73] Z. Shi, R. Pant, Z. Zhu, M. D. Stenner, M. A. Neifeld, D. J. Gauthier, and R. W. Boyd, “Design of a tunable time-delay element using multiple gain lines for increased fractional delay with high data fidelity,” *Opt. Lett.* **32**, 1986–1988 (2007).
- [74] A. Minardo, R. Bernini, and L. Zeni, “Low distortion Brillouin slow light in optical fibers using AM modulation,” *Opt. Express* **14**, 5866–5876 (2006).
- [75] T. Schneider, M. Junker, K. Lauterbach, and R. Henker, “Distortion reduction in cascaded slow light delays,” *Electronics Letters* **42**, 1110 – 1111 (2006).

- [76] J. B. Khurgin, “Performance limits of delay lines based on optical amplifiers,” *Opt. Lett.* **31**, 948–950 (2006).
- [77] A. Zadok, A. Eyal, and M. Tur, “Extended delay of broadband signals in stimulated Brillouin scattering slow light using synthesized pump chirp,” *Opt. Express* **14**, 8498–8505 (2006).
- [78] Z. Lu, Y. Dong, and Q. Li, “Slow light in multi-line Brillouin gain spectrum,” *Opt. Express* **15**, 1871–1877 (2007).
- [79] C. Yu, T. Luo, L. Zhang, and A. E. Willner, “Data pulse distortion induced by a slow-light tunable delay line in optical fiber,” *Opt. Lett.* **32**, 20–22 (2007).
- [80] G. P. Agrawal, *Fiber-Optic Communication Systems* (Wiley, New York, 2002), chap. 4, 3rd ed.
- [81] J. Downie, “Relationship of Q penalty to eye-closure penalty for NRZ and RZ signals with signal-dependent noise,” *J. Lightwave Technol.* **23**, 2031–2038 (2005).
- [82] B. Zhang, L. Yan, I. Fazal, L. Zhang, A. E. Willner, Z. Zhu, and D. J. Gauthier, “Slow light on Gbit/s differential-phase-shift-keying signals,” *Opt. Express* **15**, 1878–1883 (2007).
- [83] Z. Shi, R. W. Boyd, Z. Zhu, D. J. Gauthier, R. Pant, M. D. Stenner, and M. A. Neifeld, “Distortion-reduced pulse-train propagation with large delay in a triple gain media,” in “Slow and Fast Light,” (Optical Society of America, 2006), p. WB3.
- [84] Z. Zhu, A. M. C. Dawes, D. J. Gauthier, L. Zhang, and A. E. Willner, “Broadband SBS slow light in an optical fiber,” *J. Lightwave Technol.* **25**, 201–206 (2007).

- [85] K. Y. Song, M. G. Herráez, and L. Thévenaz, “Gain-assisted pulse advancement using single and double Brillouin gain peaks in optical fibers,” *Opt. Express* **13**, 9758–9765 (2005).
- [86] S. Chin, M. Gonzalez-Herraez, and L. Thévenaz, “Simple technique to achieve fast light in gain regime using Brillouin scattering,” *Opt. Express* **15**, 10814–10821 (2007).
- [87] S. Chin, M. Gonzalez-Herraez, and L. Thevenaz, “Self-advanced fast light propagation in an optical fiber based on Brillouin scattering,” *Opt. Express* **16**, 12181–12189 (2008).
- [88] V. P. Kalosha, L. Chen, and X. Bao, “Slow and fast light via sbs in optical fibers for short pulses and broadband pump,” *Opt. Express* **14**, 12693–12703 (2006).
- [89] R. Pant, M. D. Stenner, M. A. Neifeld, Z. Shi, R. W. Boyd, and D. J. Gauthier, “Maximizing the opening of eye diagrams for slow-light systems,” *Appl. Opt.* **46**, 6513–6519 (2007).
- [90] E. Cabrera-Granado, O. G. Calderón, S. Melle, and D. J. Gauthier, “Observation of large 10-Gb/s SBS slow light delay with low distortion using an optimized gain profile,” *Opt. Express* **16**, 16032–16042 (2008).
- [91] T. Sakamoto, T. Yamamoto, K. Shiraki, and T. Kurashima, “Low distortion slow light in flat Brillouin gain spectrum by using optical frequency comb,” *Opt. Express* **16**, 8026–8032 (2008).
- [92] R. S. Tucker, P.-C. Ku, and C. J. Chang-Hasnain, “Slow-light optical buffers: Capabilities and fundamental limitations,” *J. Lightwave Technol.* **23**, 4046 (2005).

- [93] Q. Sun, Y. V. Rostovtsev, J. P. Dowling, M. O. Scully, and M. S. Zubairy, “Optically controlled delays for broadband pulses,” *Phys. Rev. A* **72**, 031802 (2005).
- [94] Z. Deng, D.-K. Qing, P. Hemmer, C. H. R. Ooi, M. S. Zubairy, and M. O. Scully, “Time-bandwidth problem in room temperature slow light,” *Phys. Rev. Lett.* **96**, 023602 (2006).
- [95] Z. Dutton, M. Bashkansky, M. Steiner, and J. Reintjes, “Analysis and optimization of channelization architecture for wideband slow light in atomic vapors,” *Opt. Express* **14**, 4978–4991 (2006).
- [96] D. D. Yavuz, “Electromagnetically induced transparency with broadband laser pulses,” *Phys. Rev. A* **75**, 031801 (2007).
- [97] M. Bashkansky, Z. Dutton, F. K. Fatemi, J. Reintjes, and M. Steiner, “Demonstration of bicolor slow-light channelization in rubidium vapor,” *Phys. Rev. A* **75**, 021401 (2007).
- [98] G. Lenz, B. Eggleton, C. Giles, C. Madsen, and R. Slusher, “Dispersive properties of optical filters for WDM systems,” *IEEE J. Quantum Electron.* **34**, 1390–1402 (1998).
- [99] R. H. J. Kop, P. de Vries, R. Sprik, and A. Lagendijk, “Kramers-Kronig relations for an interferometer,” *Opt. Commun.* **138**, 118–126 (1997).
- [100] K. Jinguji and M. Oguma, “Optical half-band filters,” *J. Lightwave Technol.* **18**, 252–259 (2000).
- [101] C.-H. Cheng, L. Lin, T. Towe, T. J. Xia, C. Wong, K. Wu, and J.-C. Chiao, “Spectral slicer without cascaded dispersion penalty,” *Optical Communication, 2002. ECOC 2002. 28th European Conference on* **1**, 1–2 (2002).

- [102] A. Zadok, A. Eyal, and M. Tur, “Gigahertz-wide optically reconfigurable filters using stimulated Brillouin scattering,” *J. Lightwave Technol.* **25**, 2168–2174 (2007).
- [103] T. Schneider, M. Junker, and K.-U. Lauterbach, “Potential ultra wide slow-light bandwidth enhancement,” *Opt. Express* **14**, 11082–11087 (2006).
- [104] K. Y. Song and K. Hotate, “25 GHz bandwidth Brillouin slow light in optical fibers,” *Opt. Lett.* **32**, 217–219 (2007).
- [105] O. P. Lay, S. Dubovitsky, R. D. Peters, J. P. Burger, S.-W. Ahn, W. H. Steier, H. R. Fetterman, and Y. Chang, “Mstar: a submicrometer absolute metrology system,” *Opt. Lett.* **28**, 890–892 (2003).
- [106] Z. Xie and H. F. Taylor, “Fabry-Perot optical binary switch for aircraft applications,” *Opt. Lett.* **31**, 2695–2697 (2006).
- [107] X.-F. Mo, B. Zhu, Z.-F. Han, Y.-Z. Gui, and G.-C. Guo, “Faraday-Michelson system for quantum cryptography,” *Opt. Lett.* **30**, 2632–2634 (2005).
- [108] S. Sakadzic and L. V. Wang, “High-resolution ultrasound-modulated optical tomography in biological tissues,” *Opt. Lett.* **29**, 2770–2772 (2004).
- [109] S. M. Shahriar, G. Pati, V. Gopal, R. Tripathi, G. Cardoso, P. Pradhan, M. Mesal, and R. Nair, “Precision rotation sensing and interferometry using slow light,” in “Quantum Electronics and Laser Science Conference (QELS),” (paper JWB97, 2005).
- [110] C. Roychoudhuri, “Multiple-beam interferometers,” in “Optical Shop Testing,” D. Malacara, ed. (Wiley, New York, 1992), p. 213.
- [111] B. Jensen and A. Torabi, “Refractive index of hexagonal II–VI compounds CdSe, CdS, and  $\text{CdSe}_x\text{S}_{1-x}$ ,” *J. Opt. Soc. Am. B* **3**, 857–863 (1986).

- [112] P. Hariharan, *Optical Interferometry* (Elsevier Science, Amsterdam, 2003), chap. 11, pp. 173–187, 2nd ed.
- [113] A. Gomez-Iglesias, D. O’Brien, L. O’Faolain, A. Miller, and T. F. Krauss, “Direct measurement of the group index of photonic crystal waveguides via fourier transform spectral interferometry,” *Appl. Phys. Lett.* **90**, 261107 (2007).
- [114] N. Walker and J. Carroll, “Simultaneous phase and amplitude measurements on optical signals using a multiport junction,” *Electron. Lett.* **20**, 981–983 (1984).
- [115] A. Banerjee, D. Das, and V. Natarajan, “Precise frequency measurements of atomic transitions by use of a Rb-stabilized resonator,” *Opt. Lett.* **28**, 1579–1581 (2003).
- [116] D. A. Steck, “Rubidium 87 *d* line data,” <http://steck.us/alkalidata> .
- [117] J. Sharping, Y. Okawachi, and A. Gaeta, “Wide bandwidth slow light using a Raman fiber amplifier,” *Opt. Express* **13**, 6092–6098 (2005).
- [118] Z. Shi, R. W. Boyd, R. M. Camacho, P. K. Vudyasetu, and J. C. Howell, “Slow-light Fourier transform interferometer,” *Phys. Rev. Lett.* **99**, 240801 (2007).
- [119] M. D. Lukin, M. Fleischhauer, A. S. Zibrov, H. G. Robinson, V. L. Velichansky, L. Hollberg, and M. O. Scully, “Spectroscopy in dense coherent media: Line narrowing and interference effects,” *Phys. Rev. Lett.* **79**, 2959–2962 (1997).
- [120] M. Fleischhauer, A. Imamoglu, and J. P. Marangos, “Electromagnetically induced transparency: Optics in coherent media,” *Reviews of Modern Physics* **77**, 633 (2005).
- [121] M. Smit, “New focusing and dispersive planar component based on an optical phased array,” *Electron. Lett.* **24**, 385–386 (1988).

- 
- [122] R. Jacobsen, A. Lavrinenko, L. Frandsen, C. Peucheret, B. Zsigri, G. Moulin, J. Fage-Pedersen, and P. Borel, “Direct experimental and numerical determination of extremely high group indices in photonic crystal waveguides,” *Opt. Express* **13**, 7861–7871 (2005).
- [123] J. P. Hugonin, P. Lalanne, T. P. White, and T. F. Krauss, “Coupling into slow-mode photonic crystal waveguides,” *Opt. Lett.* **32**, 2638–2640 (2007).
- [124] S. G. Johnson and J. D. Joannopoulos, “Block-iterative frequency-domain methods for Maxwell’s equations in a planewave basis,” *Opt. Express* **8**, 173–190 (2001).
- [125] J. Li, T. P. White, L. O’Faolain, A. Gomez-Iglesias, and T. F. Krauss, “Systematic design of flat band slow light in photonic crystal waveguides,” *Opt. Express* **16**, 6227–6232 (2008).
- [126] D. Dimitropoulos, V. Raghunathan, R. Claps, and B. Jalali, “Phase-matching and nonlinear optical processes in silicon waveguides,” *Opt. Express* **12**, 149–160 (2004).
- [127] K. Hennessy, C. Hogerle, E. Hu, A. Badolato, and A. Imamoglu, “Tuning photonic nanocavities by atomic force microscope nano-oxidation,” *Applied Physics Letters* **89**, 041118 (2006).